Spring 1-1-2013

Remote Measurement of Shallow Media Depth Using Polarization Lidar

Steven Edward Mitchell
University of Colorado at Boulder, steven.e.mitchell@gmail.com

Remote Measurement of Shallow Media Depth Using Polarization Lidar

by

Steven E. Mitchell

B.S., Mechanical Engineering, University of Maryland at College Park,

2005

M.S., Aerospace Engineering Sciences, University of Colorado at Boulder,

2009

A thesis submitted to the

Faculty of the Graduate School of the

University of Colorado in partial fulfillment

of the requirements for the degree of

Doctor of Philosophy

Department of Aerospace Engineering Sciences

2013

This thesis entitled:
Remote Measurement of Shallow Media Depth Using Polarization Lidar
written by Steven E. Mitchell
has been approved for the Department of Aerospace Engineering Sciences

Dr. Jeffrey P. Thayer

Dr. Xinzhao Chu

Date

The final copy of this thesis has been examined by the signatories, and we find that both the content and the form meet acceptable presentation standards of scholarly work in the above mentioned discipline.

Mitchell, Steven E. (Ph.D., Aerospace Engineering Sciences)

Remote Measurement of Shallow Media Depth Using Polarization Lidar

Thesis directed by Dr. Jeffrey P. Thayer

Active noncontact range measurement sensors transmit electromagnetic radiation onto a remote target and process the received scattered signals to resolve the separation distance, or range, between the sensor and target. For lidar sensors, range is resolved by halving the roundtrip transit time multiplied by the speed of light, accounting for the refractive indices of the transit media. The ranging technique enables remote measurement of depth by resolving the range to sequential surfaces. Depth measurement in the shallow regime has conventionally been limited by the presence of ambiguous, overlapping optical pulses scattered from sequential surfaces. Enhanced performance in the shallow regime has conventionally come at the expense of the increased cost and complexity associated with high performance componentry. The issue of remote shallow depth measurement presents an opportunity for a novel approach to lidar sensor development.

In this work, I discuss how the issue of ambiguity in the shallow depth measurement may be addressed by exploiting the polarization orientation of the transmitted and received optical signals, the components of which are modified during the range observation by naturally-occurring phenomena. Conventional pulsed time of flight laser ranging sensors are unable to resolve the shallow depth between overlapping pulses received from sequential surfaces due to operation in the scalar lidar regime, where the intensity of the received scattered signal is measured with no regard for polarization information. Enhanced performance by scalar lidar sensors in the shallow media regime has been conventionally enabled through incorporation of picosecond pulse width lasers and fast photodetectors, along with their associated increase in cost and complexity.

The polarization lidar approach to shallow depth measurement developed in the dissertation facilitates the use of common lasers, optics, and detection componentry, making it comparatively less complex and costly while achieving two orders of magnitude improvement in the depth reso-

lution of distant targets. Evolution of the measurement is presented, from concept and laboratory demonstration to development of prototype instrumentation. The approach is presented within the context of lidar bathymetry, with demonstrated measurement of 1 cm water depths with an uncertainty of ± 3 mm. Furthermore, the approach provides an estimate of the first surface linear depolarization ratio, enabling differentiation between surfaces defined by variable scattering matrices. The theory is sufficiently generalized for future application to depth measurement of additional media with bounding surfaces defined by unique scattering matrices.

Dedication

To my family, those who have come before me, and those ahead.

Acknowledgements

I would like to thank my research advisor, Dr. Jeffrey Thayer, for his continued support and guidance throughout my graduate career. I would like to thank my committee members Dr. Scott Palo, Dr. Xinzhao Chu, Dr. John Degnan, and Dr. Waleed Abdalati, who have each made unique and lasting contributions to my dissertation.

A special thank you must go on record to my fellow graduate students. Matt Hayman is the graduate student responsible for developing the Stokes Vector Lidar Equation. I have appreciated the opportunity to collaborate with Matt and incorporate his work into my doctoral research. Katelynn Greer and Cody Vaudrin supported exploration of a spectrum of ideas and provided much needed life balance. Robert Stillwell has contributed a great amount of effort to the development of the prototype polarization lidar.

This research was funded in part by the NASA Earth and Space Science Fellowship project number 154-5064. Additional hardware support was funded in part by the 2008 CIRES Innovative Research Program project number 10652 and The Center for Space Entrepreneurship in Boulder, CO. I am grateful for each funding opportunity.

I would like to document a very special thank you to my parents and sister. Your support throughout the years has been the fuel that has enabled me to pursue my dreams. Thank you to my aunt and cousins for their lifelong support and encouragement. Last but not least, thank you to my loving and understanding wife, who has continuously supported me on the journey through graduate school, particularly with its nonlinear trajectory, and routinely provides the necessary ΔV to keep our satellite in orbit.

Contents

Chapter

1 Introduction 1

1.1 Research Impact 1

1.2 Resolving Range 3

1.3 Remote Sensing of Depth 3

1.4 Thesis Overview 7

2 Range-Resolved Observations Through Aqueous Media 9

2.1 Introduction 9

2.2 Historical Context 9

2.3 The Water Depth Measurement 10

2.4 Conventional Lidar Bathymetry 14

2.4.1 Theory 14

2.4.2 Detection 17

2.5 Performance Limitations 18

2.5.1 Extinction Along the Optical Path 18

2.5.2 Pulse Overlap 18

2.6 Case Study: Remote Sensing of Supraglacial Melt Lakes 22

2.7 Sensor Development 25

3 Theory 27

3.1 Introduction . . . 27

3.2 Polarization in Range-Resolved Observations . . . 27

3.3 The Stokes Vector Lidar Equation . . . 28

3.4 Polarization in Range-Resolved Observations of Shallow Media Depth . . . 30

3.5 Range-resolved Observations of Distant Shallow Media Depth . . . 33

3.5.1 Transmit Polarization . . . 33

3.5.2 Transmitter Effects . . . 34

3.5.3 Transmission Through Media of Variable Refractive Index . . . 34

3.5.4 Interaction with Media Surfaces . . . 36

3.5.5 Receiver Effects . . . 42

3.5.6 Background . . . 44

3.6 Laboratory Demonstration . . . 44

4 Detection 48

4.1 Introduction . . . 48

4.2 Photoelectron Generation . . . 48

4.2.1 Simulation . . . 52

4.2.2 Optimization . . . 58

4.3 Range Operation . . . 58

4.3.1 Signal Acquisition . . . 59

4.3.2 Implications for Sensor Architecture . . . 64

4.3.3 Signal to Noise Considerations . . . 67

4.3.4 Detection Threshold and Timing Data Considerations . . . 69

4.3.5 Discussion . . . 77

5 Intrapulse Phase Modification Induced by Scattering 83

5.1 Introduction . . . 83

5.2 Technique 83
5.3 Simulation 87
5.4 Optimization 95
5.5 Laboratory Demonstration 96
5.5.1 Simulation 97
5.5.2 Measurements 99
5.6 Conclusions 106

6 Instrumentation 108
6.1 Introduction 108
6.2 Sensor Overview 108
6.2.1 Design 108
6.2.2 Mitigation of Polarization Effects 111
6.2.3 Detection 117
6.3 Measurements 123
6.3.1 Polarization Indiscriminate Detection 123
6.3.2 Polarization Discriminate Detection 131
6.4 Conclusions 143

7 Conclusions and Recommendations 148
7.1 Conclusions 148
7.2 Recommendations 149

Bibliography 151

Tables

Table

6.1 Transmitter and Receiver Specifications of the Prototype Polarization Lidar 109

Figures

Figure

1.1 Comparison of the operational range and resolution capabilities of conventional active noncontact optical ranging techniques, modified from [16]. 4

1.2 Representative waveforms received by a lidar bathymetry sensor for decreasing water depth, taken from [110]. Received signals scattered from the surface **S** and bottom **B** begin to overlap in the shallow water regime (depth < 2 m), limiting the capacity of the sensor to resolve range to the surface and bottom and prohibiting measurement of water depth. 6

2.1 Setup for conventional airborne lidar bathymetry operations, taken from [71]. 11

2.2 Absorption of pure freshwater versus wavelength, taken from [140]. Lidar sensors developed to penetrate water are designed to transmit in the region around 500 nanometers due to the low absorption of blue-green wavelengths. 12

2.3 Timing diagram for range-resolved observation of water depth. 13

2.4 Conceptual waveform received by the conventional lidar bathymetry sensor, taken from [54]. 15

2.5 Scattering effects on the portion of the transmitted laser pulse that is refracted into the water volume, taken from [142]. 16

2.6 Data acquired with a conventional lidar bathymetry sensor, as presented at the 2013 International Lidar Mapping Forum [103]. The voltage output by the photodetector is digitized, typically at rates on the order of 1 GHz as shown here. A measurement of water depth is provided by differencing the time stamp of each apex in the photodetector output waveform, accounting for the refractive index of water. 19

2.7 Typical SHOALS bathymetry coverage superimposed onto a Google Earth image, taken from [10]. The sensor is unable to resolve between surface and bottom returns received from regions of shallow water, resulting in significant data gaps in the littoral zone. 21

2.8 Aerial view of a supraglacial melt lake on the GIS, taken from [90]. 24

2.9 Diagram of glaciological features involved in the formation and drainage of supraglacial melt lakes, taken from [145]. Water drained from supraglacial melt lakes propagates through the GIS via moulins to the bedrock, leading to enhanced basal lubrication. 24

3.1 Preliminary efforts have been made to incorporate polarization lidar techniques into lidar bathymetry. Here, depth profiles of co- (red) and cross-polarized (blue) receiver measurements for received scattered signals from the water and floor of a near-shore ocean region indicate the polarization-preserving nature of the water surface and depolarization due to rough bottom topography, taken from [29]. 29

3.2 Timing diagram for range-resolved observations through semitransparent media bounded by N surfaces. 32

3.3 Diagram of a Stokes vector (green arrow) of arbitrary intensity, described by its linear rotation angle ε and ellipticity θ angle, modified from [139]. 35

3.4 Reflectivity of typical natural bounding surfaces of semitransparent media for incident shortwave radiation, taken from [113]. 39

3.5 Intensity of the transmitted and reflected optical signals for polarized light incident upon a smooth air/water interface. 41

3.6 Illustration of the large and small scale surface roughness of an arbitrary semitransparent media surface, taken from [11]. Media surfaces defined by a rough surface mean height $h(\overline{r})\overline{n}$ on the order of the incident laser wavelength, such as ice, tend to depolarize the incident laser light. Typically, surfaces of clear waters encountered by ALB sensors are defined by large scale roughness $h(x, z)$ excited by surface winds, with negligible small scale roughness in the absence of turbidity, and tend to preserve the incident laser polarization orientation. 43

3.7 Setup for the initial laboratory demonstration to illustrate the potential of the SVLE approach to classify scattering surfaces. A pulsed laser operating at 532 nm is transmitted through a series of mirrors into a plastic tube partially filled with water. Scattered signals are passed through a rotating polarizer prior to detection by a photomultiplier tube. 45

3.8 Screenshots of the photomultiplier voltage output as viewed on a 4 GHz oscilloscope. The target consisted of a tube filled with (a) water atop a submerged smooth plastic substrate, and (b) water atop a submerged ice substrate. Due to the polarization-preserving nature of the water surface and plastic substrate, received scattered signals are suppressed by the polarizer in the receiver when the polarizer is oriented 90° to the transmitted laser plane. However, the depolarizing nature of the submerged ice substrate decouples the incident laser energy and permits range observation regardless of polarizer orientation. 47

4.1 Transmitted Stokes vector $\vec{S}_{TX} = [1, 0.95, 0, 0]^T$ oriented linear horizontal with 0.95 degree of polarization. 53

4.2 Received Stokes vectors for the simulated polarization lidar. The photodetector in each detection channel measures the S_0 (intensity) element of parallel (blue) and perpendicular (red) vectors. 54

4.3 Normalized detected signal for varying surface a_1 (f_{22} element) and transmitted DOP. 55

4.4 Simulated photodetector output for a polarization lidar ranging through semitransparent media bounded by $N = 3$ surfaces with varying depolarization scattering matrices defined by f_{22} elements $a_1 = 1.0$, $a_2 = 0.2$, $a_3 = 0.6$. 57

4.5 Illustration of the detection schemes commonly used in pulsed TOF laser ranging, shown here for the received signals scattered from a multi-storied forest canopy, taken from [63]. 60

4.6 Depiction of the photoemitting element of a typical photodetector used for laser ranging. The element, defined with quantum efficiency η and active surface area A_d, is subject to an incoming average photon rate $\overline{W}$ prior to an average emission rate of $\overline{N}$ photoelectrons. 61

4.7 The discrete Poisson probability density function described by Equation (4.33) for variable average photoelectron count $\overline{N}$ and emitted photoelectrons k. 63

4.8 Probability of the photodetector emitting a minimum of 1 photoelectron as a function of the average emission rate $\overline{N}$ [33, 39]. 65

4.9 Diagram of the expected noise and signal sources during flight, modified from Figure (2.3). A pulse of laser energy of length $c\tau$ is emitted from the sensor at time t_0 in the presence of multiple noise sources. Signals are scattered from the first and second surface by time t_2 and transit back to the sensor. 71

4.10 Detector dark noise rates as provided by the photodetector manufacturer. The photodetector is typically operated with a supply voltage of 0.80 V, generating an average dark noise rate of $\overline{N}_{b,dark} = 50$ photoelectrons/sec. 72

4.11 False alarm and detection probabilities for the range measurement of the first surface with the sensor detection threshold configured to $k_{th} = 10$. 74

4.12 Simulated timing data for a flat water surface and bottom bounding 6 cm of water. The data is simulated in the detection channel receiving signals scattered in the polarization plane parallel to the transmitted laser light and photodetector with no pulse jitter. The detection threshold $k_{th} \gg 10$ such that no noise events are registered by the detection electronics. The detection channel is assumed to operate with no dead time such that received signals scattered from the water surface and bottom are recorded by the timing electronics. 76

4.13 Simulated timing data for a flat water surface and bottom bounding 6 cm of water. The data is simulated in the detection channel receiving signals scattered in the polarization plane parallel to the transmitted laser light and photodetector with no pulse jitter. The detection threshold $k_{th} \gg 10$ such that no noise events are registered by the detection electronics, however a dead time corresponding to 30 bins has been incorporated into the measurement, preventing the sensor from registering signals scattered from the bottom. 78

4.14 Simulated timing data for a flat water surface and bottom bounding 6 cm of water. The data is simulated in the detection channel receiving signals scattered in the polarization plane parallel to the transmitted laser light and photodetector with no pulse jitter. The detection threshold k_{th} has been lowered to $k_{th} \ll 10$ to increase the P_{fa} such that the detection electronics register noise events. Registration of noise events introduces a randomly-occurring dead time, statistically enabling registration of signals scattered from the surface and bottom. 79

4.15 False alarm and detection probabilities for the simulated sensor. The average noise background has been increased by an order of magnitude, resulting an eight orders of magnitude increase in the false alarm probability for the stationary detection threshold $k_{th} = 10$. 82

5.1 Timing diagram for range-resolved observations of shallow semitransparent media via the INPHAMIS technique. 86

5.2 Voltage output from the photodetector of a conventional lidar sensor, ranging with polarization indiscriminate detection, for scattered signals received by the sensor from a simulated 40 cm water depth. The peaks of each received signal are readily identifiable ($t = 0$, $t = 3.5$ nsec) enabling a measurement of depth between surfaces. 89

5.3 Voltage output from the photodetector of a conventional lidar sensor, ranging with polarization indiscriminate detection, for overlapping scattered signals received by the sensor from a simulated 17 cm water depth. Further decreases in depth between surfaces will render the depth measurement indeterminable due to overlap of the received scattered signals. 90

5.4 Voltage output from the photodetector of a polarization discriminate lidar sensor for overlapping scattered signals received by the sensor from a simulated 17 cm water depth. Optical discrimination of the polarization orientation of scattered signals received from each surface enables depth measurement at sub-pulse width resolution. 91

5.5 Simulated timing data for a flat water surface and bottom for 3 cm deep water. The data is simulated in the co-polarized detection channel to simulate a conventional polarization indiscriminate lidar bathymetry sensor, incorporating the expected pulse jitter from the photodetector, noise events, and the governing 270 nsec electrical dead time associated with the detection electronics. Received signals scattered from the water surface are defined by a polarization-maintaining scattering matrix, enabling the dead time associated with the detection electronics and preventing registration of signals scattered from the bottom. Introduction of noise events and a randomly occurring dead time does not aid in the measurement, as surface and bottom signals are contained within the envelope of the scattered waveform. 93

5.6 Simulated timing data for a flat water surface and bottom for 3 cm deep water. The data is simulated in the co- (blue) and cross-polarized (red) detection channels to simulate the polarization discriminate detection approach of Chapter 4. Received signals scattered from the water surface are suppressed by the polarization analyzer in the receiver, enabling the registration of signals scattered from the depolarizing bottom in the perpendicular detection channel at sub pulse width resolution. 94

5.7 Diagram of the sensor developed to demonstrate the INPHAMIS technique. 96

5.8 Simulation of normalized received intensity for a range of quarterwave plate orientations for targets of varying degrees of vertical linear depolarization a. 100

5.9 Outline of the normalized digital timing histograms for surface and bottom returns at 3.0 cm (dashed) and 1.0 cm (solid) water depths. 102

5.10 Overlay of normalized surface and bottom histograms from Figure (5.9) along with insert of timing differences between the two determined bottom returns. 105

6.1 Block diagram (left) and image of the prototype polarization lidar sensor (right). The lidar transmits 532 nm laser light oriented in a linear polarization plane and simultaneously detects the parallel and perpendicular components of the received scattered light. 110

6.2 Geometrical overlap function $G(R)$ of the prototype polarization lidar as a function of range. The transmit and receive paths overlap at 150 m range such that $\geq 97\%$ of the scattered signal is received by the telescope. 112

6.3 Measurement setup for the process of evaluating the capacity of each optical element in $\mathbf{M_{TX}}$ and $\mathbf{M_{RX}}$ to modify the Stokes vector of the transiting laser light. Analyzing optics are highlighted by the red dashed box and consist of a quarterwave plate, polarizer, and photodetector. Based on the results of the measurement shown here, it was determined that the halfwave plate decoupled the polarization of the transiting laser signal. As a result, the positions of the halfwave and polarizer were reversed, enabling the polarizer to reject the cross-polarized component. 114

6.4 Measurement of the Stokes vector exiting the microchip laser. 116

6.5 Measurement of the Stokes vector exiting the telescope. A known Stokes vector defined by the output of the laser, beam expander, and Glan Thompson polarizer optical train was input to the telescope. Ten exiting Stokes vectors were measured with the telescope is rotated about its optical axis and displaced in the plane orthogonal to the optical axis. The results indicated negligible modification of the transiting laser light. 118

6.6 Hamamatsu specifications for photomultiplier tube cathode radiant sensitivity as a function of wavelength (left) and gain as a function of control supply voltage (right). The H7422PA-40 series photomultiplier tubes were chosen for their high radiant sensitivity at 532 nm, as well as the $10^5 - 10^6$ gain available at the nominal operational control supply voltage of 0.80 V. 119

6.7 Constant fraction discriminator block diagram. Electrical output from each PMT is passed to independent channels of the CFD, which determines the PMT signal apex independently of the signal pulse height. The CFD outputs a TTL-level pulse of 270 nsec width that is passed to and stored onboard the TDC. 121

6.8 Representative signal components of the CFD circuit. Provided a suitable fraction and delay is chosen, the apex of the PMT voltage output will be discriminated at the same point in time regardless of the PMT pulse height. 122

6.9 (**not to scale**) Diagram of the experimental setup. An opaque target is mounted a distance d_0 from the lidar. A semitransparent target is initially mounted at depth **A** from d_0, larger than the equivalent depth d_{CFD} defined by the 270 nsec CFD dead time. The semitransparent target is relocated to depth **B**, within d_{CFD}. Finally, the semitransparent target is relocated to depth **C**, within the equivalent depth d_{LASER} defined by the 450 psec laser pulse width. 124

6.10 Timing histogram generated by the lidar in the parallel detection channel from a single opaque surface over a 4 sec integration period. The TDC produces a histogram with a 27 psec bin width and one bin entry per laser firing. The width of the histogram is dictated by pulse jitter from the PMT. 125

6.11 Timing histograms simultaneously acquired from an opaque surface (right) mounted at 4252.5 cm depth from a semitransparent surface (left) over a 4 sec integration period. 127

6.12 Timing histogram acquired from a semitransparent surface (left) over a 4 sec integration period. The opaque surface is mounted at 3651 cm depth, within the governing 270 nsec dead time of the lidar. As a result, no timing histogram is acquired from the opaque surface (right). 128

6.13 Timing histograms simultaneously acquired from an opaque surface (right) mounted at 3651 cm depth from a semitransparent surface (left) over a 20 sec integration period. The CFD voltage threshold is lowered to discriminate noise events, generating a randomly occurring 270 nsec dead time. 130

6.14 Timing histograms simultaneously acquired from an opaque surface (right) mounted at 3651 cm depth from a semitransparent surface (left) over a 4 sec integration period. Data at left are acquired in the parallel detection channel; at right in the perpendicular channel. 133

6.15 Measurement configuration in which the glass surface is mounted at depth of 2.4 cm from the wall. The 450 psec pulse width of the laser corresponds to 6.75 cm in range. Utilizing the INPHAMIS approach, timing histograms were integrated in the parallel and perpendicular detection channels to demonstrate the capability of the sensor to measure the depth between sequential surfaces at sub-laser pulse width resolution. 135

6.16 Envelope of normalized timing histograms simultaneously acquired over a 30 sec integration period for the parallel (solid) and perpendicular (dashed) detection channels, from an opaque surface (left) and semitransparent surface mounted between the lidar and opaque surface (right). 136

6.17 Experimental configuration for the water depth measurement. The sensor was mounted to point vertically downward from an open hatch, ranging to a container of water with a submerged plastic substrate (left), the surface of which was roughened to simulate depolarizing ice. Timing histograms were integrated in the parallel and perpendicular detection channels (right), producing a water depth measurement at sub-laser pulse width resolution. 138

6.18 Observed depolarization ratio m_j versus halfwave plate calibration angle ϕ_j. Point data were obtained by taking the sum and ratio of timing histograms in the parallel and perpendicular detection channels for $\phi_j = 0°, 10°, \ldots, 90°$. Data were also acquired for $\phi_j = 45°$ for reference. A nonlinear least squares analysis generated values of $G = 1.67$, $\delta = 0.52$, and $\theta = 2.53°$. 142

6.19 Timing histograms integrated in the parallel and perpendicular detection channels for differing surfaces of the building. Integrating and ratioing the counts during the interval defined by the vertical dashed lines permits generation of a depolarization ratio which can be used to classify differing surfaces based on their propensity to decouple the incident laser signal. 144

6.20 Plot of the depolarization ratio for each surface illuminated during the experiment. Polarization maintaining surfaces such as the 2nd floor windows produce low depolarization ratios ($\delta < 1$) while depolarizing surfaces are distinguished by their variable δ values. 145

6.21 Theoretical depolarization ratio data acquired during flight of the sensor onboard a UAS over the supraglacial melt lake from Figure (2.8). Evaluation of the measured depolarization ratios during flight operations may aid in classification of water/ice boundaries as well as differing ice surfaces. 145

Chapter 1

Introduction

1.1 Research Impact

This dissertation focuses on improving the capacity of pulsed time of flight (TOF) laser ranging sensors to resolve the depths of distant shallow media by exploiting the polarization orientation of transmitted and received optical signals. The research has provided the first remote depth measurement of extremely shallow media using a laser ranging sensor. Evolution of the measurement is presented, from concept to laboratory demonstration to development and operation of prototype instrumentation, which has led to publication [99, 97] and patent [98] opportunities. The research is performed in the context of lidar bathymetry and has had tangible impact on the community, including reference in bathymetry texts such as the 2012 book Fluvial Remote Sensing for Science and Management by Carbonneau and Piégay [23]. Parallel applications in additional areas of remote depth sensing are provided at the conclusion of this dissertation in support of continued future exploration.

> ***"In the future, hardware and software developments will enhance the resolution, accuracy, and types of data products derived from riverine airborne lidar surveys. First, the use of polarized lidar will probably enhance the capacities of extremely shallow water bathymetry (Mitchell et al., 2010)."***
>
> **Carbonneau and Piégay**, Fluvial Remote Sensing for Science and Management

The outcomes of this research include:

- Developed a novel, sophisticated approach to resolve the depths of distant shallow media by evaluating the differing polarization orientations of optical signals scattered from bounding media surfaces
- Demonstrated exploitation of naturally-occurring phase modification induced by the scattering process to enable resolution of intrapulse received signals and remove conventional pulse overlap limitations in the shallow media regime
- Developed an approach to differentiate between media surface types by measuring the propensity of the surface to modify the polarization orientation of the incident laser signal
- Developed a prototype lidar sensor demonstrating the advantages of the polarization approach over conventional lidar approaches that favor high performance componentry such as picosecond pulse width lasers and fast detection electronics

The fundamental impact of the dissertation research is the removal of limitations imposed by pulse overlap ambiguities in the shallow media regime and subsequent improvement in the depth measurement capabilities of pulsed TOF lidar sensors. Conventionally, the severity of the pulse overlap limitation has been reduced by incorporating components of reduced temporal width into the sensor; however, this brute force approach requires high performance componentry such as picosecond pulse width lasers and fast detection electronics, leading to increased cost and complexity of the system. This dissertation offers a more sophisticated approach to overcome pulse overlap ambiguities by configuring the system to evaluate the polarization orientation of the received optical signal, the components of which are naturally modified during the scattering process. This approach allows for the use of common lasers, optics, and detection components, making it comparatively less complex and costly while achieving two orders of magnitude improvement in the depth resolution of distant shallow media compared to conventional approaches.

1.2 Resolving Range

Range measurement sensors resolve the separation distance between the sensor and a target of interest. These sensors have heritage in applications including computer vision and robotics [73], target tracking [7, 38], and topographic and coastal mapping [2, 17, 59, 78]. Active noncontact range-resolving sensors transmit electromagnetic radiation onto the target and process the received scattered signal to resolve the distance (or range) between the sensor and target. Applications requiring high spatial resolution transmit optical radiation, primarily for the reduced divergence compared to radio and ultrasonic wavelengths. Active noncontact optical ranging encompasses three approaches [6, 79]: interferometry, time of flight, and triangulation. While the reader is directed to [16, 76] for a detailed description of each approach, Figure (1.1) provides an overview of the operational range and resolution capabilities of the conventional active noncontact optical ranging techniques.

Remote range-resolution environments such as mapping, in which the target is located hundreds to thousands of meters from the sensor, lend themselves to the pulsed TOF technique, which permits transmission of higher peak power than interferometric or triangulation techniques. In direct detection pulsed TOF ranging, the sensor emits a pulse of laser energy toward the target and measures the transit time required for the scattered light to be received by the sensor. Range between the sensor and target is resolved by taking half of the roundtrip transit time multiplied by the speed of light, accounting for the refractive index of the transit media along the optical path.

1.3 Remote Sensing of Depth

Remote range-resolved observations *through* semitransparent media, in which the target is of finite thickness bounded by a first and second surface, are also enabled by the pulsed TOF technique. Here, range observations between the sensor and bounding surfaces are resolved to enable a measurement of media depth along the probed optical path [96]. Measurement of media depth fundamentally requires a) the first surface to be penetrable, and b) both surfaces to be detectable.

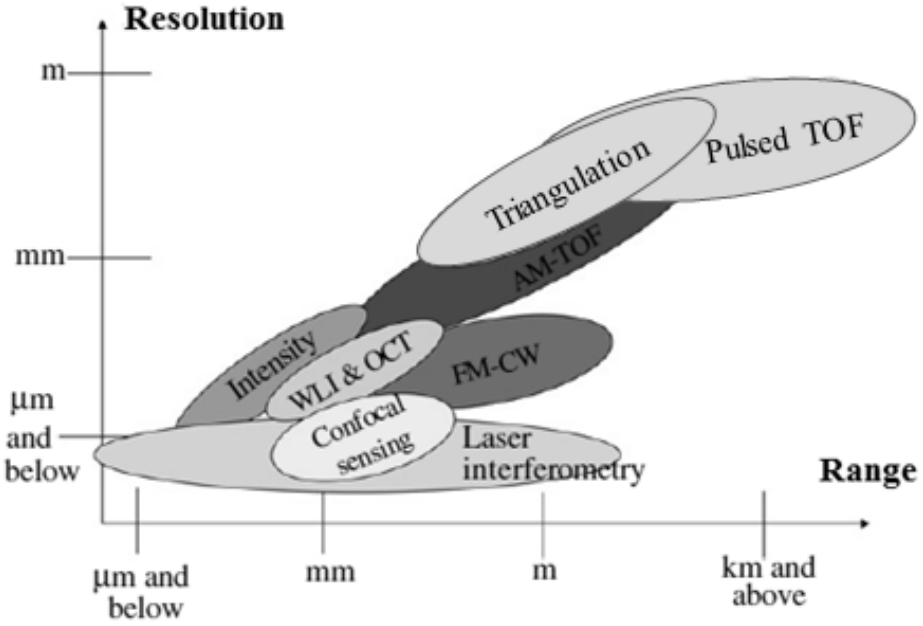

Figure 1.1: Comparison of the operational range and resolution capabilities of conventional active noncontact optical ranging techniques, modified from [16].

In the case of aqueous media, the pulsed TOF technique has heritage in resolving the depths of moderately clear, near-shore coastal waters and lakes typical of the littoral zone [59, 83, 114]. These lidar (light detection and ranging) bathymetry sensors routinely operate onboard platforms such as helicopters and fixed-wing aircraft, resolving range between the sensor and the water surface and bottom to provide measurements of water depth and subsurface terrain for use in coastal engineering and resource management [31, 32, 48], nautical charting [55], and reconnaissance efforts [71].

The conventional lidar bathymetry system consists of a pulsed laser transmitter operating at 532 nm, near the spectral absorption minimum of most natural waters [69, 125], coupled with a receiver telescope and optical detector [57, 53]. The system operates by emitting a pulse of laser energy towards the target water body and receiving the scattered light, which typically contains two peaks indicating the signals received from the water surface and bottom. The range between the sensor and each bounding surface of the aqueous media is resolved according to [93]

$$R = \frac{c\Delta t}{2n} \tag{1.1}$$

where Δt is the time of flight of the received signal scattered from each bounding surface, c is the speed of light in a vacuum, and n is the refractive index of the transit media along the optical path, typically air ($n = 1.00$) and water ($n = 1.33$) for bathymetric observations.

The capacity of the lidar bathymetry sensor to range through waters of increasing depth is limited primarily by extinction of the transmitted laser pulse along the optical path. Range-resolved observations through water are significantly limited in the shallow water regime, typically defined for depths < 2 m [3, 10], due to the inability of the sensor to distinguish between overlapping received signals scattered from the water surface and bottom [9, 110] as illustrated in Figure (1.2). As a result, conventional lidar bathymetry sensors ranging through shallow waters are limited to meter-level depth measurements [59], with more complex systems working to achieve sub-meter resolution [81, 102], and the depths of shallow waters remain largely unresolved. The deficiency in this area of remote active noncontact optical sensing of shallow media depth has motivated the dissertation research.

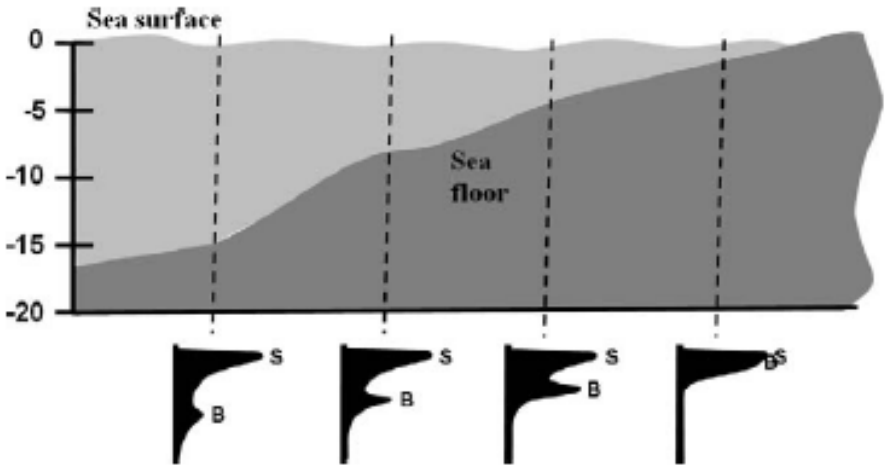

Figure 1.2: Representative waveforms received by a lidar bathymetry sensor for decreasing water depth, taken from [110]. Received signals scattered from the surface **S** and bottom **B** begin to overlap in the shallow water regime (depth < 2 m), limiting the capacity of the sensor to resolve range to the surface and bottom and prohibiting measurement of water depth.

1.4 Thesis Overview

The remainder of this dissertation is divided into six additional chapters. A brief description of the contents of each chapter is provided here.

- **Chapter 2**: This chapter contains background information describing the severity of the shallow media pulse overlap limitation that has plagued conventional laser ranging sensors. The problem is framed in the context of lidar bathymetry, specifically the study of supraglacial melt lakes that form in the summer months atop the Greenland Ice Sheet.

- **Chapter 3**: This chapter contains the mathematical foundation for the polarization lidar work described in this dissertation. Operation of the polarization lidar sensor is described within the framework of the Stokes Vector Lidar Equation, which provides a comprehensive approach to range resolved observations through semitransparent media expressed in terms of Stokes vectors and Mueller matrices.

- **Chapter 4**: This chapter discusses the detection approach to polarization discriminate laser ranging, including dual detection channels to evaluate the propensity of the scattering surface to depolarize the incident laser signal, along with signal to noise considerations for the range measurement.

- **Chapter 5**: This chapter details application of the polarization lidar approach to range resolved observations through shallow media, in which overlapping received signals scattered from sequential surfaces are contained within laser pulse width.

- **Chapter 6**: This chapter details the development of a prototype polarization lidar which evaluates the differing polarization orientations of signals scattered from bounding semitransparent media surfaces, simultaneously receiving signals polarized in the planes parallel and perpendicular to the transmitted laser signal via dual detection channels.

- **Chapter 7**: This chapter provides a summary of the dissertation, including recommenda-

tions for future applications of the research.

Chapter 2

Range-Resolved Observations Through Aqueous Media

2.1 Introduction

This chapter provides background information on the field of lidar bathymetry to provide context for the dissertation research presented in following chapters, including a description of conventional sensor operation and performance limitations.

2.2 Historical Context

Lidar bathymetry is a technique for remotely resolving the depths of moderately clear, near-shore coastal waters and lakes typical of the littoral zone [59, 83, 114]. The technique is typically employed from an airborne platform, although spaceborne [14, 100] and shipborne [44] observations have been considered. While the lidar technique originated in the atmospheric sciences to measure the elevation of clouds [46] and density profiles through the atmosphere [137], ground-based lidar sensors quickly developed, enabling range measurements with levels of precision previously unobtainable, such as enhanced resolution of the distance between the Earth and the Moon [126]. The potential for airborne lidar bathymetry (ALB) was realized in 1965 with the development of the lidar bathymeter for submarine detection [109, 129]. The seminal paper detailing the feasibility of deploying a laser sensor for airborne bathymetric observations was written in 1969 by Hickman and Hogg [69] at the Syracuse University Research Corporation.

From these localized beginnings, ALB technology experienced global growth in the development of sensors such as the NASA Airborne Oceanographic Lidar in the 1970s [80], the Australian

WRELADS II [112] in the 1980s, SHOALS in the 1990s by Optech [56, 71], and more recent efforts such as the EAARL system [45, 101]. As illustrated in Figure (2.1), these systems operate onboard platforms such as helicopters and fixed-wing aircraft [143], collecting range-resolved observations through water to enable measurements of water volume and subsurface terrain for use in coastal engineering and resource management [31, 32, 48], nautical charting [55], and reconnaissance efforts [71]. Throughout its history, ALB has offered operational advantages over alternative bathymetric techniques such as sonar sensors in terms of high spatial resolution and coverage rates, flexibility, noncontact measurement, and mobility.

2.3 The Water Depth Measurement

The fundamental ALB sensor consists of a pulsed laser transmitter operating at 532 nm, near the spectral absorption minimum of most natural waters [69, 125] as shown in Figure (2.2), coupled with a receiver telescope and optical detector [57, 53]. Many conventional lidar bathymetry sensors transmit and receive the fundamental 1064 nm laser output to aid in water surface identification, due to the minimal skin depth of infrared wavelengths in water [93, 113], at the expense of an additional receiver channel. As illustrated in Figure (2.3), a laser pulse of temporal width τ is transmitted from the sensor at time t_0 through air with refractive index n_0 towards the target water body. The pulse intercepts the water surface **S**, shown here as smooth water for illustrative purposes, at time t_1. A portion of the laser pulse is reflected at the air/water interface back to the sensor. The remaining portion of the laser pulse is transmitted into the water, where the energy is subject to increased extinction along the refracted optical path through the water column. A portion of the transmitted energy reflects off the bottom **B** of the water body at time t_2 and propagates back to the receiver. Depth measurement is based on the differential arrival times of the range-resolved received signals **1** and **2**, accounting for differences in refractive index along the optical path and laser pointing angle relative to the water surface normal.

A conceptual waveform received by the conventional lidar bathymetry sensor is provided in Figure (2.4), illustrating the fundamental received components: surface return, volumetric backscat-

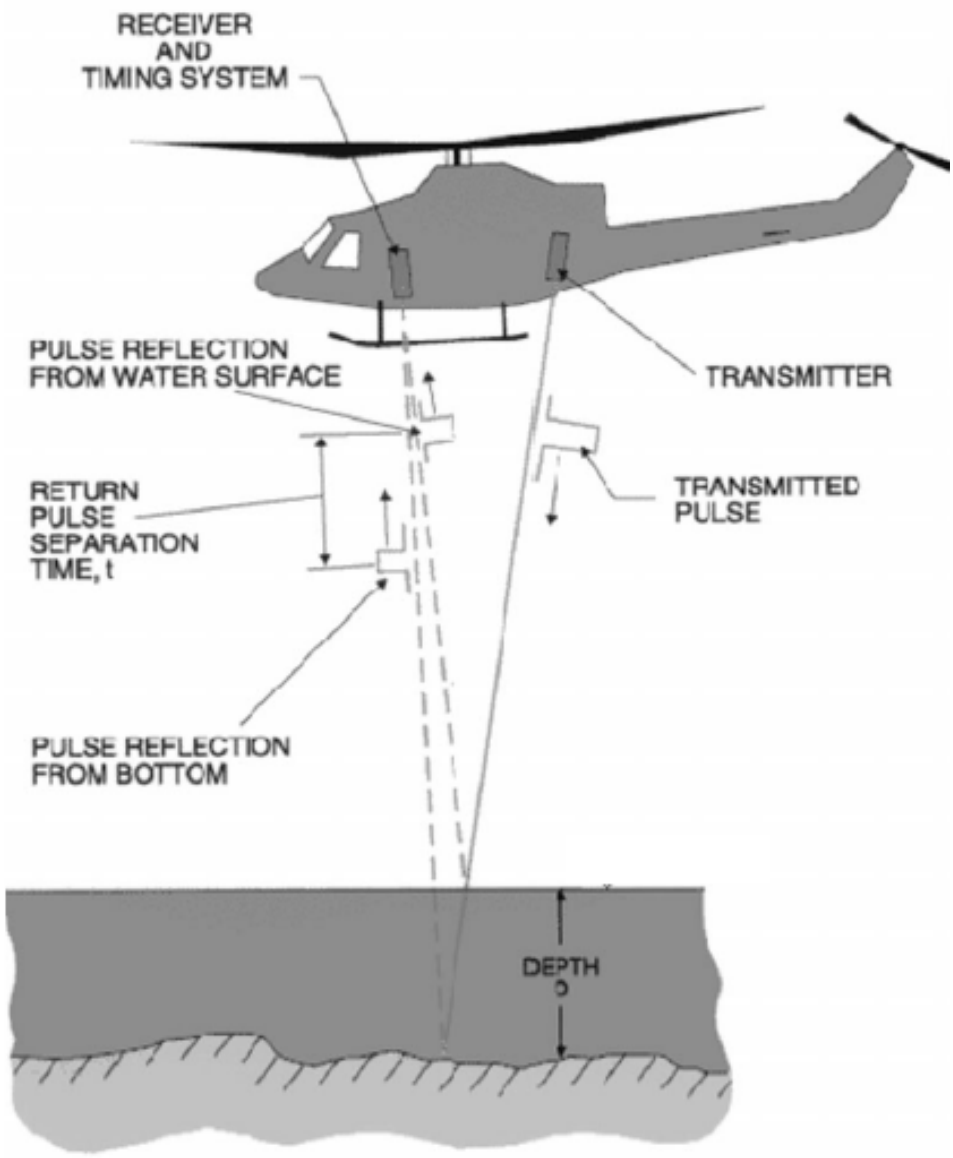

Figure 2.1: Setup for conventional airborne lidar bathymetry operations, taken from [71].

Figure 2.2: Absorption of pure freshwater versus wavelength, taken from [140]. Lidar sensors developed to penetrate water are designed to transmit in the region around 500 nanometers due to the low absorption of blue-green wavelengths.

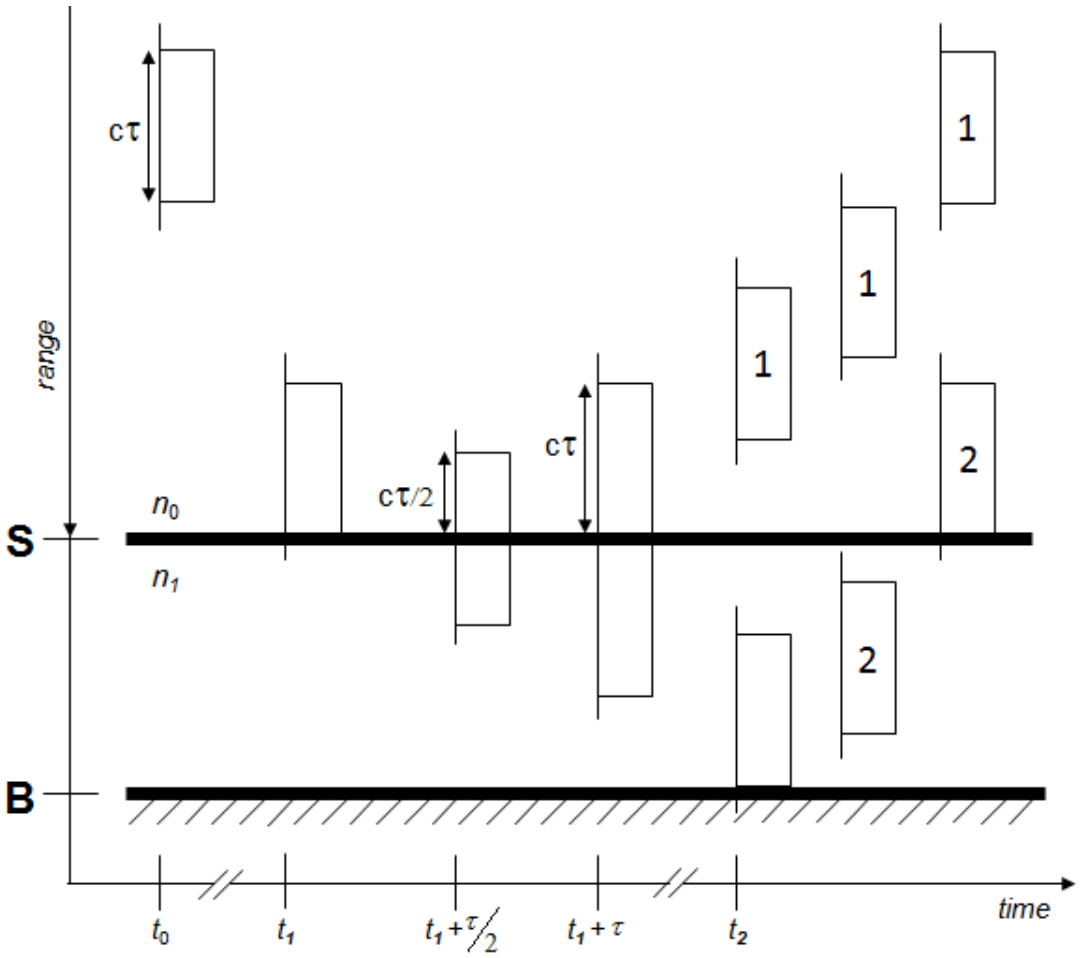

Figure 2.3: Timing diagram for range-resolved observation of water depth.

ter, and bottom return. The amplitude of the surface return varies by orders of magnitude with water surface conditions and laser pointing angle relative to the water surface normal [22]. If the laser transmitter is pointed significantly off nadir, backscattered surface energy will be received by the sensor only when waves are excited sufficiently by surface winds to present a large quantity of facets oriented perpendicular to the beam [58]. In low-wind conditions, favorable for aircraft operations, a smooth water surface results in a decrease in the intensity of the backscattered return, while the dynamic range of amplitudes increases, as the surface return is strong at nadir (approaching 2% of the transmitted pulse energy for near-nadir Fresnel reflections) and decreases rapidly for off-nadir angles. High wind conditions tend to minimize the dynamic range of received signals from the surface, at the cost of increased water turbidity and less favorable aircraft operating conditions. Contrasting high and low wind conditions, surface return intensities are increasingly lower at nadir for high winds, but fall off slowly as the transmitted beam is pointed off-nadir.

The portion of the laser pulse transmitted into the water volume is further attenuated based on water clarity during transit. The beam is subject to additional scattering and broadening during transit through the water, as illustrated in Figure (2.5). A portion of the transmitted energy is reflected from the bottom and received by the sensor, potentially upwards of six orders of magnitude weaker than the surface return. This dynamic range of received signals during sensor operation places demand on the lidar receiver architecture, with a natural inclination toward the use of photomultiplier tubes due to their ability to linearly detect low light levels across five to six orders of magnitude in dynamic range.

2.4 Conventional Lidar Bathymetry

2.4.1 Theory

Conventional non-polarization lidar bathymetry is described by the Scalar Lidar Equation, which relates the transmitted and received intensity (photons) according to [23, 93, 91]

$$N_{RX}(R,\lambda) = N_{TX}(\lambda)\left[\beta(\lambda)\Delta R\right]\frac{A}{R^2}T(\lambda)^2\left[\eta_{RX}\eta_{TX}G(R)\right] + N_B \tag{2.1}$$

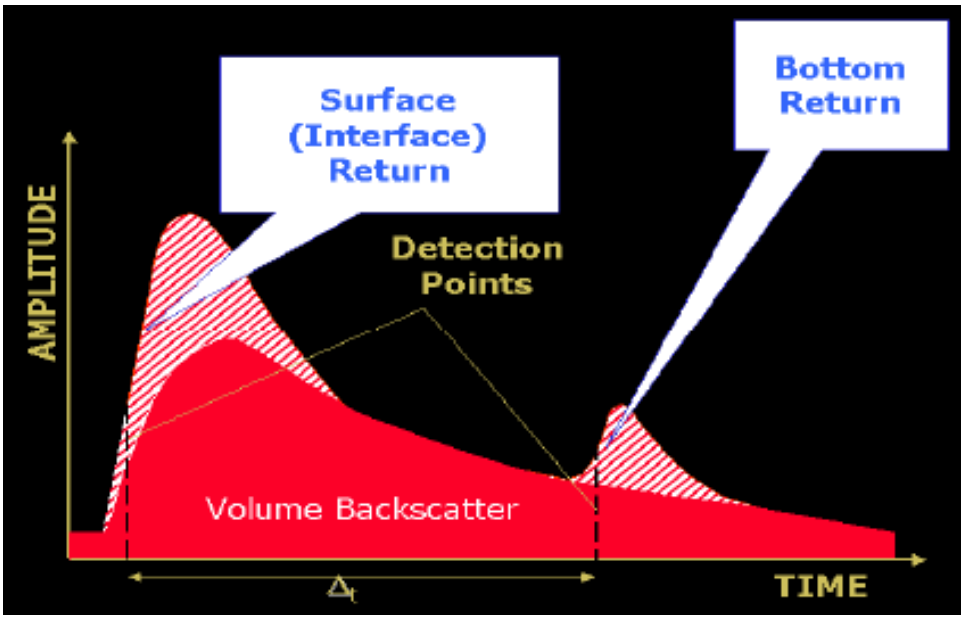

Figure 2.4: Conceptual waveform received by the conventional lidar bathymetry sensor, taken from [54].

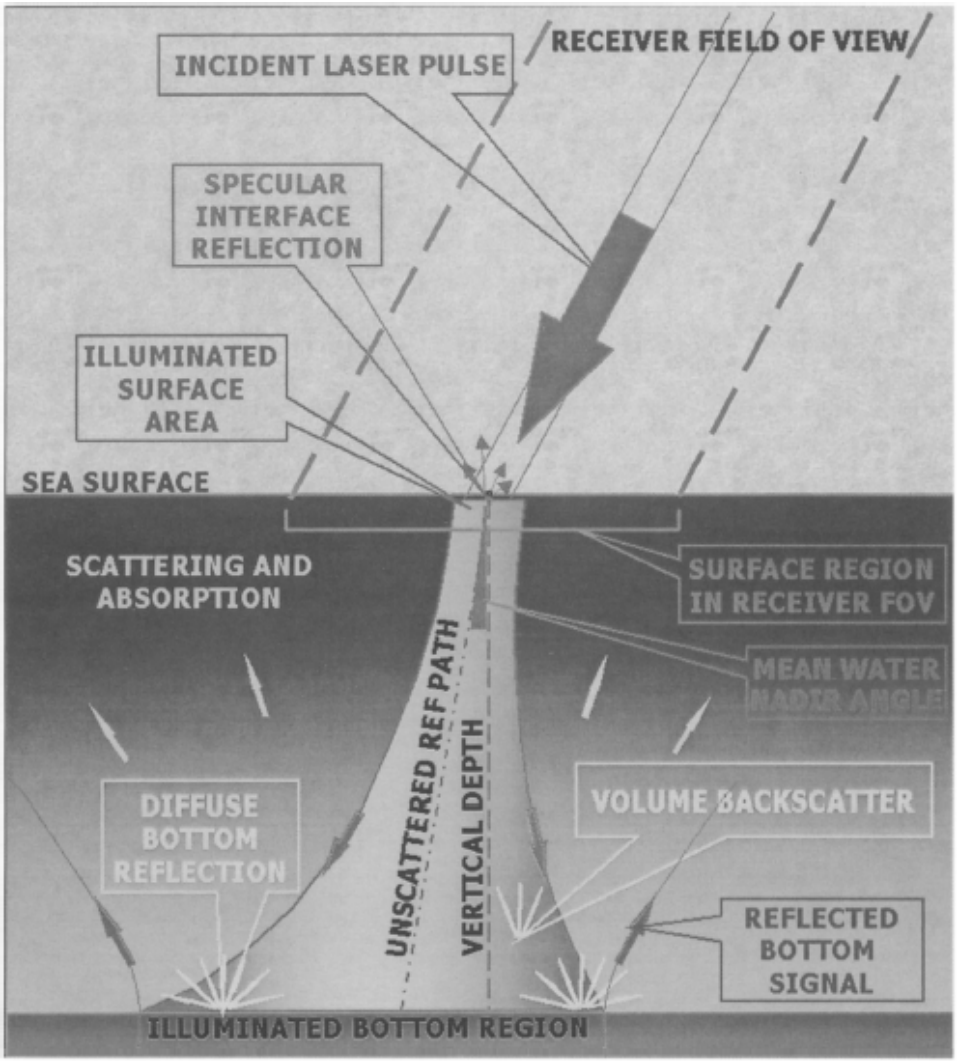

Figure 2.5: Scattering effects on the portion of the transmitted laser pulse that is refracted into the water volume, taken from [142].

where λ is defined as the operational wavelength of 532 nm, $N_{RX}(R, \lambda)$ is the intensity or number of received photons at λ and range R, $N_{TX}(\lambda)$ is the number of transmitted photons, $\beta(\lambda)$ defines the scattering properties of the water surface, volume, or bottom at wavelength λ, ΔR is the sensor range resolution, A is the receiver effective aperture, $T(\lambda)$ is the transmission of the atmosphere at wavelength λ, η_{TX} and η_{RX} are the transmitter and receiver system efficiencies, respectively, $G(R)$ is the geometrical overlap function of the sensor, and $N_B(\lambda)$ is the background noise at wavelength λ. An additional $T(\lambda)$ term exists in Equation (2.1) when $\beta(\lambda)$ defines the water volume or bottom to account for transmission of the laser pulse through the air/water interface and the water volume. For conventional lidar bathymetry sensors, Equation (2.1) provides sufficient free variables to give full description to range-resolved observations through water.

2.4.2 Detection

Conventional lidar bathymetry sensors transmit modest laser pulse energies (mJ) and use high detection thresholds to resolve unambiguous range measurement of surface and bottom scattered signals with few false alarms in the presence of noise from detector dark counts and background solar illumination [57, 63]. These sensors are designed to receive thousands of scattered photons for each transmitted laser pulse in order to exceed the detector noise floor and enable monopulse observation of depth. For lidar bathymetry sensors, laser energy is of particular demand in the deep water regime, where the signal scattered from the bottom is subject to maximum extinction along the optical path. Due to this demand for high energy, conventional sensors typically use high energy lasers with broad pulse widths on the order of several nsec, restricting operation to low repetition rates on the order of hundreds of Hz [53, 72].

The conventional approach to lidar bathymetry favors a simplified detection scheme, where the use of lasers with modest pulse energies is prioritized over other aspects of the system such as size, weight, and power consumption (SWaP). The voltage waveform output from the photodetector is digitized at rates on the order of 1 GHz, as illustrated in Figure (2.6). The use of high power lasers and power-consuming digitizing electronics significantly limits operation of these conventional

sensors onboard platforms with SWaP restrictions.

2.5 Performance Limitations

Although ALB enables remote range-resolved observation of bathymetric environments, fundamental limitations to the water depth measurement exist, as described in this section.

2.5.1 Extinction Along the Optical Path

The capacity of the lidar bathymetry sensor to measure the depths of deep waters (typ. $>$ 10 m) is limited primarily by extinction of the transmitted laser pulse along the optical path. The density of water and particulates along the probed water column contribute to both scattering and absorption of the laser pulse and spreading of the beam. This extinction along the optical path increases exponentially with increasing water depth. The result is a decrease in the intensity of scattered light received by the sensor. The depth at which extinction renders bottom scattered signals undetectable is known as the maximum surveyable depth [58]. Conventional lidar bathymetry sensors are typically capable of resolving range through water depths greater than 50 m in clean offshore waters and approximately 10 m in turbid near-shore waters [54]. As indicated in Equation (2.1), the limit to achieving a deep water depth measurement for an arbitrary water volume is related to the transmitted laser energy and telescope aperture. Range-resolution of deeper water depths is readily achievable by increasing these sensor parameters.

2.5.2 Pulse Overlap

Significant limitations to range-resolution through aqueous media are manifested in the shallow water regime, typically defined for water depths $<$ 2 m [3, 10]. The limit to achieving a shallow water depth measurement is related to the applied lidar technique and the governing time responsivity of the lidar, which defines the capacity of the system to distinguish between two surfaces along the same optical path but separated in range. The time responsivity is governed by the slowest timing element in the lidar system, such as the laser pulse width, detector pulse width, or

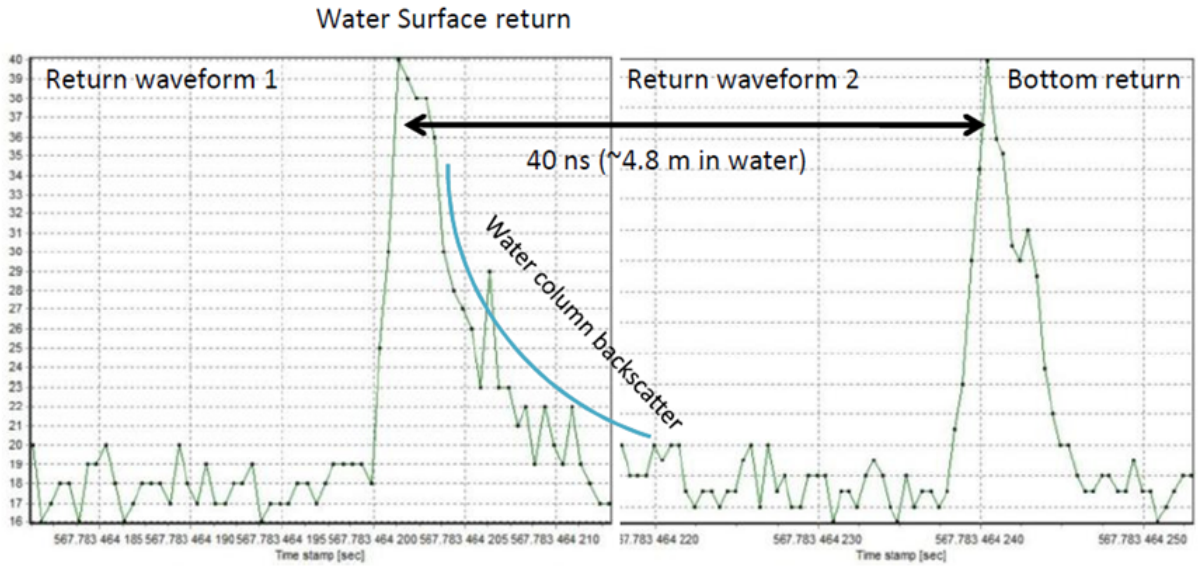

Figure 2.6: Data acquired with a conventional lidar bathymetry sensor, as presented at the 2013 International Lidar Mapping Forum [103]. The voltage output by the photodetector is digitized, typically at rates on the order of 1 GHz as shown here. A measurement of water depth is provided by differencing the time stamp of each apex in the photodetector output waveform, accounting for the refractive index of water.

speed of the acquisition electronics. Invariably, modern techniques for resolving shallow depth in semitransparent media are constrained by the governing time responsivity of the system, resulting in ambiguities between overlapping returns from sequential media surfaces and rendering depth indeterminable (refer to Figure (1.2) at right) [110]. Conventional bathymetry lidar sensors ranging through shallow waters are typically limited to meter-level depth measurements [59], with more complex systems working to achieve sub-meter resolution [81, 102].

> ***"The problem arises due to an inability to distinguish between the surface and the bottom return pulses when they are very close together in time."***
> **Nathan Quadros**, Department of Sustainability and Environment, Australia

As a result of the pulse overlap ambiguity, the shallow water regime remains largely unresolved by conventional lidar bathymetry sensors [9, 111, 110]. As noted by Lillycrop [85], "shoreline surveying can become very difficult when delineating where the land ends and the water begins." Quadros [115] discusses the operation of a lidar bathymetry sensor over a beach scene. For a wide, flat beach, "the bathymetric lidar system will likely struggle to acquire dependable depth measurements...the problem arises due to an inability to distinguish between the surface and the bottom return pulses when they are very close together in time."

As demonstrated in Figure (2.7), the pulse overlap limitation results in significant gaps in ALB data acquired over shallow water scenes [10, 136, 138]. Enhanced performance of the sensor in the shallow media regime demands a reduction of the governing time responsivity, often at the expense of increased complexity and cost associated with high performance components such as picosecond pulse width lasers and fast detectors. Pursuit of an alternative, more sophisticated approach to overcoming the pulse overlap limitation has motivated the dissertation research and is detailed in the following chapters.

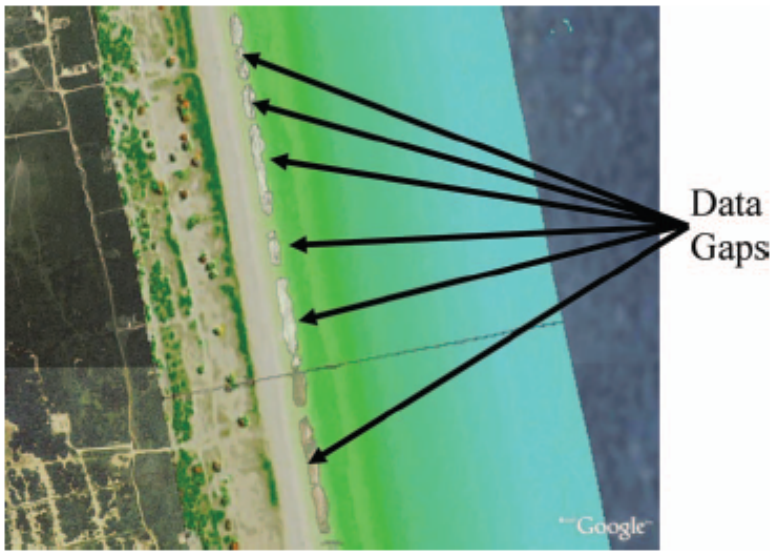

Figure 2.7: Typical SHOALS bathymetry coverage superimposed onto a Google Earth image, taken from [10]. The sensor is unable to resolve between surface and bottom returns received from regions of shallow water, resulting in significant data gaps in the littoral zone.

2.6 Case Study: Remote Sensing of Supraglacial Melt Lakes

Greenland both indicates and reacts to climate. Research in Greenland has indicated a steady rise in average temperatures, correlated with an increase in summer meltwater extent [1, 132], duration, runoff [20], and outlet glacier discharge velocities [117]. The Greenland Ice Sheet (GIS) covers approximately 1.7 million km^2, is upwards of 3 km thick [42], and flows outward from its interior through a combination of internal deformation, deformation of underlying sediments [19], and sliding at the ice-bedrock interface [74, 35]. What happens to this barren land has global implications, as there is enough frozen liquid stored within the GIS to raise the global sea level by 6 meters if the ice sheet melted completely [42, 84]. Scientists are discovering that as the climate of Greenland continues to warm, the ice sheet accelerates, driven by forces deep underground. They warn that at the current rate of melting, within a few decades rising seas will have a profound effect on the low-lying countries of the world.

> ***"2.8 million km^3 of ice in Greenland. If it all melted, it would raise [global] sea level by 6 meters."***
> **Dave Levitan**, 2013 IEEE Spectrum

During the summer months in the ablation zone, surface melting results in the formation of supraglacial melt lakes, an example of which is shown in Figure (2.8). While the ice and snow cover of the winter months reflects close to 80% of the incident solar radiation, summer melt waters *absorb* close to 80% of the sunlight [95]. As the depths of the lakes increase, scattering and absorption reduce the reflectance of incident solar radiation, enhancing the albedo feedback mechanism [88] and amplifying insidious melt of surface ice [21]. In time, water stored in the melt lakes penetrates through the GIS to the base via the formation of through-ice conduits and crevasses commonly referred to as moulins [82], draining subglacially into the sea as illustrated in Figure (2.9). These drainage events can occur rapidly in a matter of hours [35]. Models of fracture propagation through the GIS suggest that once initiated, the water-filled crevasses can propagate through the full thickness of the ice [133], as the rate of ice crack propagation is limited only by

the melt water supply required to fill the fracture [133]. The addition of surface melt water to the bedrock transfers heat and lubricating fluid to the glacier base and increases basal sliding of the GIS, providing a localized mechanism for response of the ice sheet to climate change via increased velocity of outlet glacier discharge [130]. The flow rates of many glaciers have doubled over a recent 5 year period [42, 121], increasing the volume of water and ice deposited into the ocean and underscoring the demand to better understand the dynamics of GIS mass balance and implications for the global sea level budget.

Though the formation of melt lakes in the warmer months is not a new phenomena, the relationship between the ablation region and supraglacial lake development is not yet comprehensively understood [87]. Melt lakes are developing more frequently and at higher elevations each summer. The waters of melt lakes can be as shallow as single centimeters [141], while meter-deep meltponds have been witnessed to drain in a matter of hours [35], resulting in highly dynamic shoreline development and transport of melt water. However, depth and volume statistics for supraglacial melt lakes, including their time variation, remain unresolved [21].

A suite of existing active and passive noncontact sensors have provided initial estimates of supraglacial lake volume from ground, airborne, and space-based platforms. Data from satellites such as the Moderate-Resolution Imaging Spectroradiometer (MODIS) [75] and Advanced Spaceborne Thermal Emission and Reflection Radiometer (ASTER) [144] have been utilized to examine the water-depth-driven solar radiation extinction effect on the surface reflectance of melt lakes in an effort to determine temporal changes in the volume of water stored in supraglacial lakes [21, 49, 62, 92, 127, 128, 130], at the expense of poor spatial resolution (e.g. 250 m x 250 m spatial resolution for MODIS) and limited spatial coverage constrained by the satellite orbit. Airborne campaigns have provided promising preliminary depth information using airborne laser altimeter data [92] and digital imagery [21] at increased spatial resolution. In-situ measurements with sonar sensors have been collected for a small quantity of supraglacial lakes [21, 35, 87, 131], with enhanced spatial resolution but poor coverage typically limited by logistical challenges.

Figure 2.8: Aerial view of a supraglacial melt lake on the GIS, taken from [90].

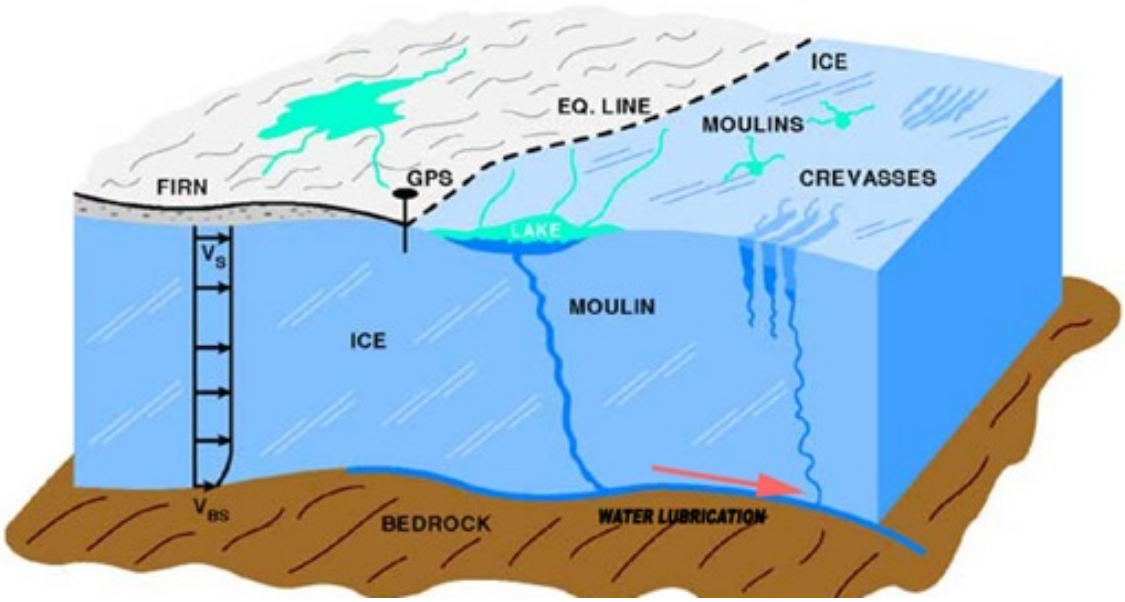

Figure 2.9: Diagram of glaciological features involved in the formation and drainage of supraglacial melt lakes, taken from [145]. Water drained from supraglacial melt lakes propagates through the GIS via moulins to the bedrock, leading to enhanced basal lubrication.

Demand exists within the science community for the development of a new generation of sensor technologies capable of providing enhanced spatial resolution of supraglacial lake volume estimates, with sufficient depth resolution to obtain water depth measurements downwards of single centimeters while maintaining deep water capabilities, in order to acquire comprehensive depth data of melt waters and facilitate further study of supraglacial lake dynamics. These data will enable the community to further resolve how ice sheet melt runoff and glacier discharge contribute to global sea level rise, providing additional insight into the impact of global climate warming.

While lidar bathymetry possess great potential to resolve supraglacial lake depth and volume estimates, the limitation imposed by the governing time responsivity of conventional lidar sensors is amplified when considering application to this extremely shallow water environment. For example, Allouis et. al. [4] simulate a lidar sensor with minimum resolvable depth of 0.41 m. A single supraglacial lake nominally 1 km in diameter and 0.41 m deep contains 1287400 m^3 of unaccounted water volume, roughly double the volume of oil spilled into the Gulf of Mexico during the 2010 BP event [43]. Taking into account the potential for rapid drainage of supraglacial lakes in the matter of hours [35], remote investigation of dynamic shoreline areas is limited by existing ALB technologies.

2.7 Sensor Development

Historically, the ALB community has resigned itself to operating within the scalar lidar approach of Equation (2.1). With a heritage of nearly 50 years of range-resolved observations through water to its credit, the scalar approach has successfully provided the timing information required to identify range from the sensor to the water surface and bottom, and subsequently provide a water depth measurement. However, change is brewing within the lidar bathymetry community. When designed appropriately, in addition to timing information the detected optical signals also contain polarization information that can be examined to evaluate the scattering properties of the target media. As demonstrated in the following chapters of the dissertation, the sensor can be configured to effectively code the transmitted laser pulse with a polarized electric field and,

depending on the scattering properties of the media, the received backscattered signals can contain preserved and modified versions of the transmitted code which are decoded in the receiver. This additional data, largely disregarded by conventional lidar bathymetry sensors, can be evaluated to provide additional information beyond the range measurement, such as to differentiate between surface types by measuring the propensity of the surface to depolarize the incident light into the perpendicular polarization plane [118].

Chapter 3

Theory

3.1 Introduction

This chapter provides a mathematical formulation of the polarization lidar approach developed in the dissertation research, including descriptions necessary to understand the measurements and analyses presented in following chapters.

3.2 Polarization in Range-Resolved Observations

At any instant in time, the electric field vector of an electromagnetic wave can be characterized by its orientation. The orientation can be fixed, as in the case of linear polarization, rotating as with circular and elliptical polarizations, or randomly oriented in the case of unpolarized radiation. Lasers incorporated into pulsed TOF sensors typically output linearly polarized light due to the crystalline nature of the lasing media. As a result, the conventional polarization lidar operates by transmitting a linearly polarized laser pulse and detecting the parallel and perpendicular planes of polarization of the received scattered light [137]. Additional optics can be inserted into the optical path for transmission of circularly polarized light, depending on the application [12, 47]. This approach generates two measurements, described by two equations in the form of Equation (2.1), one describing the received intensity in the parallel detection channel and one describing the perpendicular detection channel. The received signals provide the time of flight information required to resolve range between the sensor and target. The ratio of the received signals, commonly referred to as the depolarization ratio, also provides information regarding scattering properties of

the target, such as asphericity and surface roughness.

This approach has a rich heritage in atmospheric lidar in the study of aerosols, clouds, and precipitation [15, 24, 41, 120]. Preliminary efforts have been made to utilize polarization lidar for range-resolved observations through semitransparent media. In lidar bathymetry, analyses of the polarization orientations of received signals have been used in the study of fish schools [30, 32] and to identify submerged targets [26, 50, 94]. The polarization-preserving nature of the water surface and volume, as well as the depolarizing nature of rough bottom topographies, has been demonstrated [29, 135]. Figure (3.1) illustrates this phenomena in the depth profiles of parallel and perpendicular oriented scattered signals received by a lidar bathymetry sensor in a near-shore region of the Pacific Ocean. The ratio of signals in the parallel and perpendicular detection channels demonstrates the polarization-preserving nature of the water surface (z = 0 m) and volume, while received signals scattered from the bottom (z = 22 m) suggest strong depolarization.

The conventional approach to polarization lidar is limited, however, in that the ratio of the parallel and perpendicular received signals cannot measure phase and therefore does not fully characterize the received polarization state. Range-resolved observations give quantitative description as to *how much* the transmitted polarization orientation has changed, but it is ambiguous as to *how* the polarization changed. As a result, the measurement cannot provide a general connection to the scattering phase matrix of the semitransparent media.

3.3 The Stokes Vector Lidar Equation

Unlike the conventional scalar approach presented in Equation (2.1), polarization lidar is most completely described by the Stokes Vector Lidar Equation (SVLE), developed in [64, 68] initially for application to atmospheric lidar observations, according to

$$\vec{S}_{RX}(R) = \mathbf{M_{RX}}\left[\left(G\left(R\right)\frac{A}{R^2}\Delta R\right)\mathbf{T_{atm}}\left(\vec{k}_s, R\right)\mathbf{F}\left(\vec{k}_i, \vec{k}_s, R\right)\mathbf{T_{atm}}\left(\vec{k}_i, R\right)\mathbf{M_{TX}}\vec{S}_{TX} + \vec{S}_B\right] \quad (3.1)$$

where $\vec{S}_{RX}$ is the received Stokes vector, $\vec{S}_{TX}$ is the Stokes vector describing the transmitted laser polarization state, $\mathbf{M_{TX}}$ is the Mueller matrix description of the optical path of the lidar

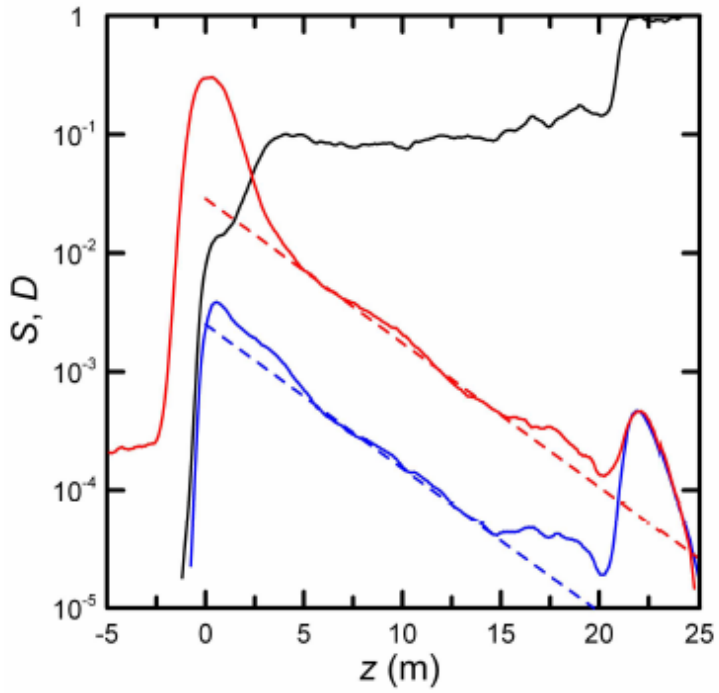

Figure 3.1: Preliminary efforts have been made to incorporate polarization lidar techniques into lidar bathymetry. Here, depth profiles of co- (red) and cross-polarized (blue) receiver measurements for received scattered signals from the water and floor of a near-shore ocean region indicate the polarization-preserving nature of the water surface and depolarization due to rough bottom topography, taken from [29].

transmitter, $\mathbf{T_{atm}}\left(\vec{k}_i, R\right)$ is the Mueller matrix describing transmission between the sensor and target through the atmosphere along the incident wave vector $\vec{k}_i$ over the range R, $\mathbf{F}\left(\vec{k}_i, \vec{k}_s, R\right)$ is the scattering phase (Mueller) matrix of the target at range R for incident and scattered wave vectors $\vec{k}_i$ and $\vec{k}_s$, respectively, ΔR is the sensor range resolution, A is the receiver aperture, $G(R)$ is the geometrical overlap function of the sensor, $\mathbf{M_{RX}}$ is the Mueller matrix description of the optical path of the lidar receiver, and $\vec{S}_B$ is the Stokes vector of the background at the input of the receiver. The Stokes vectors and Mueller matrices described within the SVLE are not normalized so that overall scattering and system efficiency may be found in the (1,1) element of the Mueller matrix and intensity is carried in the first element of the Stokes vector.

Within the SVLE approach, the transmitted laser polarization orientation is propagated along the entire optical path, allowing for interaction with multiple matrices before it is collected and analyzed in the receiver [28]. This description is fully general for direct detection lidar and allows for complete analysis and understanding of polarization effects along the optical path that otherwise may not be properly described using the conventional scalar approach to polarization lidar in Equation (2.1).

3.4 Polarization in Range-Resolved Observations of Shallow Media Depth

Equation (3.1) describes the Stokes vector $\vec{S}_{RX}$ received from a distant target with scattering matrix defined by $\mathbf{F}\left(\vec{k}_i, \vec{k}_s, R\right)$. This form of the SVLE has successfully demonstrated range-resolved observations of atmospheric phenomena including depolarization by polar mesospheric clouds [65, 66, 67, 64] and diattenuation of horizontally oriented ice crystals [105]. The SVLE is further developed in this dissertation research for application to range-resolved observations through semitransparent media. Within this framework, the SVLE consists of N subequations, each describing the Stokes vector $\vec{S}^N_{RX}$ received by the sensor from Nth semitransparent media bounding surface.

The setup for the measurement is illustrated in Figure (3.2). A laser pulse of temporal width τ is transmitted from the sensor at time t_0 through media with refractive index n_0 (typ. air

with $n = 1.00$ for ALB sensors) towards a distant semitransparent media. The pulse intercepts the first surface with scattering matrix $\mathbf{F}_1$ at time t_1. A portion of the laser pulse $\mathbf{1}$ is scattered at the surface back to the instrument. The remaining portion of the laser pulse is transmitted into the media with refractive index n_1. A portion of the transmitted energy $\mathbf{N}$ is scattered at the sequential surface defined by the scattering matrix $\mathbf{F}_N$ at time t_N and propagates back to the receiver. The sequence repeats for sequential semitransparent media of refractive index n_N bounded by N surfaces. Depth measurement between surfaces is based on the differential arrival times of the range-resolved received signals, accounting for differences in refractive index along the optical path and laser pointing angle relative to the surface normals.

Within this framework, Equation (3.1) is further developed to describe range-resolved observations through semitransparent media according to

$$\vec{S}_{RX}^{N}(R) = \mathbf{M_{RX}}\left[\left(G\left(R\right)\frac{A}{R^2}\Delta R\right)\prod_{i=0}^{N-1}\mathbf{T_{n_i}}\left(\vec{k}_s,R\right)\prod_{i=1}^{N}\mathbf{T_{F_i}}\left(\vec{k}_s,R\right)\mathbf{F_N}\left(\vec{k}_i,\vec{k}_s,R\right)\prod_{i=1}^{N}\mathbf{T_{F_i}}\left(\vec{k}_i,R\right)\prod_{i=0}^{N-1}\mathbf{T_{n_i}}\left(\vec{k}_i,R\right)\mathbf{M_{TX}}\vec{S}_{TX}+\vec{S}_B\right] \tag{3.2}$$

where $\vec{S}_{RX}^{N}$ is the received Stokes vector from the Nth surface, $\mathbf{T_{n_i}}$ is the Mueller matrix description of transmission through media with refractive index n_i, $\mathbf{T_{F_i}}$ is the Mueller matrix description of transmission through the media surface defined by the scattering matrix $\mathbf{F_i}$, $\mathbf{F_N}\left(\vec{k}_i,\vec{k}_s,R\right)$ is the scattering phase matrix of the Nth media surface at range R for incident and scattered wave vectors $\vec{k}_i$ and $\vec{k}_s$, and all remaining terms are described as in Equation (3.1). The $\mathbf{F}\left(\vec{k}_i,\vec{k}_s,R\right)$ term previously used to describe a single surface is now replaced by $\mathbf{F_N}\left(\vec{k}_i,\vec{k}_s,R\right)$ to describe the scattering matrix of N sequential media surfaces, where each sequential scattering matrix $\mathbf{F_N}$ accounts for transmission along the optical path through previous interfaces and media.

As an illustrative example, the received Stokes vector $\vec{S}_{RX}^{2}$ from the second ($N = 2$) semitransparent media surface with scattering matrix $\mathbf{F_2}$ is defined according to

$$\vec{S}_{RX}^{2}(R) = \mathbf{M_{RX}}\left[\left(G\left(R\right)\frac{A}{R^2}\Delta R\right)\mathbf{T_{n_0}}\mathbf{T_{F_1}}\mathbf{T_{n_1}}\mathbf{F_2}\mathbf{T_{n_1}}\mathbf{T_{F_1}}\mathbf{T_{n_0}}\mathbf{M_{TX}}\vec{S}_{TX}+\vec{S}_B\right] \tag{3.3}$$

where the incident and scattered wave vectors have been omitted for brevity, $\mathbf{T_{F_1}}$ describes the Mueller matrix for transmission along the optical path through the first surface, and $\mathbf{T_{n_{0,1}}}$ are the

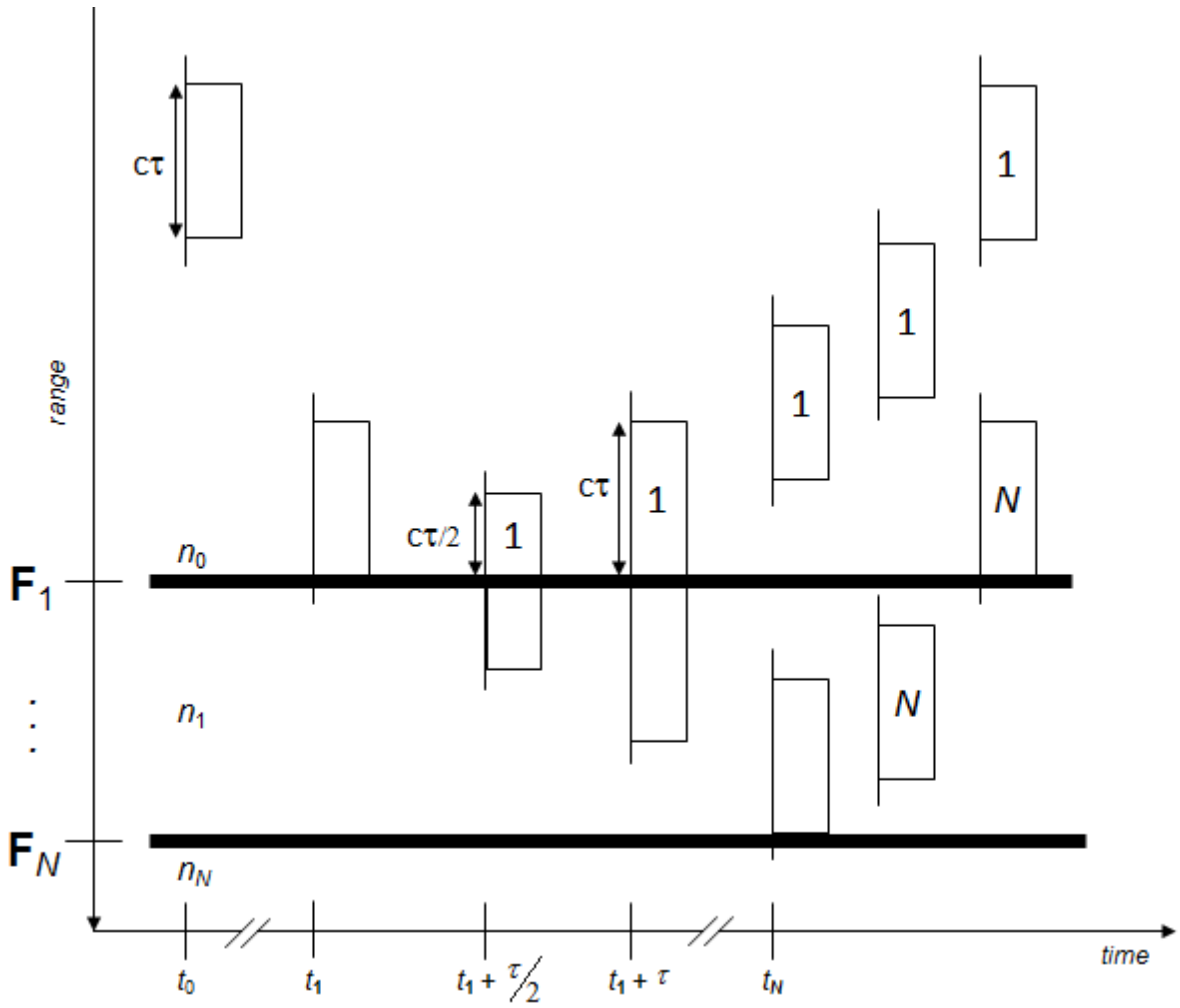

Figure 3.2: Timing diagram for range-resolved observations through semitransparent media bounded by N surfaces.

Mueller matrix descriptions for transmission through media with refractive indices $n_{0,1}$. Evaluation of Equation (3.3) provides a complete description of the received Stokes vector from the second semitransparent media surface, accounting for all polarization effects along the optical path.

3.5 Range-resolved Observations of Distant Shallow Media Depth

The development of the SVLE presented in Equation (3.2) provides the comprehensive framework for noncontact optical sensing of range through distant semitransparent media by accounting for polarization effects along the entire optical path. Further description of each contributing polarization component is provided in this section.

3.5.1 Transmit Polarization

The polarization orientation of the transmitted laser pulse is described by the Stokes vector $\vec{S}_{TX}$ according to [52]

$$\vec{S}_{TX} = \begin{bmatrix} S_0 \\ S_1 \\ S_2 \\ S_3 \end{bmatrix} \tag{3.4}$$

where S_0 is the total intensity (photons), S_1 is the power in the horizontal/vertical linear polarization, S_2 is the power in the $\pm 45^\circ$ linear polarization, and S_3 is the power in the right- and left-hand circular polarizations. The relationship between the terms in Equation (3.4) can also be written in terms of physical parameters of the polarization orientation according to

$$\vec{S}_{TX} = N_{TX} \begin{bmatrix} 1 \\ p_{TX} \cos(2\varepsilon_{TX}) \cos(2\theta_{TX}) \\ p_{TX} \sin(2\varepsilon_{TX}) \cos(2\theta_{TX}) \\ p_{TX} \sin(2\theta_{TX}) \end{bmatrix} \tag{3.5}$$

where N_{TX} is the total photons in the transmitted laser pulse, p_{TX} is the laser degree-of-polarization (DOP) defined as

$$p_{TX} = \frac{\sqrt{S_1^2 + S_2^2 + S_3^2}}{S_0} \tag{3.6}$$

ε_{TX} is the linear rotation angle of the polarization and θ_{TX} is the ellipticity angle, as illustrated in Figure (3.3).

3.5.2 Transmitter Effects

After transmission from the laser head, the optical pulse passes through a transmitting optical system defined by the Mueller matrix $\mathbf{M_{TX}}$, often consisting of steering mirrors, wave plates and beam expanders. Depending on sensor design, these optical elements possess the potential to modify the polarization state of the transmitting laser signal. Thus particular attention must be paid to the design of transmitting optics. For existing sensors, it is often necessary to mitigate the polarization effects through incorporation of hardware and software compensation [65].

3.5.3 Transmission Through Media of Variable Refractive Index

For semitransparent media of refractive index n where higher order scattering effects are weak, single scattering may be assumed [13] such that the polarization state of the transmitted laser pulse is described by a single volume element between surfaces according to [64]

$$\mathbf{T_n}\left(\vec{k}_i\right) = \mathbf{F_{col}}\left(\vec{k}, \vec{k}, R\right) + \left(\mathbf{I} - \mathbf{E_{col}}\left(\vec{k}, R\right)\right) \tag{3.7}$$

where $\mathbf{F_{col}}\left(\vec{k}, \vec{k}, R\right)$ is the column integrated volume forward scattering matrix of the propagation medium through distance R for wave vector $\vec{k}$, $\mathbf{E_{col}}\left(\vec{k}, R\right)$ is the column extinction matrix of the path to or from the media and $\mathbf{I}$ is an identity Mueller matrix. The dissertation research assumes for single scattering during propagation through semitransparent media that extinction is polarization independent, as is common in atmospheric lidar applications [77], and the forward scattering coefficient is small compared to the unextinguished light such that

$$f_{11}^{col}\left(\vec{k}, \vec{k}, R\right) \ll \left(1 - e_{11}^{col}\left(\vec{k}, R\right)\right) \tag{3.8}$$

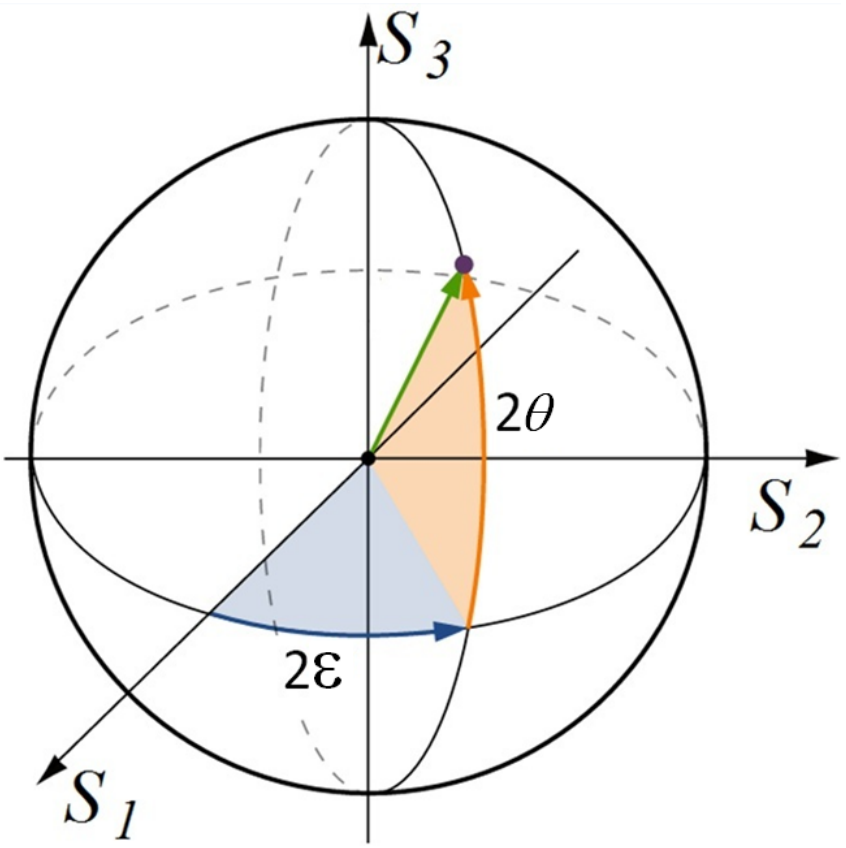

Figure 3.3: Diagram of a Stokes vector (green arrow) of arbitrary intensity, described by its linear rotation angle ε and ellipticity θ angle, modified from [139].

and the polarization effects of the media with refractive indices n along the transmit and receive optical paths may be ignored.

The framework for this assumption is illustrated in Equation (3.9), where the Mueller matrix describing the media along the optical path for a typical ALB sensor is polarization preserving, and a single β_n term is used to describe extinction along the optical path,

$$\mathbf{T_n} = \beta_n \begin{bmatrix} 1 & 0 & 0 & 0 \\ 0 & 1 & 0 & 0 \\ 0 & 0 & 1 & 0 \\ 0 & 0 & 0 & 1 \end{bmatrix} \tag{3.9}$$

where

$$\beta_n = e^{-k_n(\lambda)d_n} \tag{3.10}$$

describes the attenuation of the transmitted laser pulse along the optical path for attenuation coefficient k_n at wavelength λ over the media depth d_n.

3.5.4 Interaction with Media Surfaces

The scalar lidar approach offered in Equation (2.1) provides a simplistic description of the scattering properties of a semitransparent media surface, described in $\beta(\lambda)$ as a scalar quantity. Alternatively, the scattering effects of a media surface are most completely described by the scattering Mueller matrix $\mathbf{F}\left(\vec{k}_i, \vec{k}_s, R\right)$ provided in the SVLE approach. The Mueller matrix transforms and couples polarization orientations during the scattering process, rather than simply scaling modes corresponding to measured detection channels. As described in [27, 86, 119], the components of a realizable Mueller matrix in Equation (3.2) can be decomposed into a combination of retarders, diattenuators, and depolarizers according to

$$\mathbf{F} = \mathbf{M_R}\mathbf{M_D}\mathbf{M_\Delta} \tag{3.11}$$

where $\mathbf{M_R}$, $\mathbf{M_D}$, and $\mathbf{M_\Delta}$ describe the retarding, diattenuating, and depolarizing attributes of the scattering Mueller matrix, respectively. All three components have the capacity to couple

polarization modes during interaction with the scattering media surface.

The dissertation research described here pays particular attention to semitransparent media with bounding surfaces described by the depolarization matrix $\mathbf{M}_{\boldsymbol{\Delta}}$, since most natural and man-made media exhibit depolarization [36, 37] and prior work has demonstrated success exploiting depolarization in bathymetric laser ranging [29, 99]. Diattenuating and retarding surfaces could be considered for future exploration of semitransparent media.[1] The Mueller matrix for depolarization describes nondeterministic polarization systems [123]. Depolarization can be viewed as a reduction of the degree of polarization of light, in which polarized light is coupled into unpolarized light. Assuming the surfaces of the semitransparent media do not cause diattenuation or retardance, the scattering phase matrix assumes the form of a normalized depolarization matrix in the backscattered direction as [86, 47, 51]

$$\mathbf{F} = \mathbf{M}_{\boldsymbol{\Delta}} = \beta_F \begin{bmatrix} 1 & 0 & 0 & 0 \\ 0 & a & 0 & 0 \\ 0 & 0 & b & 0 \\ 0 & 0 & 0 & c \end{bmatrix} \tag{3.12}$$

where the reflectivity of the scattering surface is described by β_F and takes the form of a scattering coefficient, as illustrated in Figure (3.4), or a Fresnel reflection depending on the scattering process. The coefficients a, b, and c are the tendency of horizontal/vertical, $\pm 45°$, and right/left-hand circular polarizations to remain polarized, respectively. For semitransparent media surfaces that tend to preserve the polarization orientation of the incident light, the magnitude of a, b, and c are all approximately 1. Alternatively, for media surfaces that tend to modify the incident polarization through depolarization, such as the rough bottom topographies encountered in lidar bathymetry, these terms are generally of magnitude less than 1. A motivation for the dissertation research has been an understanding of the interaction of polarized laser light with distant semitransparent media and classification of bounding surfaces based on their propensity to depolarize the incident optical signal.

[1] The reader is directed to [64] for a detailed description of retarding and diattenuating effects described within the SVLE.

"A motivation for the dissertation research has been an understanding of the interaction of polarized laser light with distant semitransparent media and classification of bounding surfaces based on their propensity to depolarize the incident optical signal."

3.5.4.1 Water Surface

For lidar bathymetry sensors, the Mueller matrix descriptions for transmission through and reflection from the water surface are described mathematically by Fresnel's equations. For a pulse of laser energy incident upon the water surface, the Mueller matrix for reflection is defined according to

$$\mathbf{M_R} = \frac{1}{2}\left(\frac{\tan\theta_-}{\sin\theta_+}\right)^2 \times \begin{bmatrix} \cos^2\theta_- + \cos^2\theta_+ & \cos^2\theta_- - \cos^2\theta_+ & 0 & 0 \\ \cos^2\theta_- - \cos^2\theta_+ & \cos^2\theta_- + \cos^2\theta_+ & 0 & 0 \\ 0 & 0 & -2\cos\theta_+\cos\theta_- & 0 \\ 0 & 0 & 0 & -2\cos\theta_+\cos\theta_- \end{bmatrix} \tag{3.13}$$

for $\theta_\pm = \theta_i \pm \theta_r$, where θ_i and θ_r are the incident and refracted angles of the laser beam, respectively, defined according to Snell's Law. Similarly, the Mueller matrix for transmission is defined according to

$$\mathbf{M_T} = \frac{\sin 2\theta_i \sin 2\theta_r}{2\left(\sin\theta_+\cos\theta_-\right)^2} \begin{bmatrix} \cos^2\theta_- + 1 & \cos^2\theta_- - 1 & 0 & 0 \\ \cos^2\theta_- - 1 & \cos^2\theta_- + 1 & 0 & 0 \\ 0 & 0 & 2\cos\theta_- & 0 \\ 0 & 0 & 0 & 2\cos\theta_- \end{bmatrix} \tag{3.14}$$

Figure (3.5) provides a plot of the reflectance and transmittance for the surface of a water body, where the laser pulse transmits through media with $n = 1.00$ to a sequential media with $n = 1.33$. For the lidar bathymetry sensor developed in the dissertation, in which the transmitted

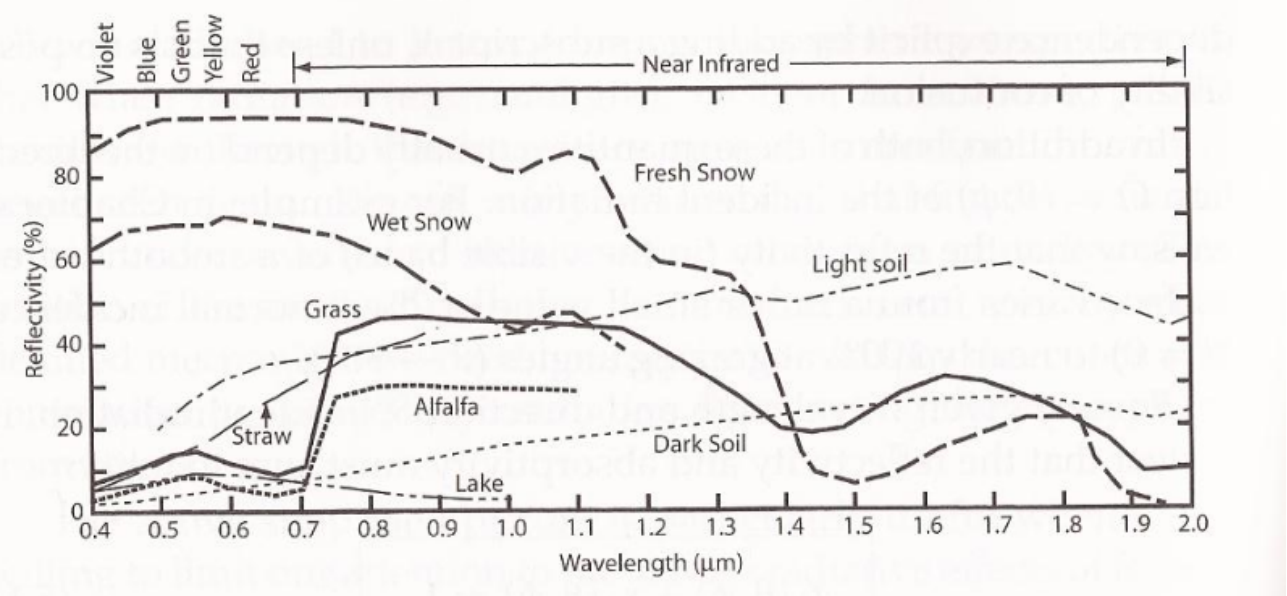

Figure 3.4: Reflectivity of typical natural bounding surfaces of semitransparent media for incident shortwave radiation, taken from [113].

laser light is constrained within $\pm 20^{\circ}$ of nadir due to expected aircraft flight profiles, the transmitted and received intensities are approximately 98% and 2%, respectively, for a smooth water surface.

The diameter of a water molecule is approximately $2.75\mathring{A}$ [25], three orders of magnitude smaller than the probing 532 nm lidar wavelength. To the lidar, liquid water is a Rayleigh scattering environment and depolarization from the water column is negligible [25, 137]. Turbid waters and subsurface particulates tend to introduce depolarization into the scattering process, as described in additional detail in the following subsection. For smooth water not roughened by wind, most surface facets are co-planar and horizontal, resulting in an intense Fresnel specular return for incident laser pulses oriented near-nadir and a rapid fall-off of backscattered energy at small off nadir angles [63].

During typical operation of an ALB sensor, however, the water surface tends to behave like a distorted mirror surface due to the presence of surface winds, such that the incident laser light is not reflected in a single direction but rather is scattered in a variety of directions, depending on the local slope of wave platelets where each light ray encounters the surface [22, 113]. For a wind-roughened water surface, the majority incident optical radiation is scattered in a narrow cone of angles surrounding the specular reflection. As the roughness of the water surface increases, the incident laser light is scattered into a wider cone until the reflected radiation is scattered almost uniformly in all directions. Waves formed on the surface tend to exhibit large scale roughness compared to the incident laser wavelength, as illustrated in Figure (3.6), with negligible small scale roughness due to surface tension of the water. Since the surface roughness is not constructed on the scale of the incident laser wavelength [116], the water surface remains polarization-preserving and the corresponding f_{22} element of the scattering matrix is approximately 1. In this sense, enhanced surface roughness tends to scatter incident laser light outside of the receiver optical path, decreasing signal levels registered by the photodetector, with negligible depolarization.

3.5.4.2 Water Bottom

Following transmission through the air/water interface, the remaining 98% of the incident laser signal is refracted into the water column with polarization orientation described by the trans-

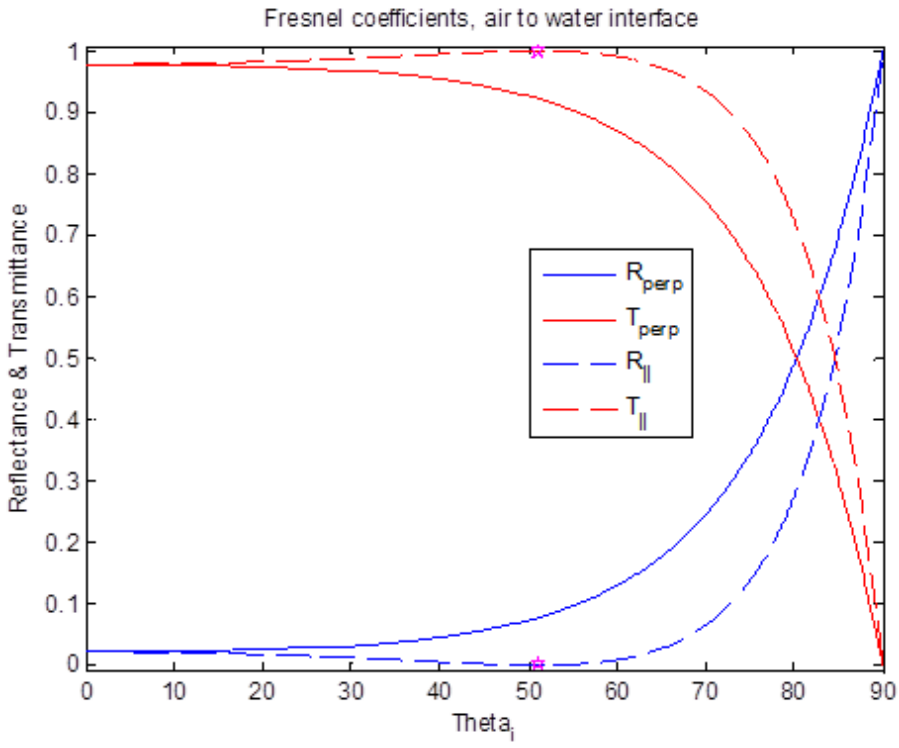

Figure 3.5: Intensity of the transmitted and reflected optical signals for polarized light incident upon a smooth air/water interface.

mitted Stokes vector. The depth of penetration is limited by extinction along the optical path through water, which is a function of the transmit wavelength and attenuation due to the water volume and particulates along the path, as defined in Equation (3.10). Provided sufficient laser energy is transmitted into the water column to overcome extinction losses, a portion of the transmitted energy incidents and scatters from the bottom. The majority of bottom surfaces encountered in bathymetric environments, such as sand and ice, exhibit small scale surface roughness on the order of the incident laser wavelength, as illustrated in Figure (3.6). These surface features result in diffuse scattering and subsequently tend to depolarize the incident polarized laser light [11, 134].

Due to their crystalline structure (ice for example), the majority of bottom surfaces inherently possess a degree of randomness in angle of incidence and path length on the scale of the incident wavelength. Photons propagating through the water incident different sections of the bottom, each randomly oriented at the wavelength scale. Each photon is subjected to a differential phase shift imposed by scattering from random sections of the bottom, randomizing the orientation of the electric field vector describing the scattered light [28, 60]. In the limit of a completely depolarizing surface ($f_{22} = 0$), the electric field vector of the scattered signal is randomly oriented.

Thus, photons incident upon the bottom tend to lose their polarization information as a result of scattering from the rough surface. The corresponding f_{22} element of the scattering matrix defining a depolarizing bottom is typically < 1. Evaluation of the f_{22} element by the lidar sensor permits classification of semitransparent surfaces based on the relative propensity of the surface to depolarize the incident laser signal and can therefore be used to characterize submerged surfaces.

3.5.5 Receiver Effects

Scattered signals input to the lidar receiver typically transmit through an optical path defined by $\mathbf{M_{RX}}$, often consisting of steering mirrors, etc., in similar fashion to the sensor transmitter. Depending on the sensor configuration, these optical elements also have the potential to modify the polarization state of the transiting light. Therefore it is often again necessary to cancel the polarization effects through hardware and software compensation, in particular for existing sensors

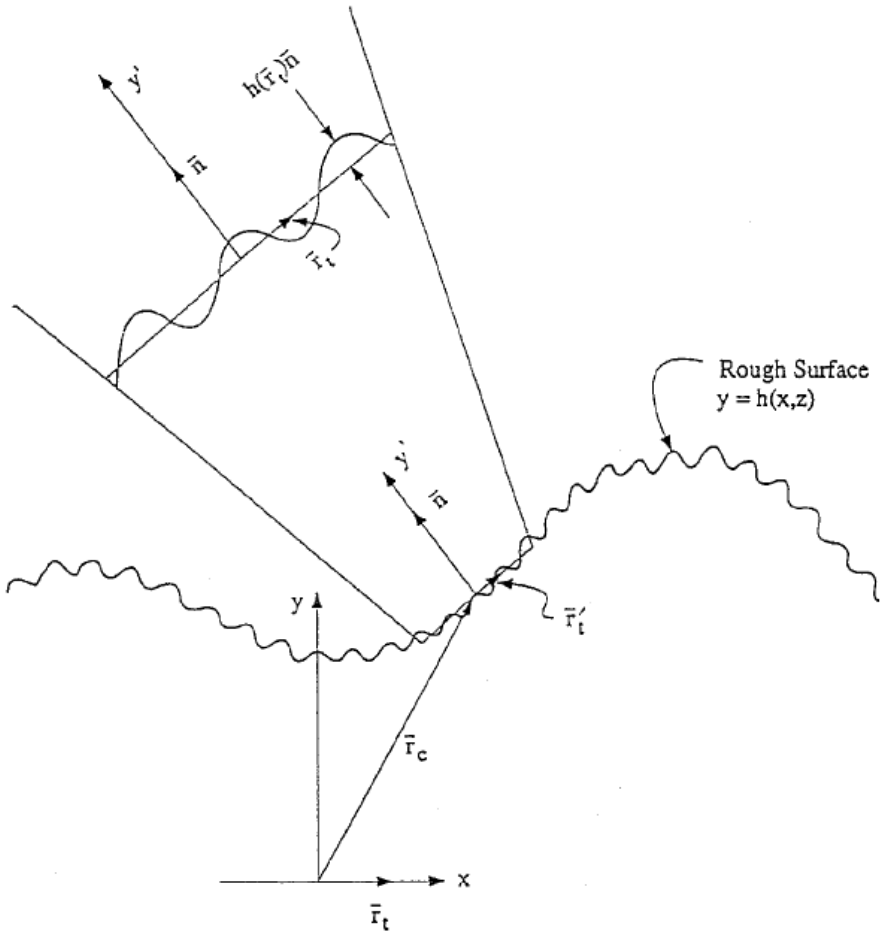

Figure 3.6: Illustration of the large and small scale surface roughness of an arbitrary semitransparent media surface, taken from [11]. Media surfaces defined by a rough surface mean height $h(\overline{r})\overline{n}$ on the order of the incident laser wavelength, such as ice, tend to depolarize the incident laser light. Typically, surfaces of clear waters encountered by ALB sensors are defined by large scale roughness $h(x, z)$ excited by surface winds, with negligible small scale roughness in the absence of turbidity, and tend to preserve the incident laser polarization orientation.

[65, 66].

3.5.6 Background

The background contribution $\vec{S}_B$ is the product of the background Stokes vector and the receiver projection matrix. The background Stokes vector is most generally described according to

$$\vec{S}_B = N_b \begin{bmatrix} 1 \\ p_b \cos(2\varepsilon_b)\cos(2\theta_b) \\ p_b \sin(2\varepsilon_b)\cos(2\theta_b) \\ p_b \sin(2\theta_b) \end{bmatrix} \tag{3.15}$$

where N_b describes the total photons incident on the photodetector when no polarization analyzer is present in the receiver, p_b is the DOP of the background light, ε_b is the linear orientation of the polarization component of background light, and θ_b is the ellipticity angle of the background. When the background light is input to and passed through the receiver Mueller matrix $\mathbf{M_{RX}}$, the total background counts incident on the photodetector are given by the product of $\mathbf{M_{RX}}$ and Equation (3.15).

3.6 Laboratory Demonstration

Initial laboratory experiments highlighted the benefit of the SVLE approach to range-resolved observations through semitransparent media. In addition to timing information, the detected optical signals also contain polarization information about the media that can be utilized to discriminate between surfaces. Using the laboratory setup of Figure (3.7), received scattered signals were observed on a 4 GHz oscilloscope. The emission from a pulsed laser operating at 532 nm was aligned and transmitted into a tube partially filled with water. The bottom of the tube initially consisted of a smooth plastic substrate, then a submerged ice substrate.

Received scattered signals were aligned through a polarizer, free to rotate about the optical axis, prior to collection by a photomultiplier tube, the output of which was displayed on the oscilloscope. The results in Figure (3.8) illustrate the observed signals from (a) the water surface

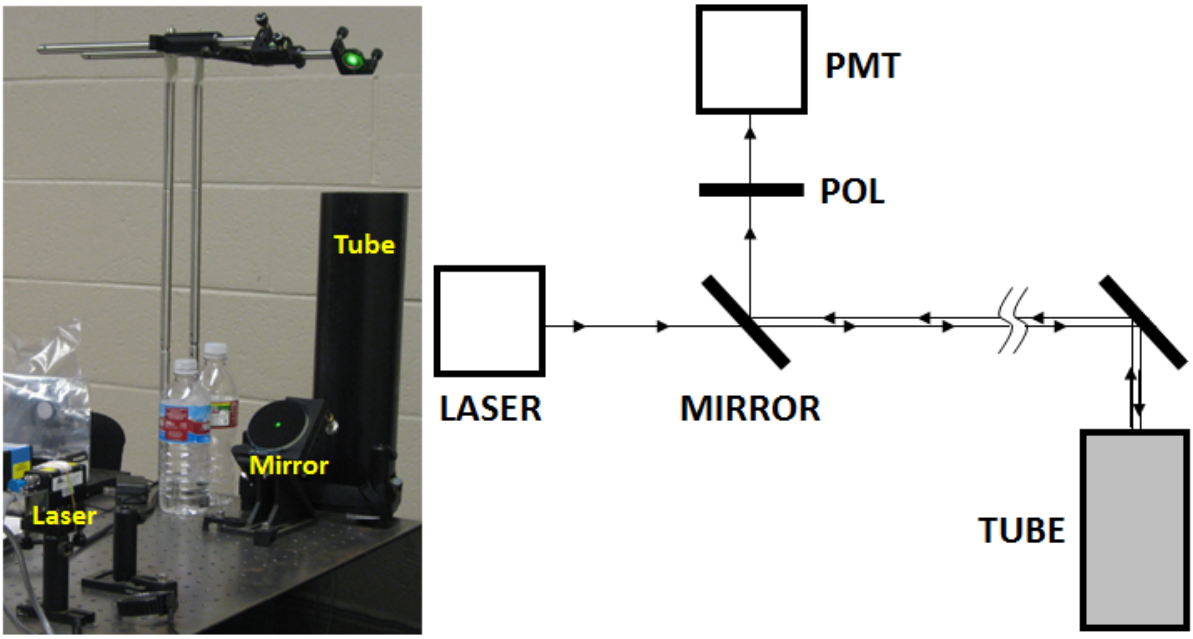

Figure 3.7: Setup for the initial laboratory demonstration to illustrate the potential of the SVLE approach to classify scattering surfaces. A pulsed laser operating at 532 nm is transmitted through a series of mirrors into a plastic tube partially filled with water. Scattered signals are passed through a rotating polarizer prior to detection by a photomultiplier tube.

and bottom of the tube, and (b) the water surface and submerged ice substrate, with the polarizer oriented to 0° and 90° for reception of co- and cross-polarized signals, respectively. For a surface and bottom defined by a polarization-maintaining scattering matrix ($f_{22} \approx 1$), the received signals are suppressed with the polarizer oriented to 90°. However, due to the capacity of the ice substrate to decouple the incident polarized laser light ($f_{22} < 1$), the cross-polarized component continues to register output on the PMT even with the polarizer oriented to 90°. This initial laboratory experiment demonstrated the potential of the SVLE approach to classify scattering surfaces, and further motivated the research presented in the following chapters.

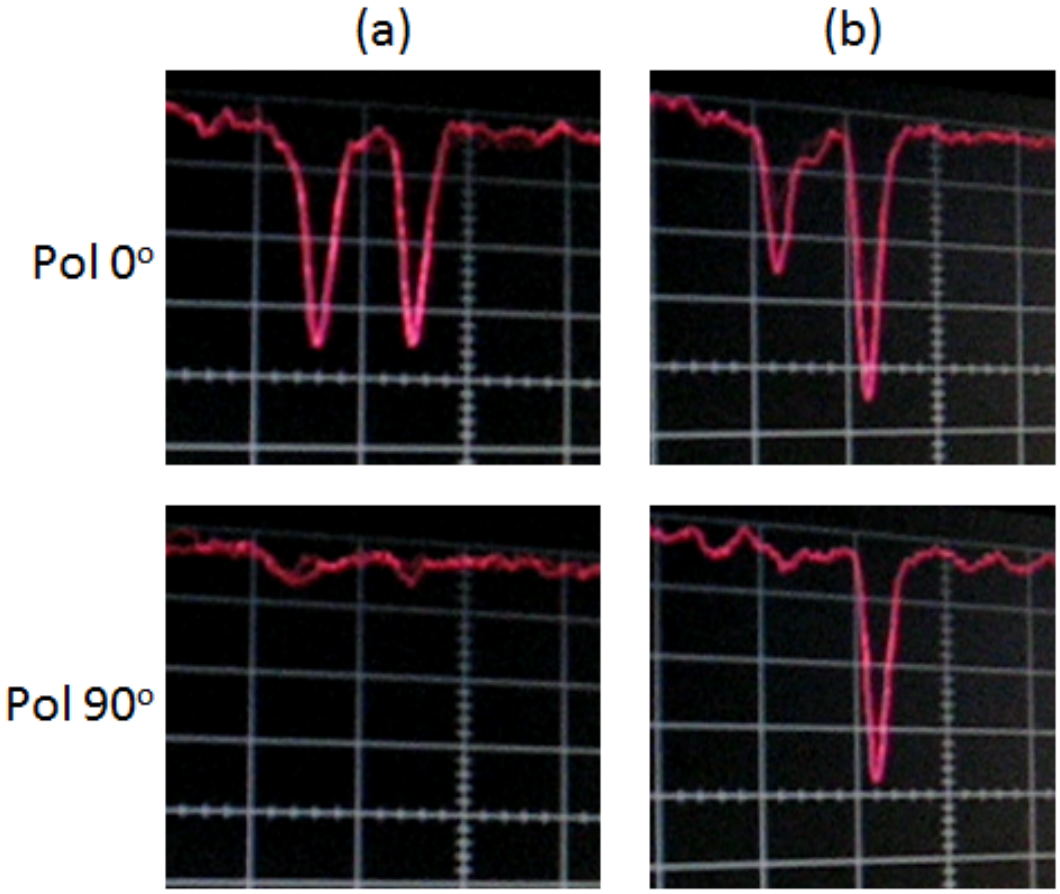

Figure 3.8: Screenshots of the photomultiplier voltage output as viewed on a 4 GHz oscilloscope. The target consisted of a tube filled with (a) water atop a submerged smooth plastic substrate, and (b) water atop a submerged ice substrate. Due to the polarization-preserving nature of the water surface and plastic substrate, received scattered signals are suppressed by the polarizer in the receiver when the polarizer is oriented 90° to the transmitted laser plane. However, the depolarizing nature of the submerged ice substrate decouples the incident laser energy and permits range observation regardless of polarizer orientation.

Chapter 4

Detection

4.1 Introduction

This chapter details the detection approach for range-resolved observations through semi-transparent media described within the framework of the SVLE. The lidar sensor is configured to evaluate media surfaces with scattering matrices defined with variable levels of depolarization, providing a measurement of range as well as an estimate of depolarization that can be used to discriminate between and classify surfaces.

4.2 Photoelectron Generation

The polarization orientation of laser ranging signals cannot be measured directly. Characterization of the received Stokes vector $\vec{S}_{RX}$ requires a series of scalar measurements. The optical path of the lidar receiver must incorporate a polarization analyzer to project the polarization orientation of the received scattered signal onto an axis of the Poincare sphere (Figure (3.3)) and measure the resulting intensity with a photodetector. Each projection generates a resultant photodetector intensity that can be used to reconstruct $\vec{S}_{RX}$. The measured intensity from the Nth surface of a semitransparent media is described in conjunction with Equation (3.2), as

$$\vec{N}^N = \mathbf{O}\vec{S}^N_{RX} \tag{4.1}$$

where $\vec{N}^N$ is a vector of the photoelectron counts (intensity) generated by the photodetector from signals scattered from the Nth media surface in each observed detection channel according to

$$\vec{N}^N = \begin{bmatrix} N_1^N \\ N_2^N \\ \vdots \end{bmatrix} \tag{4.2}$$

and $\mathbf{O}$ is the output projection matrix corresponding to the $\vec{N}^N$ measurements written as

$$\mathbf{O} = \mathbf{o} \begin{bmatrix} \mathbf{P_1} \\ \mathbf{P_2} \\ \vdots \end{bmatrix} \tag{4.3}$$

where $\mathbf{P_n}$ is the nth projection matrix corresponding to the nth detection channel and

$$\mathbf{o} = \begin{bmatrix} \eta_1 & 0 & 0 & 0 & 0 & 0 & 0 & 0 & \\ 0 & 0 & 0 & 0 & \eta_2 & 0 & 0 & 0 & ... \\ & & & & \vdots & & & & \end{bmatrix} \tag{4.4}$$

where η_n is the nth channel detection efficiency. The matrix $\mathbf{o} = \begin{bmatrix} 1 & 0 & 0 & 0 \end{bmatrix}$ denotes that only the S_0 (intensity) element of the received Stokes vector is directly measured by the photodetector. For conventional lidar sensors ranging through semitransparent media with a polarization indiscriminate detection approach, $\mathbf{O}$ simplifies to $\begin{bmatrix} \eta & 0 & 0 & 0 \end{bmatrix}$.

For a lidar evaluating a scattering phase matrix dominated by linear depolarization, two measurements are required: the parallel and perpendicular components of the received scattered signal. For received signals scattered from the Nth media surface, the resulting photoelectron counts (intensities) are given by

$$\vec{N}^N = \begin{bmatrix} N_\perp^N \\ N_\parallel^N \end{bmatrix} \tag{4.5}$$

and

$$\mathbf{O} = \mathbf{o} \begin{bmatrix} \mathbf{P}_\perp \\ \mathbf{P}_\parallel \end{bmatrix} \tag{4.6}$$

where $\mathbf{P}_\perp$ and $\mathbf{P}_\parallel$ are the 4 x 4 Mueller matrix descriptions of perpendicular and parallel polarizers

in the receiver optical path, respectively, defined according to

$$\mathbf{P}_{\perp} = \begin{bmatrix} 1 & -1 & 0 & 0 \\ -1 & 1 & 0 & 0 \\ 0 & 0 & 0 & 0 \\ 0 & 0 & 0 & 0 \end{bmatrix} \tag{4.7}$$

and

$$\mathbf{P}_{\parallel} = \begin{bmatrix} 1 & 1 & 0 & 0 \\ 1 & 1 & 0 & 0 \\ 0 & 0 & 0 & 0 \\ 0 & 0 & 0 & 0 \end{bmatrix} \tag{4.8}$$

and $\mathbf{o}$ transforms the resulting eight element Stokes vector into two measured intensities according to

$$\begin{bmatrix} \eta_{\perp} & 0 & 0 & 0 & 0 & 0 & 0 & 0 & \\ 0 & 0 & 0 & 0 & \eta_{\parallel} & 0 & 0 & 0 & \ldots \\ & & & & \vdots & & & & \end{bmatrix} \tag{4.9}$$

where $\eta_{\perp}$ and $\eta_{\parallel}$ are the efficiencies of the perpendicular and parallel detection channels, respectively.

Consolidating Equation (4.1) into relevant terms and assuming here for illustrative purposes that $\mathbf{M_{TX}}$ and $\mathbf{M_{RX}}$ are defined as identity matrices, the number of photoelectrons generated in each detection channel from the $\mathbf{N}$th surface is defined as

$$N_{\perp}^{N} = \mathbf{o}\mathbf{P}_{\perp}\mathbf{F}_{N}(\vec{k}_i, \vec{k}_s, R)\vec{S}_{TX} \tag{4.10}$$

and

$$N_{\parallel}^{N} = \mathbf{o}\mathbf{P}_{\parallel}\mathbf{F}_{N}(\vec{k}_i, \vec{k}_s, R)\vec{S}_{TX} \tag{4.11}$$

Therefore,

$$N_{\perp}^{N} = \begin{bmatrix} 1 & 0 & 0 & 0 \end{bmatrix} \begin{bmatrix} 1 & -1 & 0 & 0 \\ -1 & 1 & 0 & 0 \\ 0 & 0 & 0 & 0 \\ 0 & 0 & 0 & 0 \end{bmatrix} \beta_N \begin{bmatrix} 1 & 0 & 0 & 0 \\ 0 & a_N & 0 & 0 \\ 0 & 0 & b_N & 0 \\ 0 & 0 & 0 & c_N \end{bmatrix} \vec{S}_{TX} \tag{4.12}$$

and

$$N_{\parallel}^{N} = \begin{bmatrix} 1 & 0 & 0 & 0 \end{bmatrix} \begin{bmatrix} 1 & 1 & 0 & 0 \\ 1 & 1 & 0 & 0 \\ 0 & 0 & 0 & 0 \\ 0 & 0 & 0 & 0 \end{bmatrix} \beta_N \begin{bmatrix} 1 & 0 & 0 & 0 \\ 0 & a_N & 0 & 0 \\ 0 & 0 & b_N & 0 \\ 0 & 0 & 0 & c_N \end{bmatrix} \vec{S}_{TX} \tag{4.13}$$

Defining the transmitted polarization orientation as linear horizontal such that $\vec{S}_{TX} = \begin{bmatrix} 1 & 1 & 0 & 0 \end{bmatrix}^T$ permits the simplification

$$N_{\perp}^{N} = \beta_N \left(1 - a_N\right) \tag{4.14}$$

and

$$N_{\parallel}^{N} = \beta_N \left(1 + a_N\right) \tag{4.15}$$

To compute a, set

$$\beta_N = \beta_N \tag{4.16}$$

$$\frac{N_{\perp}^{N}}{1 - a_N} = \frac{N_{\parallel}^{N}}{1 + a_N} \tag{4.17}$$

$$a_N = \frac{N_{\parallel}^{N} - N_{\perp}^{N}}{N_{\perp}^{N} + N_{\parallel}^{N}} \tag{4.18}$$

Thus, in addition to enabling a measurement of range, the received scattered signals contain polarization information that can be evaluated to interrogate the scattering properties of a media surface. This information can be used to differentiate between and classify surfaces with varying $\mathbf{F}$, such as water and ice [118], by measuring the propensity of the surface to depolarize incident light and couple energy into the perpendicular polarization plane. Depolarization is often characterized

by ratioing the perpendicular and parallel polarization components of the received scattered light. For the lidar described here, the resulting linear depolarization ratio [51] is defined as

$$\delta = \frac{N_{\perp}}{N_{\parallel}} \tag{4.19}$$

where $N_{\perp}$ and $N_{\parallel}$ are the components of the detected signal polarized perpendicular and parallel to the transmitted beam, respectively. For polarization-maintaining surfaces such as smooth water, $\delta \approx 0$, while depolarizing surfaces such as ice tend to decouple the incident polarized laser light such that $\delta > 0$.

4.2.1 Simulation

The polarization lidar is simulated ranging to a single surface ($N = 1$) of an arbitrary semitransparent media. The transmitted signal is oriented linear horizontal with 0.95 DOP and resulting normalized Stokes vector defined as

$$\vec{S}_{TX} = \begin{bmatrix} 1 \\ 0.95 \\ 0 \\ 0 \end{bmatrix} \tag{4.20}$$

as illustrated in Figure (4.1). $\mathbf{M_{TX}}$ and $\mathbf{M_{RX}}$ are defined as identity matrices, and the Mueller matrices of the detection channels are defined in Equations (4.7) and (4.8). The media surface is defined according to Equation (3.12) with scattering matrix $\mathbf{F_1}$, surface reflectivity $\beta_1 = 1.0$, and $a_1 = 0.4$. The resulting normalized received intensities in each detection channel are defined according to Equations (4.10) and (4.11) as $N_{\perp}^1 = 0.31$ and $N_{\parallel}^1 = 0.69$, respectively, measured as the S_0 element of the Stokes vectors plotted in Figure (4.2). The transmitted DOP of $\vec{S}_{TX}$ and the scattering properties $\mathbf{F_1}$ of the media surface drive the measured intensities $N_{\perp}$ and $N_{\parallel}$, neglecting instrument effects along the optical path. Figure (4.3) illustrates the normalized received intensities in each detection channel for $a_1 = 0 : 1$ and transmitted signal $\vec{S}_{TX}$ with DOP equal to 0.95 and 0.5.

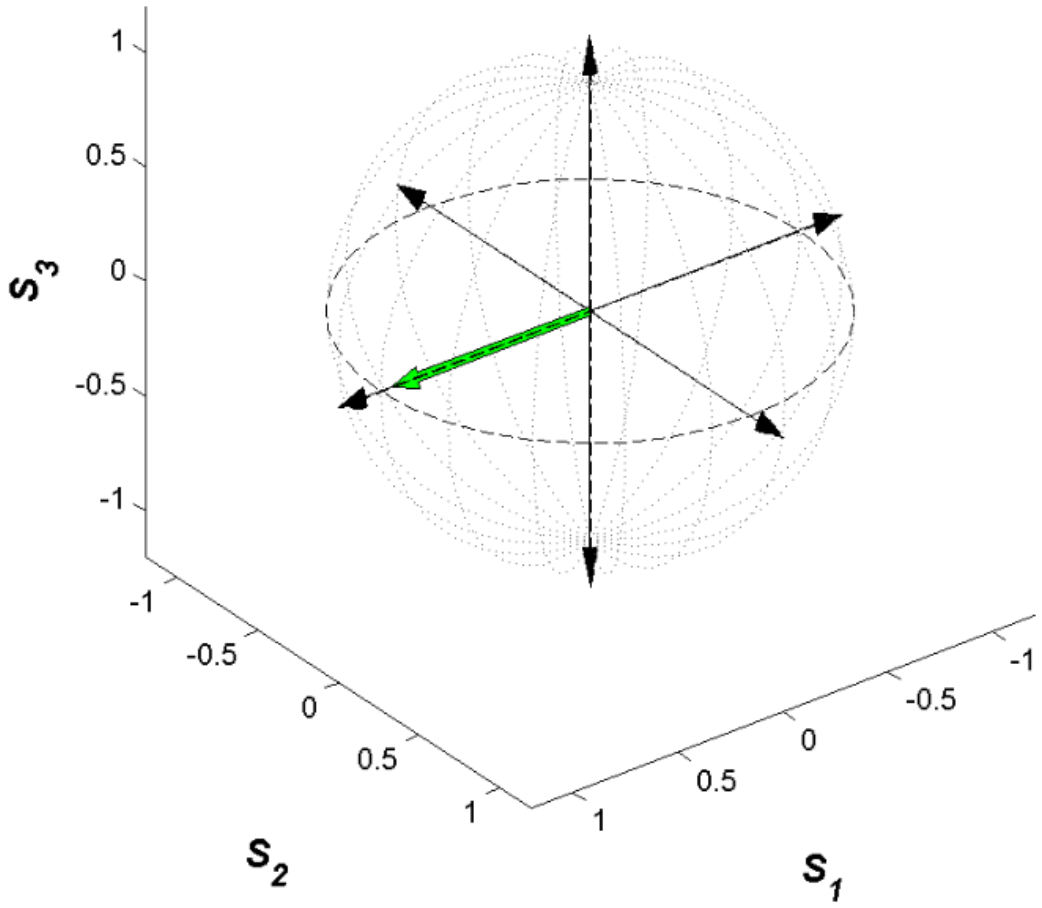

Figure 4.1: Transmitted Stokes vector $\vec{S}_{TX} = [1, 0.95, 0, 0]^T$ oriented linear horizontal with 0.95 degree of polarization.

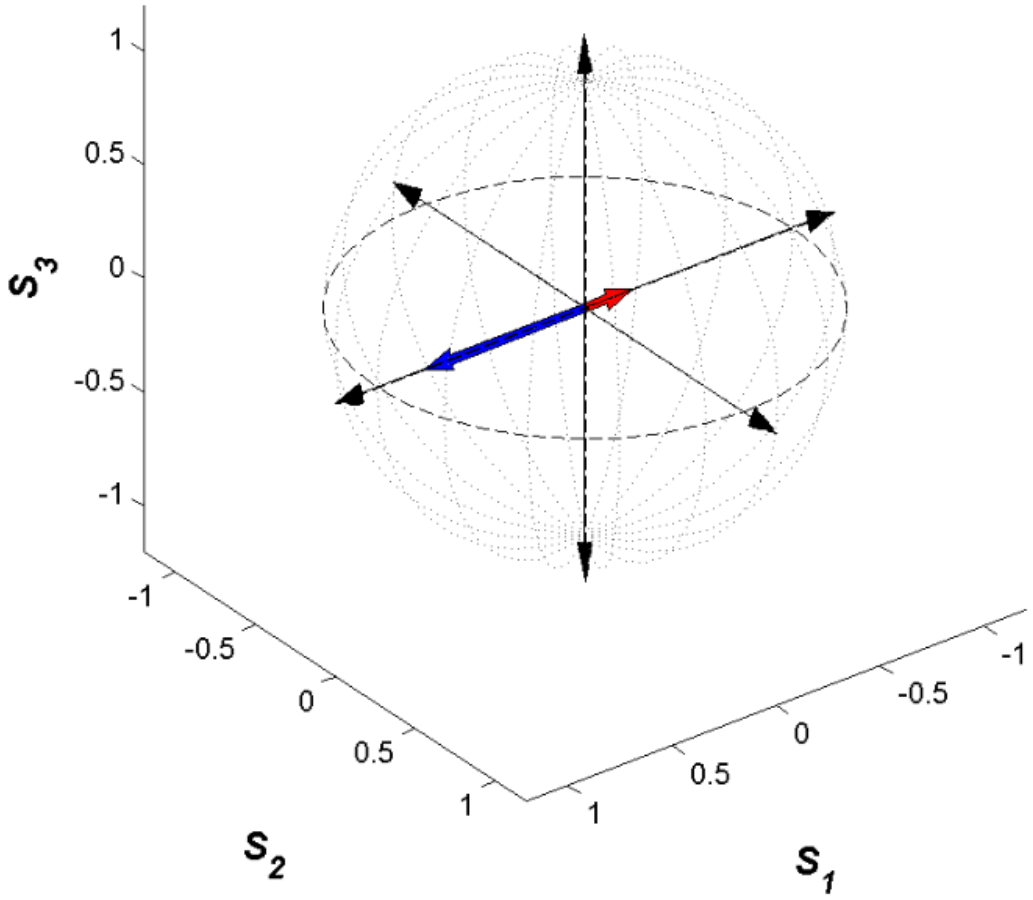

Figure 4.2: Received Stokes vectors for the simulated polarization lidar. The photodetector in each detection channel measures the S_0 (intensity) element of parallel (blue) and perpendicular (red) vectors.

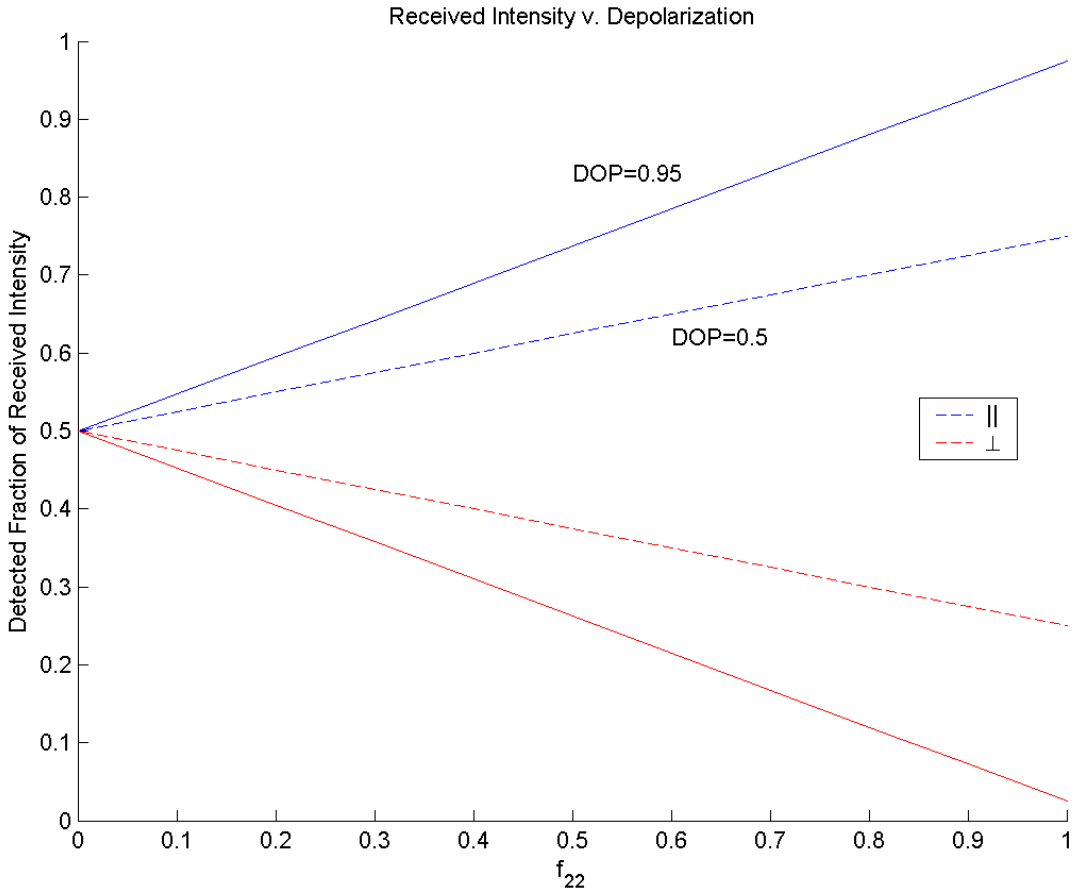

Figure 4.3: Normalized detected signal for varying surface a_1 (f_{22} element) and transmitted DOP.

The polarization lidar is now simulated for a sensor ranging to semitransparent media bounded by $N = 3$ surfaces. Referring to Figure (3.2), the thickness of each surface is defined as $\ll$ than the transmitted laser pulse width $c\tau$ and $n_0 = n_{1,2} = 1.00$ such that timing effects due to variable refractive indices are negligible. The transmitted Stokes vector $\vec{S}_{TX}$ with 0.95 DOP propagates through the $N = 3$ surfaces, each with scattering matrix $\mathbf{F_{1:3}}$ defined in Equation (3.12) for $\beta_1 = \beta_{2,3} = 1.0$ and $a_1 = 1.0$, $a_2 = 0.2$, $a_3 = 0.6$. Scattered signals are received by the sensor from the $N = 1$ surface at time $t_{F_1} = 0$, $N = 2$ surface at $t_{F_2} = 10$ nsec, and $N = 3$ surface at $t_{F_3} = 20$ nsec, such that the depth between each sequential surface is 1.5 m. From Equations (4.10) and (4.11), $N_{\perp}^{1,2,3} = 0.025, 0.405, 0.215$ and $N_{\parallel}^{1,2,3} = 0.975, 0.595, 0.785$, respectively. For illustrative purposes, the measured intensities in each detection channel have been assigned to the peak amplitude of the respective photodetector output voltage, defined as a photomultiplier tube with 1.0 nsec rise time and 2.5 nsec FWHM output pulse length.

The resulting photodetector outputs are plotted in Figure (4.4). Conventional lidar sensors ranging through semitransparent media with a polarization indiscriminate approach detect the total intensity contained in the perpendicular and parallel polarization planes (black dashed). The measurement enables only a range-resolved observation of each surface. Incorporating polarization discrimination into the lidar, the detected signals enable a range-resolved observation of each surface as well as an estimate of the capacity of each surface to depolarize the incident laser light. Depending on the definition of the scattering phase matrix $\mathbf{F}$ of the surface and the associated capacity of the surface to depolarize the incident laser light, the signals in the parallel (blue) and perpendicular (red) detection channels generate a variable photodetector intensity. Therefore, the range to each surface can be evaluated by the polarization lidar and the ratio of the detected signals can be used to discriminate between and classify surfaces of variable depolarization, at the expense of photodetector output level.

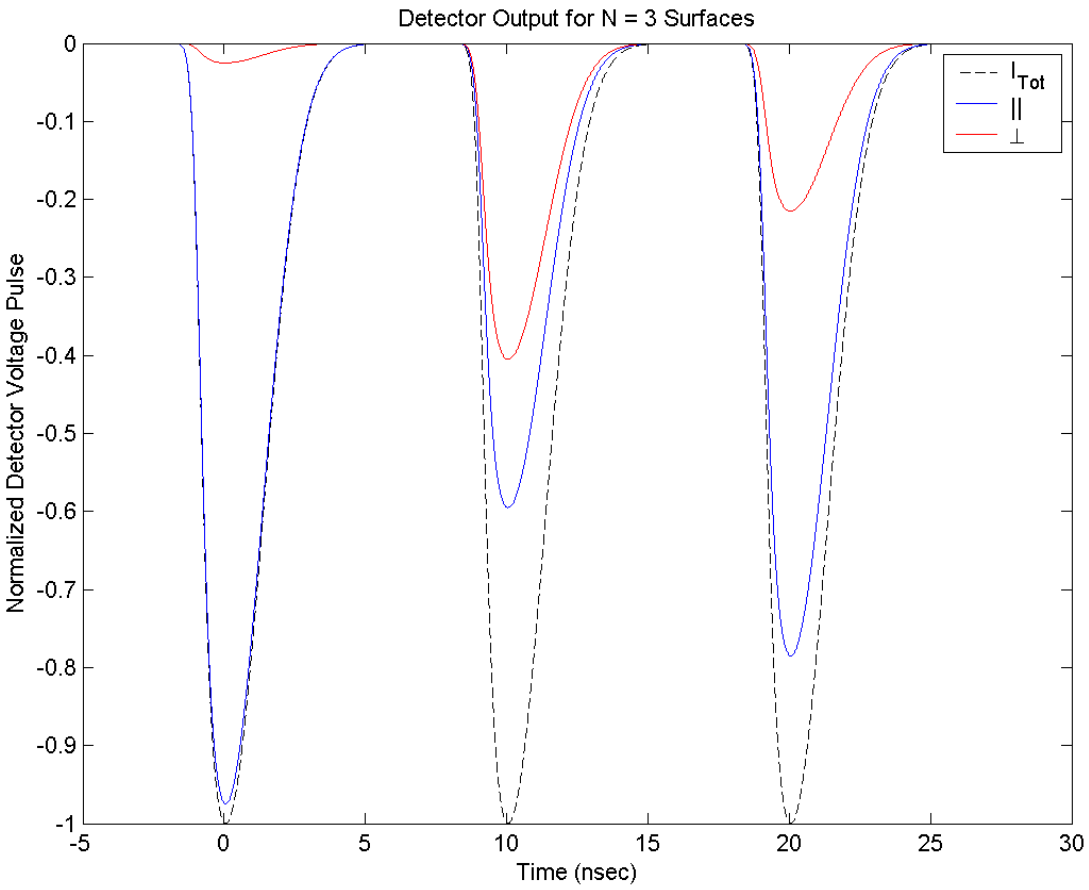

Figure 4.4: Simulated photodetector output for a polarization lidar ranging through semitransparent media bounded by $N = 3$ surfaces with varying depolarization scattering matrices defined by f_{22} elements $a_1 = 1.0$, $a_2 = 0.2$, $a_3 = 0.6$.

4.2.2 Optimization

The SVLE provides an end-to-end theoretically complete polarization description of range-resolved observations through semitransparent media bounded by N surfaces, giving full consideration to polarization effects of all components along the optical path and their impact on detection. This analysis tool is critical for understanding the systematic error and measurement attributes of the polarization lidar [66]. Optimization of the polarization lidar measurement is achieved through application of the SVLE in an effort to minimize systematic coupling of energy between the transmit and receive polarization planes.

The Stokes vector $\vec{S}_{TX}$ describing the transmitted polarization orientation must be chosen for maximum degree of linearity and DOP. Conventional lasers often transmit a Stokes vector $\vec{S}_{TX}$ with DOP < 1, requiring incorporation of polarization conditioning optics into the transmit path to increase the DOP of the laser light prior to transmission from the sensor. The Mueller matrices of the transmitter and receiver paths, $\mathbf{M_{TX}}$ and $\mathbf{M_{RX}}$, should avoid the use of reflective components which have the capacity to rotate and depolarize incident polarized light. Misalignment of the transmit and receive polarization planes must be properly aligned and calibrated for cross talk [5].

4.3 Range Operation

Following the polarization operation of the transmitted laser light along the optical path, the photoelectrons $\vec{N}^N$ generated by the sensor photodetector from the received signals scattered from the Nth surface are converted into an output voltage that is processed and stored by the sensor to provide the range observation [63]. Figure (4.5) provides a graphical overview of the signal processing schemes typically used by laser ranging sensors. The voltage output from the photodetector is composed of scattered laser light and noise sources consisting of detector dark counts and solar background. For sensors operating with an analog detection scheme, which include conventional lidar bathymetry sensors, high signal-to-noise ratio (SNR) performance per pulse is achieved through the use of laser pulses with high peak power to enable *monopulse* detection.

These sensors are designed to receive thousands of scattered photons per laser fire in order for the received scattered signals to exceed the expected noise floor with sufficient intensity to accurately resolve range.

In contrast to the analog approach, photon counting sensors utilize a low SNR approach to laser ranging [39, 63]. The approach is digital in nature, where there is either an absence or presence of discrete events upon detection of a photon (signal or noise). Unlike analog sensors, this low SNR, *micropulse* approach employs lasers with low peak power and aims to enable detection of single numbers of received photons. For low SNR laser ranging sensors, the photodetector is chosen with low characteristic dark noise as compared to the rate of received signal photons in an effort to minimize registration of noise events. For daytime operations, solar background is typically the dominant noise source, the effects of which can be reduced through incorporation of narrow fields of view and bandpass filtering.

4.3.1 Signal Acquisition

Conventional photodetectors used in laser ranging sensors are the avalanche photodiode (APD) and the photomultiplier tube (PMT). Regardless of the detection approach, operation of the photodetector is governed by the photoelectric effect [107, 108]. Semiclassical radiation theory predicts that the average rate of emission $\overline{r}$ of photoelectrons by the photoemitting surface of a photodetector which is irradiated with a constant intensity source of photons is described by

$$\overline{r} = \frac{\eta I A_d}{h\nu} \tag{4.21}$$

where η is the quantum efficiency of the photoemitting surface, $h\nu$ is the photon energy at laser frequency ν, I is the intensity of the incident optical radiation, and A_d is the surface area of the photoemitting surface. The quantum efficiency η is generally identified as the probability of photoelectron emission given incident energy $h\nu$. The average optical power $\overline{P}$ incident on the photoemitting surface during sensor operation is related to the average incident intensity by

$$\overline{P} = \overline{I} A_d \tag{4.22}$$

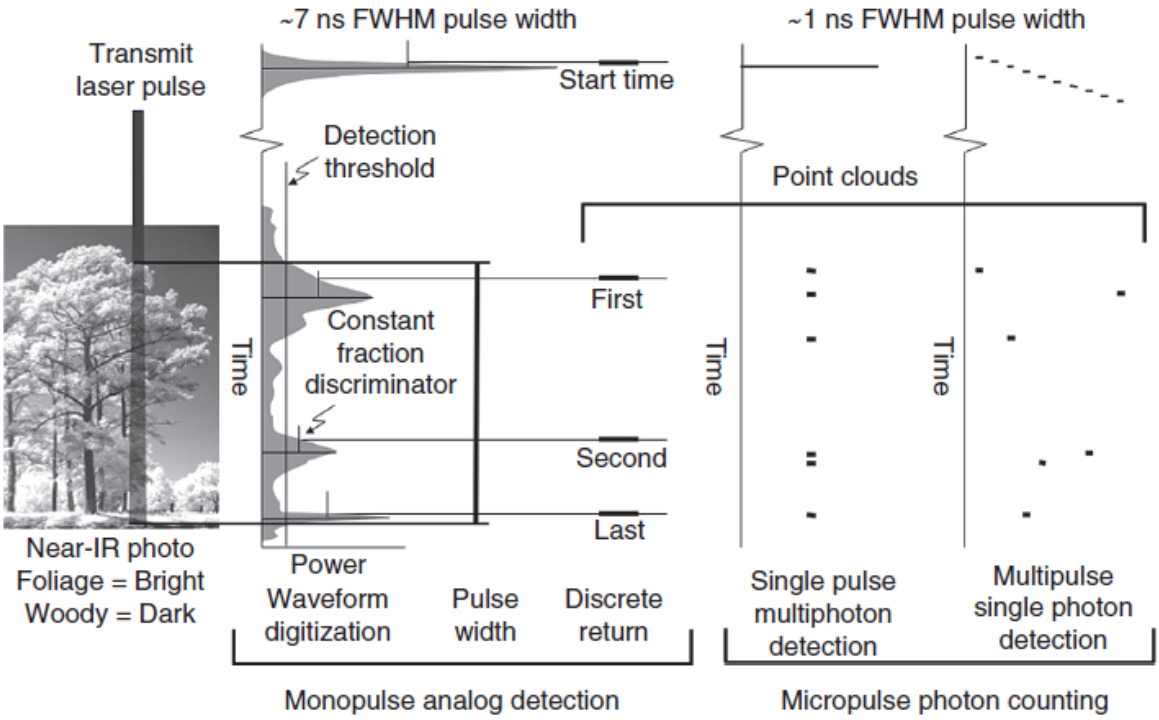

Figure 4.5: Illustration of the detection schemes commonly used in pulsed TOF laser ranging, shown here for the received signals scattered from a multi-storied forest canopy, taken from [63].

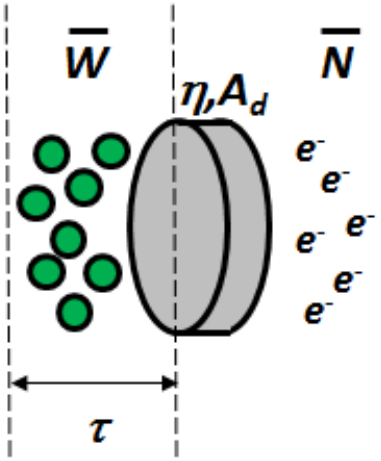

Figure 4.6: Depiction of the photoemitting element of a typical photodetector used for laser ranging. The element, defined with quantum efficiency η and active surface area A_d, is subject to an incoming average photon rate $\overline{W}$ prior to an average emission rate of $\overline{N}$ photoelectrons.

and the average optical energy (photons) $\overline{W}$ is related to the average power in the time interval τ by

$$\overline{W} = \overline{P}\tau \tag{4.23}$$

Therefore, the average number of photoelectrons emitted in the time interval τ can be defined according to

$$\overline{N} = \overline{r}\tau = \frac{\eta \overline{W}}{h\nu} \tag{4.24}$$

The probability of the detector surface emitting a photoelectron in the time interval $d\tau$ is $\overline{r}d\tau$, provided that $d\tau$ is small enough that the probability of two or more events occurring during $d\tau$ is negligible. The probability $P_k(\tau + d\tau)$ is then the sum of two mutually exclusive occurrences:

- k photoelectrons are emitted by time τ with probability $P_k(\tau)$ and no events occur during the interval $d\tau$, the latter probability being $(1 - \overline{r}\tau)$. Since these events are independent by assumption, their joint probability is $(1 - \overline{r}\tau)P_k(\tau)$.

- k - 1 photoelectrons are emitted in time τ with probability $P_{k-1}(\tau)$ and one emission occurs during the interval $d\tau$, the latter probability being $\overline{r}d\tau$. Once again, independence leads to a joint probability of $\overline{r}d\tau P_{k-1}(\tau)$.

Therefore,

$$P_k(\tau + d\tau) = (1 - \overline{r}d\tau)P_k(\tau) + \overline{r}d\tau P_{k-1}(\tau) \tag{4.25}$$

and

$$\frac{P_k(\tau + d\tau) - P_k(\tau)}{d\tau} = \overline{r}[P_{k-1}(\tau) - P_k(\tau)] \tag{4.26}$$

Taking the limit where $d\tau \to 0$,

$$\frac{P_k(\tau)}{d\tau} = \overline{r}[P_{k-1}(\tau) - P_k(\tau)] \tag{4.27}$$

Assuming that $k = 0$ photoelectrons are emitted in the interval $d\tau$ and $P_{-1}(\tau) = 0$, then

$$\frac{dP_0}{d\tau} = -\overline{r}P_0(\tau) \tag{4.28}$$

Integrating the boundary condition $P_0(0) = 1$ yields

$$P_0(\tau) = e^{-\overline{r}\tau} \tag{4.29}$$

For $k = 1$ emitted photoelectrons in the time interval $d\tau$,

$$\frac{dP_1}{d\tau} = \overline{r}[P_0(\tau) - P_1(\tau)] = \overline{r}[e^{-\overline{r}\tau} - P_1(\tau)] \tag{4.30}$$

and with the boundary condition $P_1(0) = 0$ yields

$$P_1(\tau) = \overline{r}\tau e^{-\overline{r}\tau} \tag{4.31}$$

Therefore, it can be concluded by induction that for k emissions

$$P_k(\tau) = \frac{(\overline{r}\tau)^k}{k!}e^{-\overline{r}\tau} \tag{4.32}$$

Incorporating the average number of photoelectrons $\overline{N}$ emitted in time τ as defined in Equation (4.24), the discrete probability density function is defined according to a Poisson distribution for the distribution of k photoelectrons,

$$q(k; \overline{N}) = \frac{(\overline{N})^k}{k!}e^{-\overline{N}} \tag{4.33}$$

and plotted in Figure (4.7) for variable values of k and $\overline{N}$.

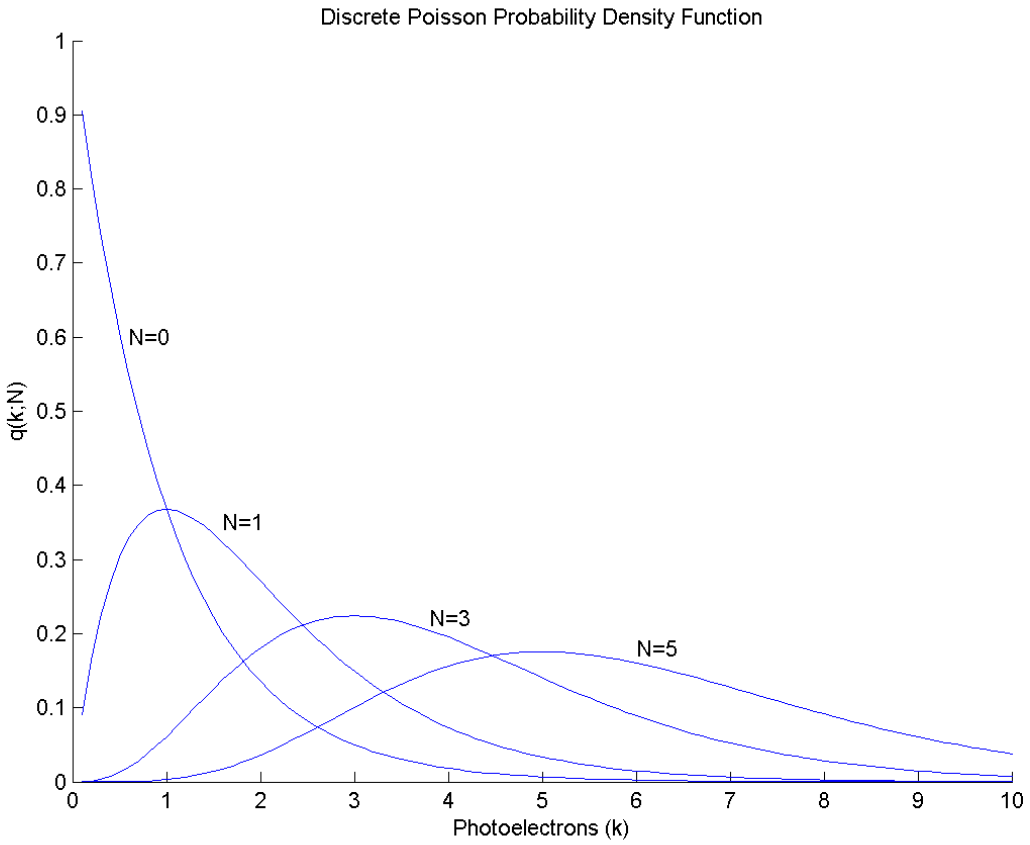

Figure 4.7: The discrete Poisson probability density function described by Equation (4.33) for variable average photoelectron count $\overline{N}$ and emitted photoelectrons k.

From Equation (4.33), the probability of the photodetector surface emitting a photoelectron and generating an output voltage that can be processed to provide a range observation requires $k > 0$ emitted photoelectrons such that

$$P_{k>0} = 1 - q(0; \overline{N}) = 1 - e^{-\overline{N}} \tag{4.34}$$

Therefore, for the low SNR lidar sensor to achieve a minimum 95% detection probability for each transmitted laser pulse requires a minimum average emission rate of $\overline{N} = 3$ photoelectrons, as depicted in Figure (4.8).

4.3.2 Implications for Sensor Architecture

Conventional lidar bathymetry sensors transmit modest laser pulse energies (mJ) and use high detection thresholds to resolve unambiguous range measurement of scattered signals with few false alarms in the presence of noise from detector dark counts and background solar illumination [57, 63]. These sensors are designed to receive thousands of scattered photons for each transmitted laser pulse in order to exceed the detector noise floor and enable monopulse observation of range. Due to the demand for high peak power, conventional sensors use lasers with broad pulse widths on the order of several nsec, restricting operation to low repetition rates on the order of hundreds of Hz [53, 72] and limiting performance in the shallow media regime due to the ambiguity between overlapping surface and bottom scattered signals. Ironically, this degradation of performance in the shallow regime has historically been largely accepted by the lidar bathymetry community. Guenther [54] notes that "relatively narrow pulse widths are needed to provide required timing accuracy and resolution of shallow depths; a pulse width of under 7 nsec is desirable," the spatial equivalent of 1.5 m in water. This conventional approach limits the density of range-resolved observations acquired by ALB sensors along the flight path, ultimately degrading estimation of the volume of water.

The conventional high SNR detection approach favors a simplified detection scheme, where the use of lasers with modest pulse energies is prioritized over other SWaP aspects of the system. This trade limits operation of these sensors onboard platforms where mass, volume, and power are

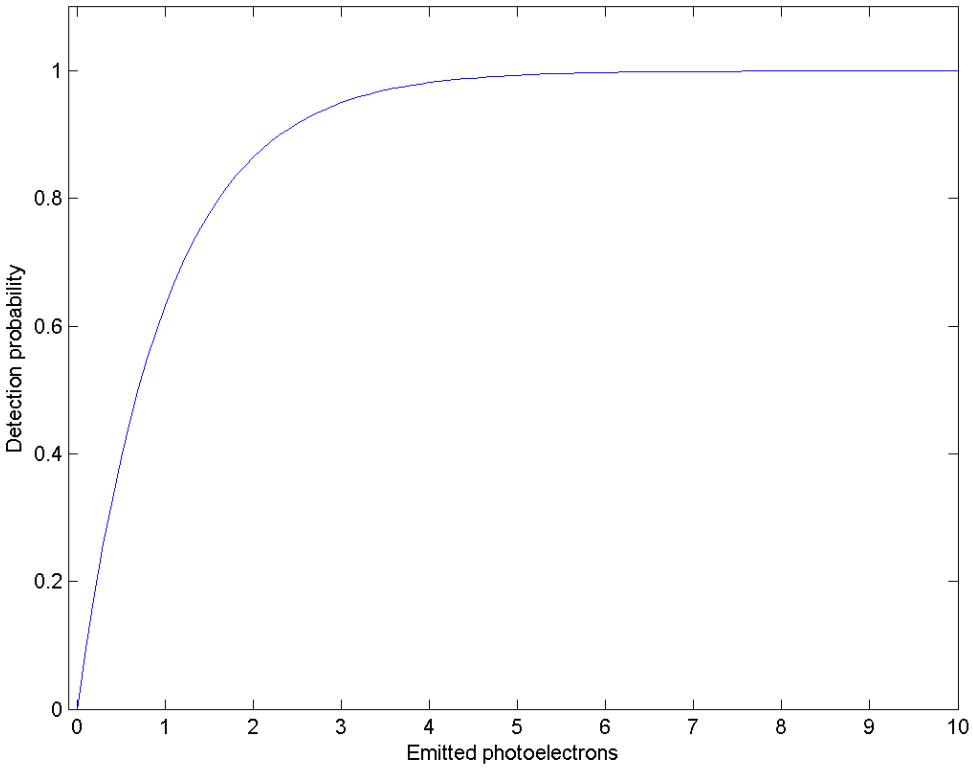

Figure 4.8: Probability of the photodetector emitting a minimum of 1 photoelectron as a function of the average emission rate $\overline{N}$ [33, 39].

limited, such as UAS. Discussing the future of ALB sensors, Gutelius [61] explains that two key drivers of future growth include a reduction in system capital cost, driven primarily by a reduction in technological complexity of ALB sensors, in conjunction with lower system operational costs, driven by increasing the availability of aircraft of opportunity, lowering the cost and size of the lidar sensor, and reducing manpower requirements. *"Clearly the next platforms for ALB systems will be unmanned aircraft systems/air vehicles (UAS/UAV). To make a step-wise change in size, weight, and power demands to fit in an ALB package on a UAV (at the same time retaining performance) requires substantial advances in several areas of engineering. The key challenge...to developing a substantially down-sized system is in somehow maintaining current ALB performance."*

> ***"Clearly the next platforms for ALB systems will be unmanned aircraft... The key challenge...to developing a substantially down-sized system is in somehow maintaining current ALB performance."***
> **Bill Gutelius**, President, Active Imaging Systems

Figures (4.7) and (4.8) illustrate theoretically that the conventional high SNR approach to lidar bathymetry does not efficiently use available laser photons. In the field of topographic laser ranging, Degnan [40, 39] has demonstrated that for a given laser power-receive aperture product, the maximum return rate of signals scattered from the target media is obtained by adopting a single photon sensitivity in the sensor detection architecture. While the detection threshold can be adjusted to optimize the SNR based on the operational environment of the sensor, this suggests efficiency of the range-resolved observation is maximized when using a high repetition rate, low energy laser transmitter.

Development of low peak power (μJ), high repetition rate (kHz) lasers and multi-event, single photon sensitive detection channels have enabled a low SNR detection approach to range-resolved observations. Building upon the work of [34, 40, 39, 122], the depth sounding rate of a lidar bathymetry sensor can be increased for a given laser output power by transmitting the available photons in a high frequency (kHz) train of low energy pulses and employing a low SNR

detection approach. The low peak power, high average power architecture permits a reduction in the transmitted pulse energy, and subsequently the pulse width, reducing the severity of pulse overlap limitations in the shallow media regime. The components required for a low SNR sensor translate into low SWaP requirements, creating the potential for incorporation onboard platforms such as UAS. Significant scientific interest exists in the potential to increase the density of depth soundings, particularly in the study of rapidly developing water bodies such as dynamic supraglacial melt lakes. Thus, in an effort to develop an efficient sensor for future use onboard platforms such as UAS, the polarization lidar developed in the dissertation research employs a low SNR approach to range-resolved observation through semitransparent media.

4.3.3 Signal to Noise Considerations

The multi-event, low SNR approach to laser ranging is not without its drawbacks. Inevitably, low SNR sensors are prone to false alarms in the presence of solar background and detector dark noise. However, the severity of the limitation can be reduced through proper system design, including incorporation of narrowband interference filters and narrow fields of view in parallel with proper discriminator threshold configuration. Additionally, following each recorded event, the sensor suffers a "dead time" in which subsequent scattered optical signals received by the sensor cannot be registered by the detection electronics [124]. While the characteristic dead time varies based on sensor configuration, the restriction on sensor operation can be significant. For example, the prototype sensor developed within this dissertation suffers from a 270 nsec dead time. Upon discrimination and recording of the photodetector output (initiated by signal or noise), the sensor is unable to record another event for 270 nsec, equivalent to 40.5 m of range in air or 30.5 m of water depth. Proper performance of a low SNR lidar sensor demands attention to proper design and optimization of detection electronics for the desired operational environment.

In addition to the signals scattered from the bounding media surfaces, there are several noise contributions to the photodetection statistics. Consider first those noise sources that are Poisson distributed, namely detector dark noise and solar background scattered along the optical path.

Let $\overline{N}_s$ and $\overline{N}_n$ be the count variables representing the mean signal and noise photoelectrons, respectively, in each detection channel such that $\overline{N}_{s+n} = \overline{N}_s + \overline{N}_n$ describes the mean signal plus noise photoelectron count due to photons arriving during the measurement interval τ. The discrete probability density function is again defined according to a Poisson distribution such that

$$q_{s+n}(k; \overline{N}_{s+n}) = \frac{(\overline{N}_s + \overline{N}_n)^k}{k!} e^{(-\overline{N}_s + \overline{N}_n)} \tag{4.35}$$

The detection threshold photoelectron count k_{th} is given by the largest integer satisfying the inequality describing the probability of false alarm probability

$$P_{fa} \geq \sum_{k=k_{th}}^{\infty} \frac{(\overline{N}_n)^k}{k!} e^{-\overline{N}_n} = 1 - \sum_{k=0}^{k_{th}-1} \frac{(\overline{N}_n)^k}{k!} e^{-\overline{N}_n} \tag{4.36}$$

resulting in a probability of detection defined for k_{th} according to

$$P_d = \sum_{k=k_{th}}^{\infty} q_{s+n}(k; \overline{N}_{s+n}) = 1 - \sum_{k=0}^{k_{th}-1} q_{s+n}(k; \overline{N}_{s+n}) \tag{4.37}$$

and corresponding signal to noise ratio of the range observation

$$SNR = \frac{\langle k \rangle}{\sqrt{var(k)}} = \frac{\overline{N}_s}{\sqrt{\overline{N}_s + \overline{N}_n}} = \frac{\overline{N}_s}{\sqrt{\overline{N}_s + \overline{N}_n}} \tag{4.38}$$

Equations (4.36) - (4.38) illustrate detection statistics of the low SNR approach, in which the probability of false alarm is generally large compared to conventional high SNR sensors, particularly in the presence of solar background. However, range resolved observations are enabled through proper discriminator thresholding and the use of high repetition rate lasers. Integration of multiple pulses effectively reduces the probability of false alarm. Here, the sensor integrates detected events from a train of n pulses under the assumption of a constant false alarm rate during the integration interval. Since the signal improves linearly with the number of integrated pulses n and the noise increases by $\sqrt{n}$, an overall improvement in SNR of $\sqrt{n}$ is achieved.

$$SNR^{(n)} = \frac{\langle k \rangle}{\sqrt{var(k)}} = \frac{n\overline{N}_s}{\sqrt{n(\overline{N}_s + \overline{N}_n)}} = \frac{\sqrt{n}\overline{N}_s}{\sqrt{\overline{N}_s + \overline{N}_n}} \tag{4.39}$$

Consider a train of constant amplitude pulses received from the first surface of a semitransparent media. Each pulse corresponds to the case of a Poisson signal immersed in a Poisson background

described by Equation (4.35). The discrete probability density function for the integrated pulse train is described according to

$$q_{s+n}^{(n)}(k;\overline{N}_{s+n}) = \frac{n^k(\overline{N}_s + \overline{N}_n)^k}{k!}e^{-n(\overline{N}_s+\overline{N}_n)} \tag{4.40}$$

The detection statistics are calculated in the same manner as the single pulse ($n = 1$) case, such that

$$P_{fa}^{(n)} \geq 1 - \sum_{k=0}^{k_{th}-1} \frac{(n\overline{N}_n)^k}{k!}e^{-n\overline{N}_n} \tag{4.41}$$

$$P_d^{(n)} = 1 - \sum_{k=0}^{k_{th}-1} q_{s+n}^{(n)}(k;\overline{N}_{s+n}) \tag{4.42}$$

Integration of n pulses by low SNR laser ranging sensors is typically performed in post-processing of acquired timing data through discrimination of temporal coherence [39, 89].

4.3.4 Detection Threshold and Timing Data Considerations

4.3.4.1 Threshold Configuration

Desired SNR performance of the sensor is characterized based on the operational environment of range observation. A diagram of the signal and noise environment for a lidar bathymetry sensor is depicted in Figure (4.9), modified from Figure (2.3) to show only the transmitted and scattered pulses from the first and second surface defined by the scattering matrices $\mathbf{F_1}$ and $\mathbf{F_2}$. For the purposes of illustration, the sensor is simulated ranging through a target water body such that the first surface defines the scattering properties of the air/water interface and the second surface defines the scattering properties of the bottom. The sensor is assumed here to operate at a nominal flight altitude of 300 m above the water surface, typical of low flying UAS, with a maximum expected media depth of 10 m. The range resolution of the sensor is defined by the $\tau_{bin} = 27$ psec bin resolution of the timing electronics used in the dissertation research such that

$$\Delta R = \frac{c\tau}{2n} = \frac{c(27e^{-12})}{2n_{0,1}} \tag{4.43}$$

and ΔR equals 4 mm in air, 3 mm in water. Photoelectron events generating an output voltage from the photodetector are recorded by the timing electronics throughout the range window. A 95% detection probability with a maximum false alarm probability of 1% during the range measurement (for each laser fire) in each detection channel is desired.

As depicted in Figure (4.9), the total average number of noise photoelectrons includes:

- Dark noise generated by each detection channel of the sensor, including spontaneous emission of photoelectrons by the photodetector and noise contributions from discriminating and recording electronics, $\overline{N}_{b,dark}$. For the polarization lidar developed in the dissertation, the photodetector in each detection channel operates with a dark noise rate of $\overline{N}_{b,dark} = 50$ photoelectrons/sec, as specified by the manufacturer in Figure (4.10) and verified through measurement.

- Noise due to solar background illumination isotropically scattered through the atmosphere and into the sensor receiver path, $\overline{N}_{b,atm}$. Degnan [39] defines the atmospheric contribution to the solar background as

$$\overline{N}_{b,atm} = \frac{\eta_q \eta_r}{h\nu} \frac{N_\lambda^0(\Delta\lambda) A_r \Omega_r}{4\pi} \left[\frac{1 - T_0^{1+sec\theta_s}}{1 + sec\theta_s} \right] \tag{4.44}$$

  where η_q is the photodetector quantum efficiency, η_r is the efficiency of the sensor receiver, N_λ^0 is the wavelength-dependent solar spectral illuminance of the atmosphere, $\Delta\lambda$ is the bandpass of the spectral filter in the receiver path, Ω_r is the receiver field of view in steradians, T_0 defines transmission through the atmosphere, and θ_s is the solar zenith angle at the time of the measurement.

- Noise due to solar background scattered from within the water volume, $\overline{N}_{b,water}$

- Noise due to the Lambertian scatter of solar background illumination from the surfaces defined by $\mathbf{F_1}$ and $\mathbf{F_2}$, $\overline{N}_{b,1}$ and $\overline{N}_{b,2}$, respectively defined by Degnan [39] such that

$$\overline{N}_{b,1:2} = \beta A_r \tau_{bin} = N_\lambda^0(\Delta\lambda)\Omega_r \tau_{bin} \left[\frac{\eta_q \eta_r A_r}{\pi h\nu} \right] \left[\rho T_0^{1+sec\theta_s} cos\phi + \frac{1 - T_0^{1+sec\theta_s}}{4(1 + sec\theta_s)} \right] \tag{4.45}$$

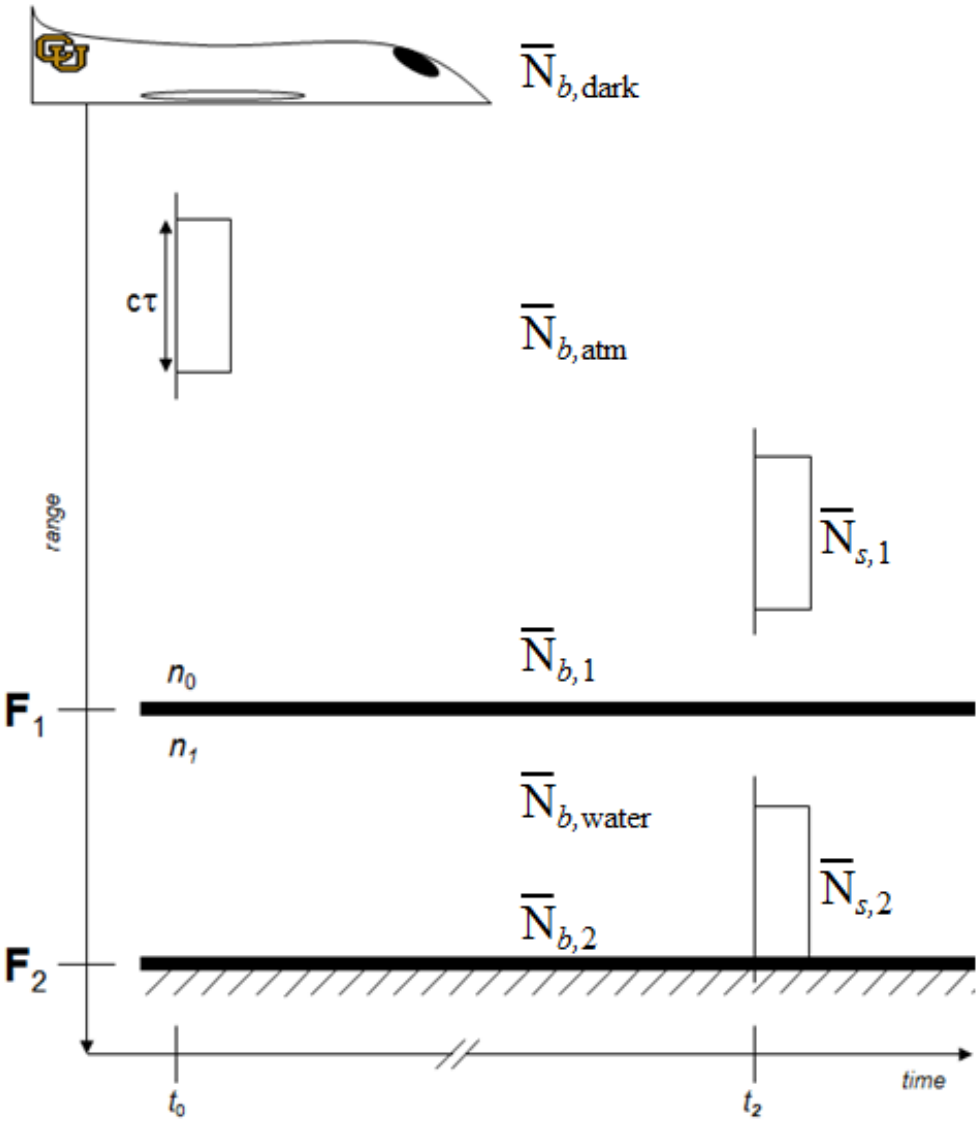

Figure 4.9: Diagram of the expected noise and signal sources during flight, modified from Figure (2.3). A pulse of laser energy of length $c\tau$ is emitted from the sensor at time t_0 in the presence of multiple noise sources. Signals are scattered from the first and second surface by time t_2 and transit back to the sensor.

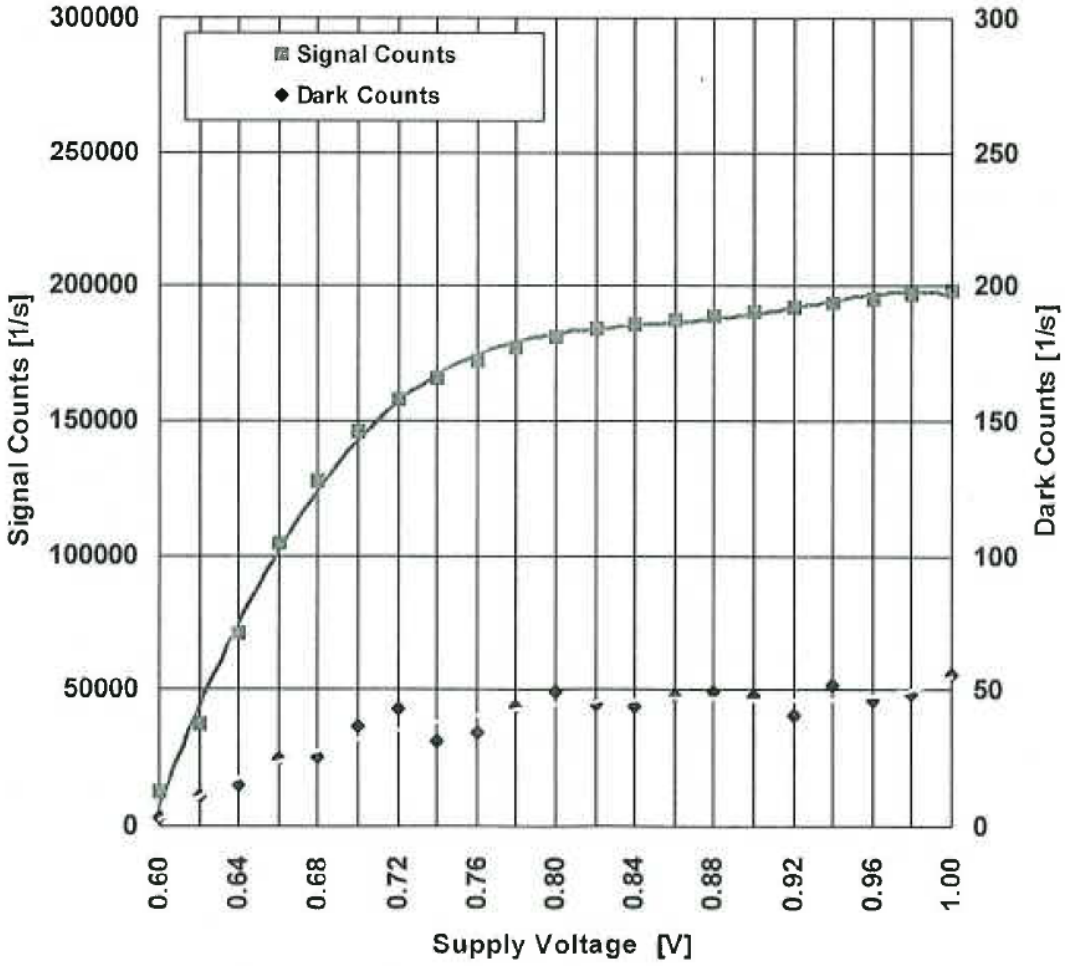

Figure 4.10: Detector dark noise rates as provided by the photodetector manufacturer. The photodetector is typically operated with a supply voltage of 0.80 V, generating an average dark noise rate of $\overline{N}_{b,dark} = 50$ photoelectrons/sec.

where ϕ is the subtended angle between the Sun and the surface normal.

The total mean number of noise photoelectrons per range bin is therefore defined according to

$$\overline{N}_b = (\overline{N}_{b,dark} + \overline{N}_{b,atm} + \overline{N}_{b,1} + \overline{N}_{b,water} + \overline{N}_{b,2})\tau_{bin} \tag{4.46}$$

The total average noise photoelectrons per range bin is calculated to be $\overline{N}_b = 1.2$ for the simulated sensor. Additionally, the Stokes vectors describing the solar background input to the sensor receiver from the atmosphere, water, and surfaces are defined according to Equation (3.15), assumed here to have zero DOP such that each detection channel in the sensor is subject to equal noise photoelectrons.

Range to the surface defined by the scattering matrix $\mathbf{F_1}$ (water surface) is evaluated initially. The sensor begins to record photoelectron events upon each laser fire. A flight altitude of 300 m above the water surface requires a minimum range window of 600 m in which the sensor records each event, signal or noise. For a 600 m detection window and 4 mm range resolution ΔR, the probability of false alarm within a single range bin is

$$0.01 * \frac{1}{(\frac{600m}{0.004m})} = 6.67e^{-8} \tag{4.47}$$

The threshold photon number k_{th} that results in a probability of exceeding the threshold

$$P(\overline{N}_{s,1+b} \geq k_{th}) \tag{4.48}$$

that is less than or equal to $6.67e^{-8}$ for the average noise rate of $\overline{N}_b = 1.2$ photoelectrons is evaluated in Equation (4.36) with the result $k_{th} = 10$. The number of signal plus noise photoelectrons required to produce a 95% detection probability for the threshold $k_{th} = 10$ is determined through Equation (4.37) with $\overline{N}_{s,1+b} = 15.8$ photoelectrons. Therefore, the required number of signal photoelectrons is $\overline{N}_{s,1} = \overline{N}_{s,1+b} - \overline{N}_b = 15.8 - 1.2 = 14.6$.

The simulation continues by examining range to the surface defined by the scattering matrix $\mathbf{F_2}$ (bottom). A flight altitude of 300 m and expected water depth of 10 m requires a minimum window of 628 m to account for the refractive index change of water, in which the sensor records

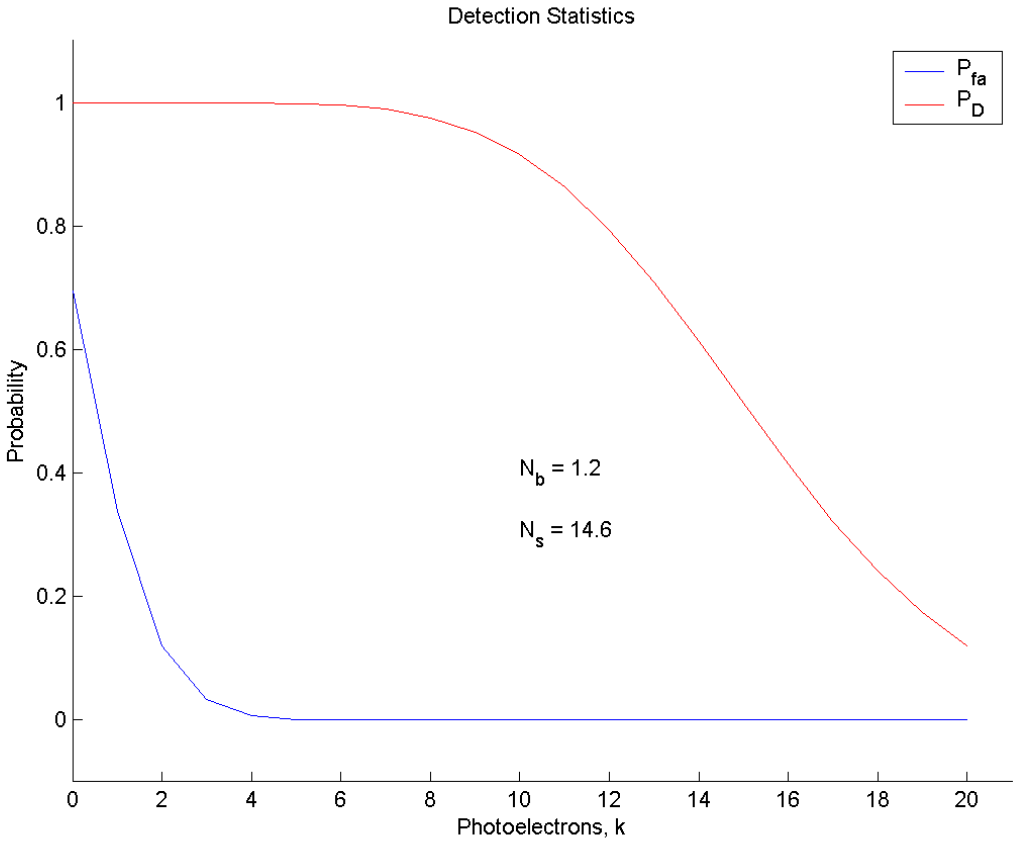

Figure 4.11: False alarm and detection probabilities for the range measurement of the first surface with the sensor detection threshold configured to $k_{th} = 10$.

each event. For a 628 m detection window and 4 mm range resolution, the probability of false alarm within a single range bin is

$$0.01 * \frac{1}{(\frac{628m}{0.004m})} = 6.37e^{-8} \tag{4.49}$$

The threshold photon number k_{th} that results in a probability of exceeding the threshold

$$P(\overline{N}_{s,2+b} \geq k_{th}) \tag{4.50}$$

that is less than or equal to $6.37e^{-8}$ for the average noise rate of $\overline{N}_b = 1.2$ photoelectrons is determined using Equation (4.36) and is again $k_{th} = 10$. The number of signal plus noise photoelectrons required to produce a 95% detection probability for the threshold $k_{th} = 10$ is determined through Equation (4.37) with $\overline{N}_{s,2+b} = 15.8$ photoelectrons. Therefore, the required number of signal photoelectrons is again $\overline{N}_{s,2} = 14.6$. The corresponding SNR of the range observation is

$$SNR = \frac{\overline{N}_s}{\sqrt{\overline{N}_s + \overline{N}_b}} = \frac{14.6}{\sqrt{14.6 + 1.2}} = 3.7 \tag{4.51}$$

4.3.4.2 Timing Data

Figure (4.12) illustrates timing data acquired with the simulated sensor from a calm, flat water surface and bottom in the parallel detection channel for a 6 cm water depth, defined as 20 range bins (540 psec). Dead time effects are neglected, enabling received signals scattered from the water surface and bottom to be discriminated and recorded by the timing electronics. The transmitted laser and photodetector pulse widths are assumed here to be less than a bin width and operate with no timing jitter, resulting in a single-bin registration of surface and bottom scattered signals. The detection threshold is configured such that $k_{th} \gg 10$ and no noise events are registered by the detection electronics during the measurement interval defined as 200 laser firings. As a result, signals scattered from the water surface and bottom are recorded and plotted in Figure (4.12).

The detrimental impact of the dead time associated with the timing electronics of low SNR lidar sensors is highlighted in Figure (4.13). Here, the detection threshold remains configured to

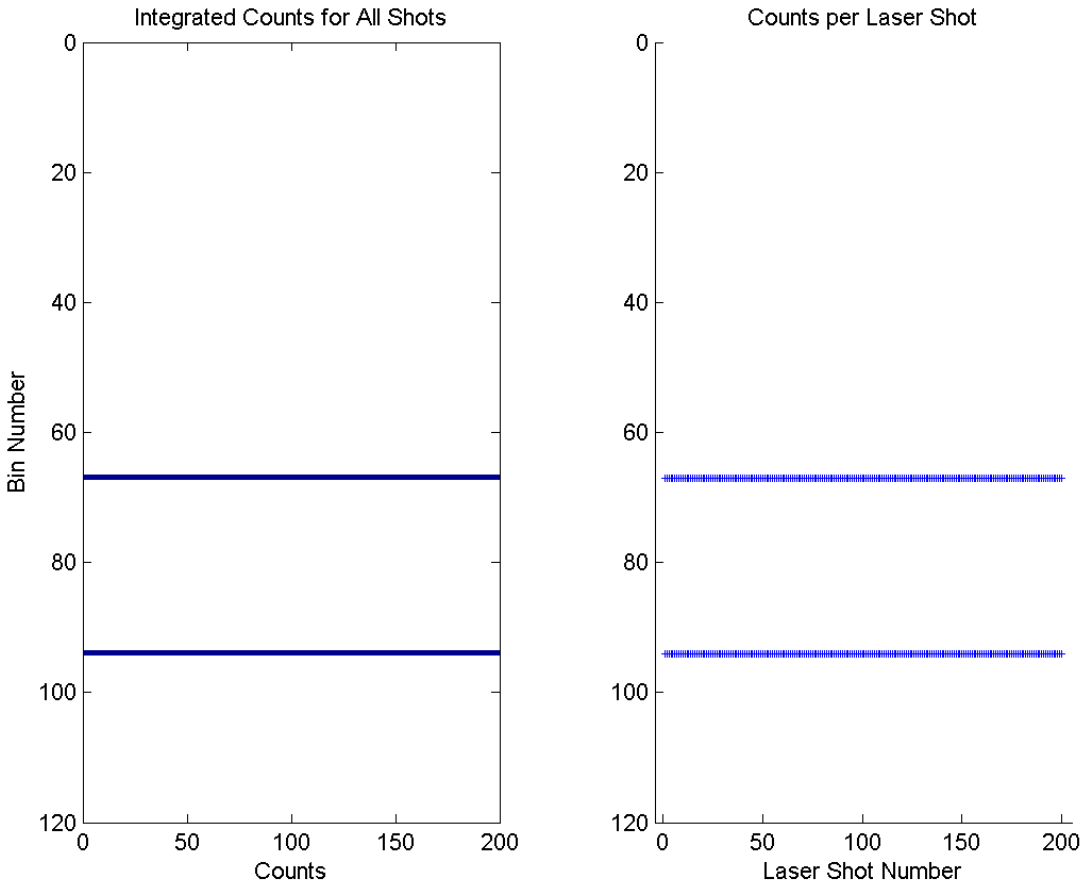

Figure 4.12: Simulated timing data for a flat water surface and bottom bounding 6 cm of water. The data is simulated in the detection channel receiving signals scattered in the polarization plane parallel to the transmitted laser light and photodetector with no pulse jitter. The detection threshold $k_{th} \gg 10$ such that no noise events are registered by the detection electronics. The detection channel is assumed to operate with no dead time such that received signals scattered from the water surface and bottom are recorded by the timing electronics.

$k_{th} \gg 10$ such that no noise events are registered by the detection electronics. However, a dead time corresponding to 30 bins (810 psec) has been applied to the detection electronics, preventing the sensor from registering signals scattered from the bottom.

The detection threshold k_{th} is lowered in Figure (4.14) such that $k_{th} \ll 10$ to increase the probability of false alarm such that the detection electronics register noise events. Following registration of a noise event, the detection electronics suffer a 30 bin dead time. However, registration of the incoherent noise events introduces a randomly-occurring dead time, statistically enabling registration of signals scattered from the surface and bottom. For a low SNR lidar bathymetry sensor, the registration of noise events provides a means to overcome the governing dead time of the electronics, at the expense of increased integration time and corresponding degradation of spatial resolution.

4.3.5 Discussion

This section of the dissertation highlights key performance aspects of the low SNR detection approach. If a rough estimate of the range between the sensor and media is known *a prior*, the range window can be reduced, leading to a reduction in the mean noise photoelectrons $\overline{N}_b$ passed through the detection path as well as the photon threshold k_{th} required to achieve the desired probability of false alarm per range bin. This so-called "range gate" approach has been successfully demonstrated [40, 39]. In the presence of polarized background sources, performance of the sensor can be optimized by transmitting/receiving in the plane parallel/perpendicular to the transmitted linearly polarized laser light to reduce the average noise rates in a preferential detection channel. The probability of false alarm can be reduced to limit the detection of noise photoelectrons, but at the cost of increased photoelectron detection threshold and the demand for increased signal levels $\overline{N}_{s,1}$ and $\overline{N}_{s,2}$.

As indicated, following discrimination of emitted photoelectrons (signal or noise) and recording of an event, the detection electronics used in low SNR laser ranging sensors are typically subject to a dead time in which additional signals cannot be recorded. The sensor developed in this dis-

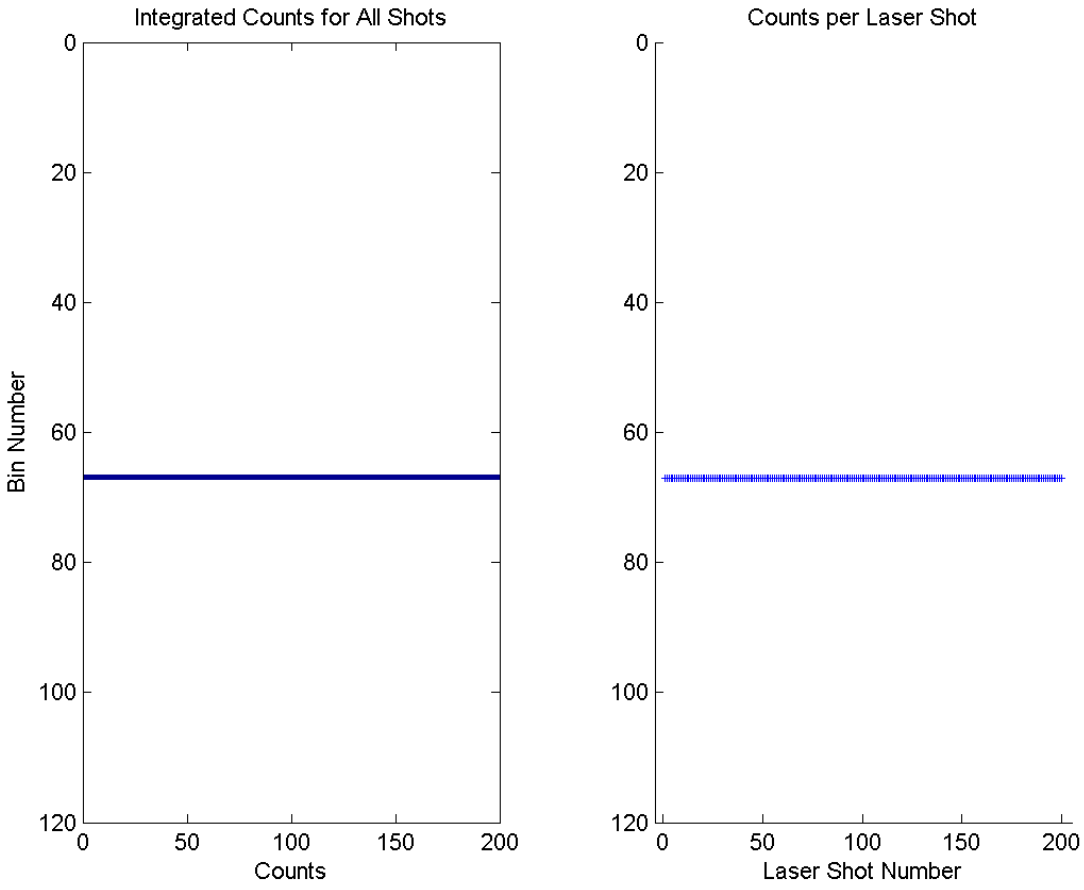

Figure 4.13: Simulated timing data for a flat water surface and bottom bounding 6 cm of water. The data is simulated in the detection channel receiving signals scattered in the polarization plane parallel to the transmitted laser light and photodetector with no pulse jitter. The detection threshold $k_{th} \gg 10$ such that no noise events are registered by the detection electronics, however a dead time corresponding to 30 bins has been incorporated into the measurement, preventing the sensor from registering signals scattered from the bottom.

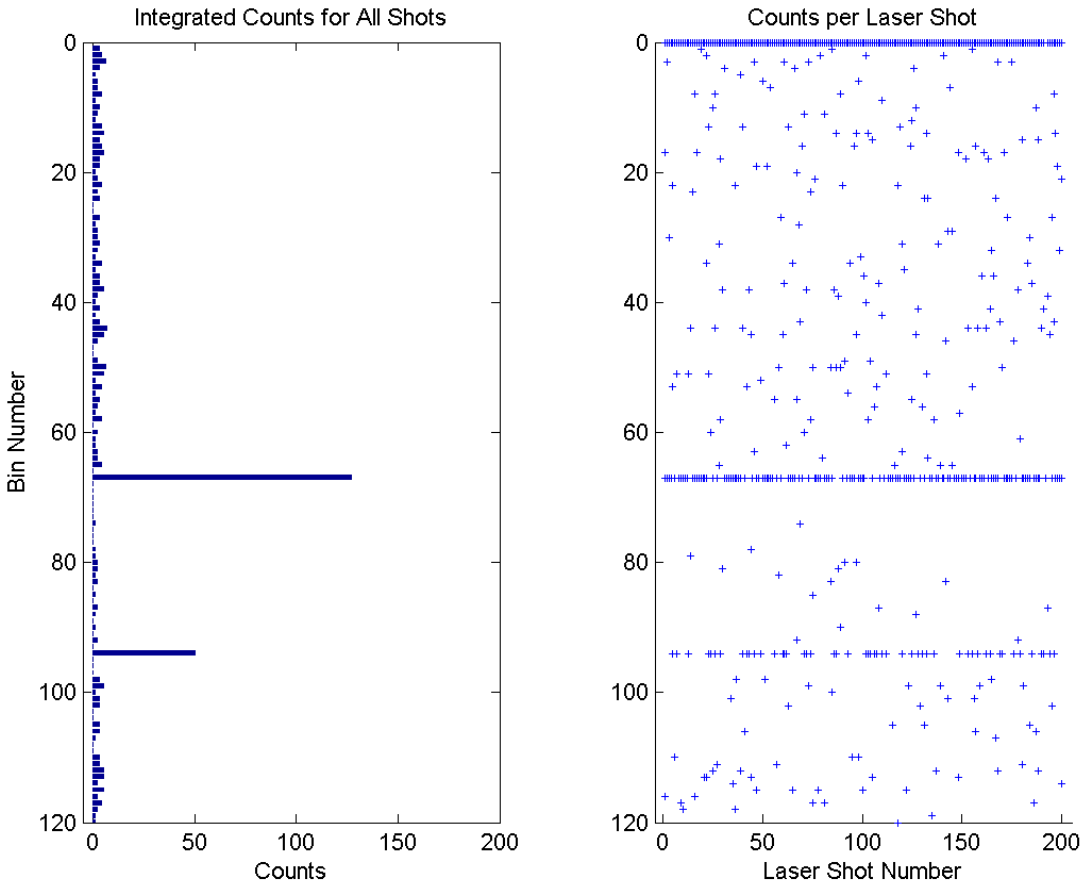

Figure 4.14: Simulated timing data for a flat water surface and bottom bounding 6 cm of water. The data is simulated in the detection channel receiving signals scattered in the polarization plane parallel to the transmitted laser light and photodetector with no pulse jitter. The detection threshold k_{th} has been lowered to $k_{th} \ll 10$ to increase the P_{fa} such that the detection electronics register noise events. Registration of noise events introduces a randomly-occurring dead time, statistically enabling registration of signals scattered from the surface and bottom.

sertation suffers from a 270 nsec dead time following discrimination of received scattered light of sufficient intensity to enable the discriminator, equivalent to 30.5 m of water depth. In the event signals scattered from the surface defined by $\mathbf{F_1}$ are registered in both detection channels, as in the case of a depolarizing surface or sensor design with significant polarization crosstalk between channels, the sensor is unable to record events from the surface defined by $\mathbf{F_2}$, preventing a measurement of depth. Thus the signal photoelectrons scattered from the first surface $\overline{N}_{s,1}$ have the capacity to function as an additional noise term in Equation (4.46). Therefore, the discriminator threshold in the channel detecting signals scattered from the second surface must be configured sufficiently above the expected average noise level plus the expected "noise" contribution from a depolarizing first surface.

Ironically, the limitation on depth measurement imposed by the dead time of the detection electronics of low SNR sensors can be reduced, however, by increasing the false alarm rate. While typically understood to be a negative aspect of the low SNR approach, the false alarm probability can be adjusted to optimize the depth measurement by lowering the detection threshold k_{th}. Consider again the sensor simulated in this section. Maintaining a 1% probability of false alarm and examining range through a depolarizing first surface, a portion of the scattered signal $\overline{N}_{s,1}$ incidents the photodetector in each detection channel. Provided the first surface sufficiently depolarizes the incident laser light, the emitted photoelectrons will be discriminated and recorded in each channel, followed by the governing 270 nsec dead time which prevents resolving range to the second surface for depths less than 30.5 m.

"Through discrimination and recording of naturally-occurring noise events, the limitation on depth measurement imposed by the dead time of detection electronics is effectively removed."

If the detection threshold k_{th} is lowered, or equivalently the detection threshold is held $k_{th} = 10$ and the background noise level is increased, the false alarm rate rises dramatically. This effect is depicted in Figure (4.15), where the average noise photoelectron level has increased by an

order of magnitude to $\overline{N}_b = 12$. The result is an eight orders of magnitude increase in the probability of false alarm for the stationary detection threshold $k_{th} = 10$. Due to the increase, additional noise signals are discriminated and recorded by the timing electronics, resulting in an increase of the randomly-occurring dead time associated with the timing electronics. The incoherent nature of the noise terms in Equation (4.46) leads to this randomly-occurring dead time. Statistically, a noise event will periodically occur during the time period defined as 30 bins prior to the surface return. This noise signal is discriminated and recorded, generating a dead time that prevents the detection electronics from registering the surface return and enabling registration of the bottom scattered signal. Provided sufficient integration time, signals from both surfaces will be recorded, enabling a measurement of depth between surfaces. Through discrimination and recording of naturally-occurring noise events, the limitation on depth measurement imposed by the dead time of detection electronics is effectively removed, at the cost of increased integration time and degraded spatial resolution for ALB sensors. Ultimately, however, the signals scattered from surfaces of shallow depth overlap and are enveloped within the pulse width of the laser/detector. In this scenario, introduction of a randomly-occurring electronic dead time does not enable a depth measurement and optical techniques must be employed to resolve media depth, as described in the following chapter.

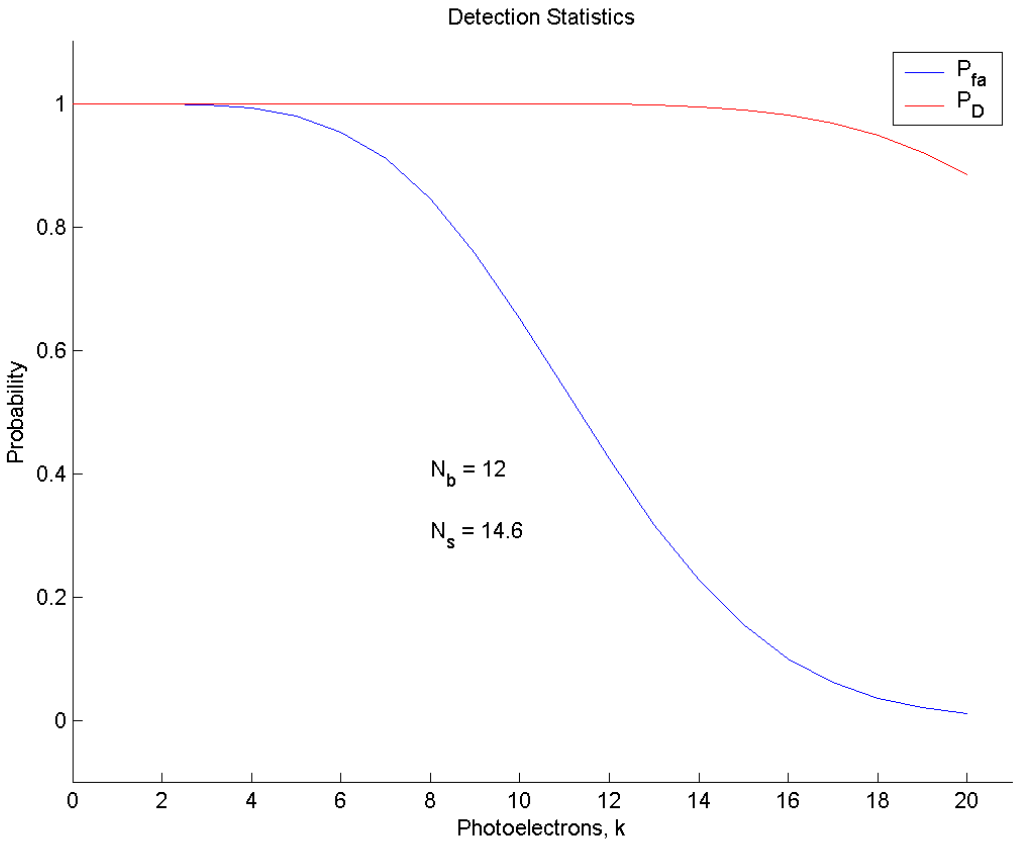

Figure 4.15: False alarm and detection probabilities for the simulated sensor. The average noise background has been increased by an order of magnitude, resulting an eight orders of magnitude increase in the false alarm probability for the stationary detection threshold $k_{th} = 10$.

Chapter 5

Intrapulse Phase Modification Induced by Scattering

5.1 Introduction

This chapter presents the Intrapulse Phase Modification Induced by Scattering (INPHAMIS) technique, a polarization technique that enables suppression of signals scattered from sequential media surfaces depending on their scattering phase matrix. Overlapping received signals scattered from sequential media surfaces of shallow depth can be isolated by exploiting their differing polarization characteristics. The INPHAMIS technique removes laser and detector pulse width limitations that define the governing time responsivity of conventional lidar sensors, translating the dual surface, shallow depth measurement into two single surface range-resolved observations. The technique achieves sub-pulse width resolution of sequential semitransparent media surfaces, and has led to publication [99] and patent [98].

5.2 Technique

Chapter 2 detailed the significant performance limitations that plague conventional range-resolved observations through distant shallow semitransparent media. The limit to achieving shallow depth measurement is related to the applied lidar technique and the governing time responsivity of the sensor, which defines the capacity of the lidar to distinguish between two surfaces along the same optical path but separated in range. Invariably, current techniques for determining shallow media depths are inhibited by the governing time responsivity of the lidar. For shallow aqueous media, such as the waters contained in fluvial environments and along the shoreline of supraglacial

melt lakes, limited instrument bandwidth results in ambiguities between surface and bottom scattered signals, making water depth indeterminable and leaving coverage gaps in bathymetric data [10].

Nayegandhi [103] described the difficulty associated with conventional lidar bathymetry sensors operating in shallow waters. *"Traditionally most lidar systems have a long [laser] pulse, but when you have a very long pulse it is hard to differentiate between two vertical objects that are close to each other. For lidar systems, when you want to map shallow submerged topography that is about 1 meter deep, you want to get a pulse that is as short as possible. ...The traditional bathymetric lidar system [sends] out a laser pulse that is fairly long, and when it enters the water column it is hard to differentiate between the water surface and bottom, when you have one pulse interacting with both surfaces. It's not impossible, it's just much harder to do.*" Recent development of so-called "topobathymetric" lidars have enhanced performance of the conventional sensor in the shallow water regime through a temporal reduction of the transmitted laser pulse width [102, 104], trading off performance in deeper waters due to the inherent reduction in pulse energy. While future development of picosecond pulse width lasers and fast detectors can further improve shallow water measurement capabilities through a reduction in governing time responsivity, these performance enhancements come at increased cost and complexity.

> ***"It is hard to differentiate between the water surface and bottom, when you have one pulse interacting with both surfaces. It's not impossible, it's just much harder to do."***
>
> **Amar Nayeganhdi**, 2013 International Lidar Mapping Forum

A novel approach to remote resolution of shallow media depths has been developed within the dissertation research, which has led to publication [99] and patent [98] opportunities. The approach exploits the naturally-occurring, differing polarization characteristics of received signals scattered from sequential media surfaces. For the lidar bathymetry sensor, the polarization preserving nature of the water surface and volume, as well as the depolarizing nature of rough bottom topographies,

has been demonstrated [29]. Signal returns from the depolarizing bottom can be isolated from surface and volume returns through polarization discrimination of the received scattered signals, at sub-pulse width resolution. Minimum depth resolution is no longer limited by laser or detector pulse width and instead places the demand on the timing electronics. Longer pulses and more optimal laser wavelengths may be used with no consequence on depth determination while potentially improving signal detection. The approach, which takes advantage of the naturally-occurring, intra-pulse phase modification induced by scattering (INPHAMIS) can equally be applied to deep water depth measurements, providing a complete range of depth determination capabilities unobtainable by conventional lidar sensors.

The timing diagram of Figure (3.2) is revisited and reconfigured in Figure (5.1) to illustrate the INPHAMIS approach. A laser pulse of temporal width τ is transmitted from the sensor at time t_0 through media with refractive index n_0 towards a distant semitransparent media. $\vec{S}_{TX}$ and $\mathbf{M_{TX}}$ are configured to effectively code the transmitted laser pulse with a linearly oriented electric field. The linearly polarized pulse intercepts the first surface with scattering matrix $\mathbf{F_1}$ and f_{22} element $a_1 = 1$ at time t_1. A portion of the laser pulse **1** reflects back to the receiver with a nearly preserved linear code. The remaining portion of the laser pulse is transmitted into the media with refractive index n_1. A portion of the transmitted energy **N** is scattered at the sequential surface defined by the scattering matrix $\mathbf{F_N}$ and f_{22} element $a_N < 1$ at time t_N and propagates back to the receiver. Scatterers defined within the depolarization matrix $\mathbf{F_N}$ modify the linearly coded laser pulse, effectively scrambling the polarization orientation of the pulse **N** returning to the receiver. The polarization analyzer in $\mathbf{M_{RX}}$ is configured to decode the information contained within each return pulse. In the event the depth between **1** and **N** is less than $c\tau/n_1$, the receiver discriminates the codes of each received scattered signal at sub-pulse width resolution.

In general, the INPHAMIS technique is applicable to shallow depth measurements between N surfaces provided that the scattering matrix $\mathbf{F_N}$ defining each surface is unique. For the lidar bathymetry sensor, signals scattered from the bottom of the water body ($N = 2$) must have $SNR_2 > 1$. Recall from Equation (4.38) that the received signal scattered from the second surface

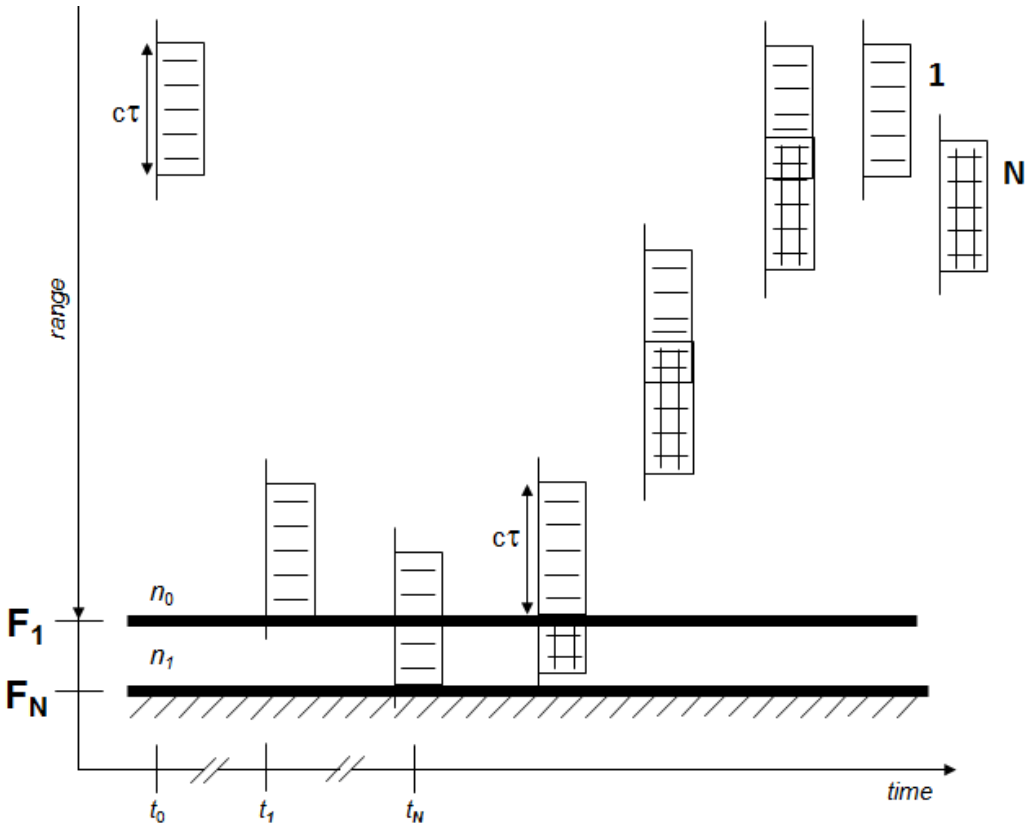

Figure 5.1: Timing diagram for range-resolved observations of shallow semitransparent media via the INPHAMIS technique.

has SNR_2 defined as

$$SNR_2 = \frac{\overline{N}_{s,2}}{\sqrt{\overline{N}_{s,2} + \overline{N}_{s,1} + \overline{N}_b}} \tag{5.1}$$

where the component of the received signal scattered from the water surface $\overline{N}_{s,1}$ is now considered a "noise" source in the shallow water regime in addition to the background $\overline{N}_b$ input to the receiver. From here it is clear that the SVLE approach of Equation (3.2) provides the definitions necessary to optimize the signal $\overline{N}_{s,2}$ received from the bottom in the presence of background noise and "noise" scattered from the first surface.

5.3 Simulation

A polarization lidar utilizing the INPHAMIS technique is simulated in this section for a transmitted laser signal polarized linear horizontal with 0.95 DOP and resulting normalized Stokes vector

$$\vec{S}_{TX} = \begin{bmatrix} 1 \\ 0.95 \\ 0 \\ 0 \end{bmatrix} \tag{5.2}$$

$\mathbf{M_{TX}}$ and $\mathbf{M_{RX}}$ are defined as identity matrices and the sensor detection channels are defined in Equations (4.7) and (4.8). The sensor ranges to a semitransparent medium bounded by $N = 2$ surfaces. Referring to Figure (5.1), the thickness of each surface is defined as $\ll$ than the transmitted laser pulse width $c\tau$,$n_0 = 1.00$, and $n_1 = 1.33$ corresponding to an arbitrary water body. The transmitted Stokes vector $\vec{S}_{TX}$ propagates through the media surfaces defined by the scattering matrices $\mathbf{F_1}$ and $\mathbf{F_2}$ defined in Equation (3.12) for $\beta_2 = 0.6\beta_1$ and $a_1 = 1.0$, $a_2 = 0.2$.

Figure (5.2) illustrates the simulated voltage output from the sensor photodetector, defined as a photomultiplier tube with 1.0 nsec rise time and 2.5 nsec FWHM output pulse length. The conventional lidar bathymetry sensor operates with polarization indiscriminate detection, receiving scattered signals from the $N = 1$ surface at time $t_1 = 0$ and the $N = 2$ surface at $t_2 = 3.5$ nsec. Given the response of the sensor to the received scattered signals from each surface, the

apex of each signal is readily identifiable in Figure (5.2) with a 3.5 nsec time differential and corresponding water depth of 40 cm. The variability in peak amplitude of each pulse is due to the definition $\beta_1 > \beta_2$. The simulation is repeated in Figure (5.3) for $N = 2$ surfaces and 1.5 nsec time differential between signals received from each surface, corresponding to a water depth of 17 cm. Given the time responsivity of the lidar, the received scattered signals begin to overlap at this depth. Further decrease in media depth, or β_2, will render the depth measurement indeterminable due to ambiguity between the overlapping received scattered signals.

The conventional lidar is replaced by a polarization discriminating lidar sensor detecting the perpendicular and parallel components of the received scattered signals. From Equations (4.12) and (4.13), the measured intensities in each detection channel are defined as $N_{\perp}^{1,2} = 0.025, 0.405$ and $N_{\parallel}^{1,2} = 0.975, 0.595$, respectively. As depicted in Figure (5.4), the measured intensities have been assigned to the peak amplitude of the photodetector voltage output, accounting for $\beta_2 = 0.6\beta_1$. Analysis of the polarization orientation of scattered signals received from each surface enables depth measurement at sub-pulse width resolution by suppressing signals scattered from the $N = 1$ surface in the perpendicular detection channel. In the shallow regime, resolution of depth between surfaces is now independent of the governing time responsivity of the sensor using the INPHAMIS approach. This effectively translates the N-surface range observation into N single-surface measurements by allowing the sensor to multiplex between surfaces based on their scattering phase matrix $\mathbf{F_N}$. Sensors working to achieve shallow depth measurements through incorporation of high performing components, such as the topobathymetric lidars previously mentioned, can achieve an order of magnitude improvement in shallow depth resolution with conventional components through evaluation of polarization characteristics of the received scattered signals.

The simulation continues to demonstrate timing data acquired for a calm water surface and bottom bounding 3 cm of water depth, corresponding to 270 psec, as illustrated in Figures (5.5) and (5.6). The apex of the photodetector voltage output of the form in Figures (5.2)-(5.4) is discriminated and recorded by the sensor timing electronics. Each range bin is assumed to be 27 psec wide, corresponding to 3 mm range resolution in water. A 270 psec (10 bin widths)

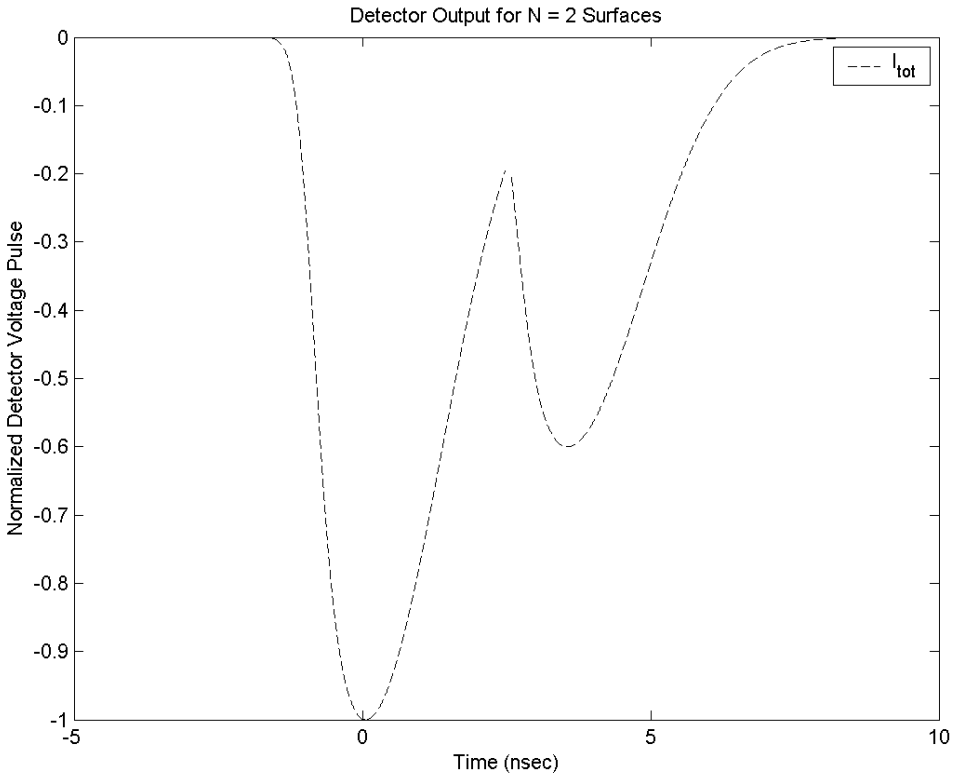

Figure 5.2: Voltage output from the photodetector of a conventional lidar sensor, ranging with polarization indiscriminate detection, for scattered signals received by the sensor from a simulated 40 cm water depth. The peaks of each received signal are readily identifiable ($t = 0$, $t = 3.5$ nsec) enabling a measurement of depth between surfaces.

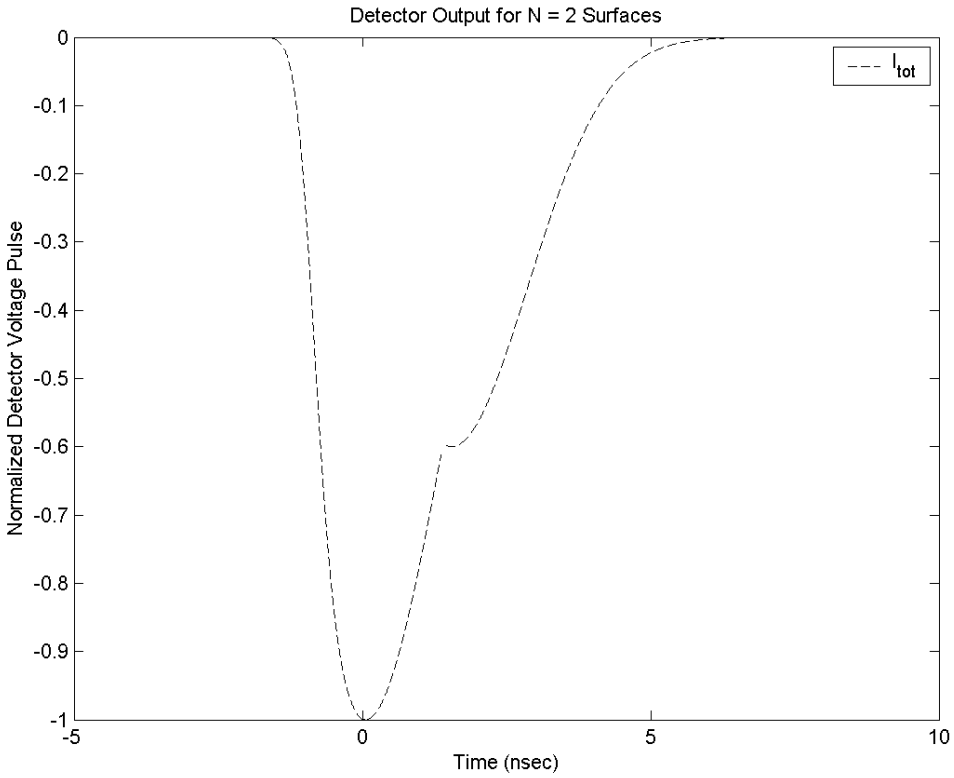

Figure 5.3: Voltage output from the photodetector of a conventional lidar sensor, ranging with polarization indiscriminate detection, for overlapping scattered signals received by the sensor from a simulated 17 cm water depth. Further decreases in depth between surfaces will render the depth measurement indeterminable due to overlap of the received scattered signals.

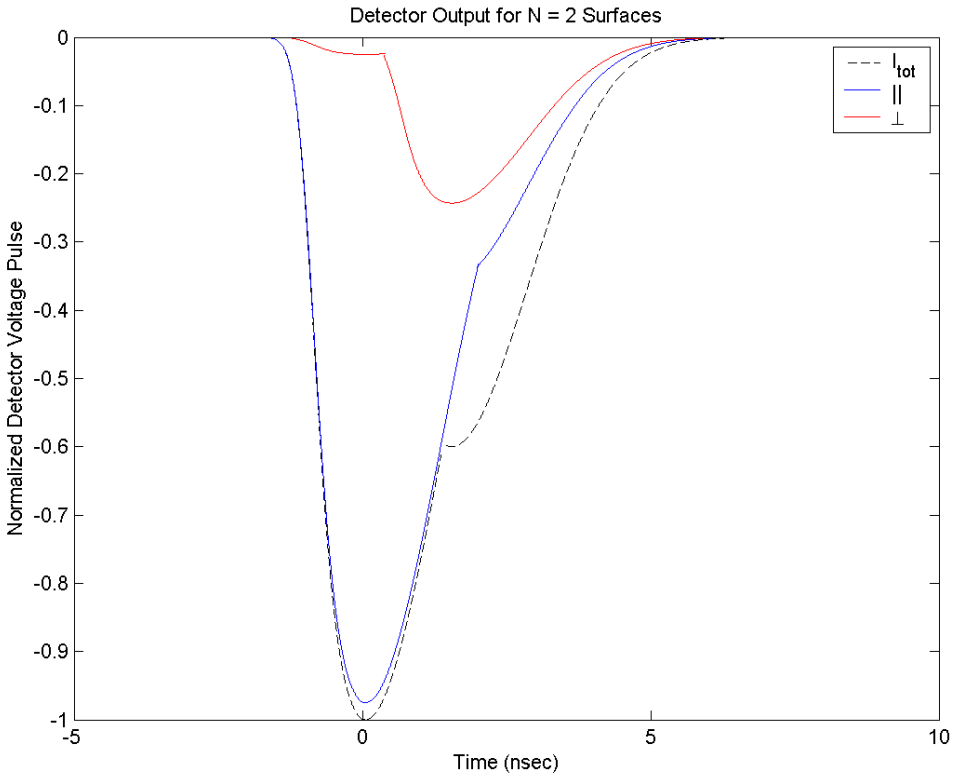

Figure 5.4: Voltage output from the photodetector of a polarization discriminate lidar sensor for overlapping scattered signals received by the sensor from a simulated 17 cm water depth. Optical discrimination of the polarization orientation of scattered signals received from each surface enables depth measurement at sub-pulse width resolution.

jitter is included in the photodetector response characteristics and produces the spread in recorded events from the surface and bottom timing histograms. The data in Figure (5.5) is simulated initially in the co-polarized detection channel to simulate a conventional polarization indiscriminate lidar bathymetry sensor, including discriminated and recorded noise events and a 30 bin width dead time associated with the detection electronics consistent with the simulations from Chapter 4.3.4.2. Received signals scattered from the water surface are defined by a polarization-maintaining scattering matrix, enabling the dead time associated with the detection electronics and preventing registration of signals scattered from the bottom. Unlike the measurements presented in Figure (4.14), however, recording noise events and introducing a randomly occurring electronic dead time does not aid in the depth measurement, as surface and bottom signals are contained within the envelope of the photodetector voltage output with 2.5 nsec governing time responsivity. As such, only the signal scattered from the water surface is recorded by the sensor and the randomly occurring electronic dead time does not benefit the measurement.

Figure (5.6) plots the timing data from both the co- and cross-polarized detection channels to simulate the polarization discriminate detection approach detailed in Chapter 4. The cross-polarized detection channel is defined here with identical performance characteristics as the co-polarized channel, including discrimination of noise events and a randomly occurring electrical dead time. Received signals scattered from the water surface are suppressed by the polarization analyzer in the receiver, enabling the sensor to record signals scattered from the depolarizing bottom, at sub pulse width resolution. The benefit of the INPHAMIS approach is readily apparent, as discrimination of the polarization orientation of the received optical signals has enabled the sensor to record events from the surface and bottom where both returns are contained within the envelope of the photodetector voltage output. The dual surface detection measurement has effectively been translated into dual single surface range-resolved observations.

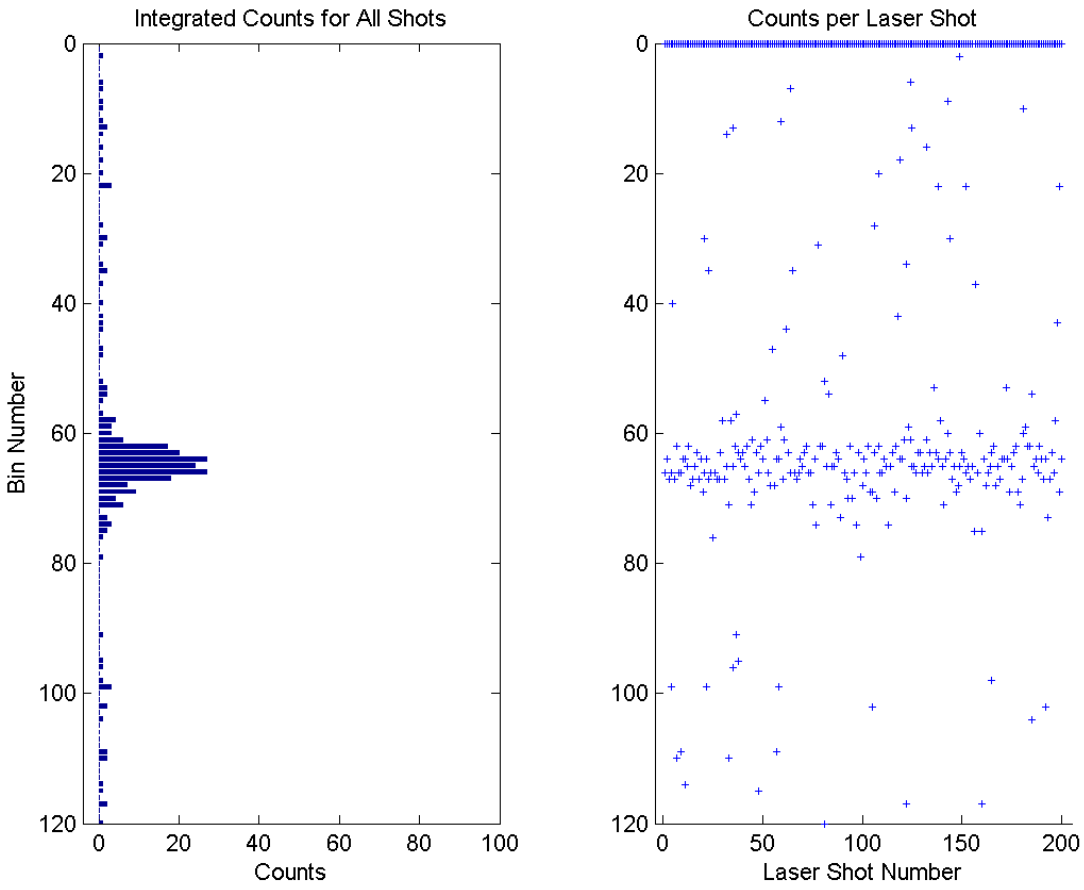

Figure 5.5: Simulated timing data for a flat water surface and bottom for 3 cm deep water. The data is simulated in the co-polarized detection channel to simulate a conventional polarization indiscriminate lidar bathymetry sensor, incorporating the expected pulse jitter from the photodetector, noise events, and the governing 270 nsec electrical dead time associated with the detection electronics. Received signals scattered from the water surface are defined by a polarization-maintaining scattering matrix, enabling the dead time associated with the detection electronics and preventing registration of signals scattered from the bottom. Introduction of noise events and a randomly occurring dead time does not aid in the measurement, as surface and bottom signals are contained within the envelope of the scattered waveform.

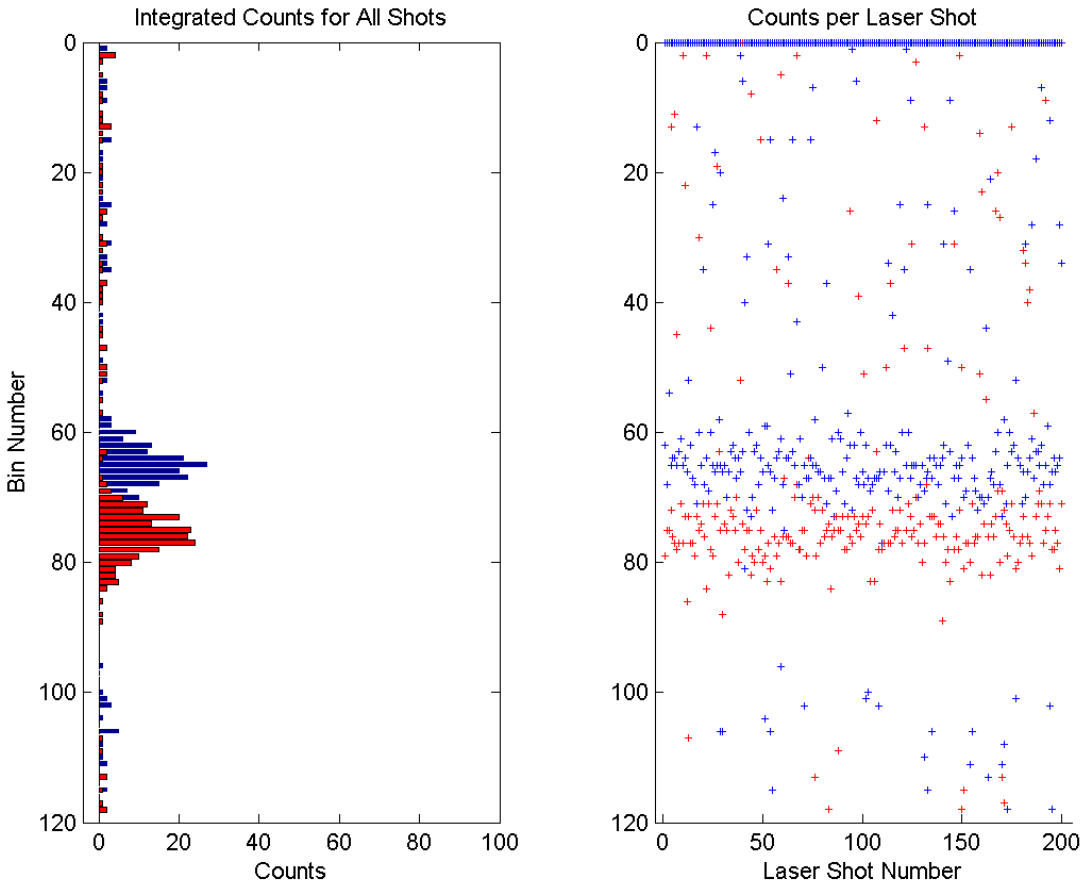

Figure 5.6: Simulated timing data for a flat water surface and bottom for 3 cm deep water. The data is simulated in the co- (blue) and cross-polarized (red) detection channels to simulate the polarization discriminate detection approach of Chapter 4. Received signals scattered from the water surface are suppressed by the polarization analyzer in the receiver, enabling the registration of signals scattered from the depolarizing bottom in the perpendicular detection channel at sub pulse width resolution.

5.4 Optimization

Operation of the INPHAMIS technique is optimized through evaluation of the SVLE. The Stokes vector $\vec{S}_{TX}$ describing the laser polarization orientation should be chosen for maximum degree of linearity and DOP. For the lidar configured to interrogate linear depolarization, particular emphasis must be paid to the design and implementation of $\mathbf{M_{TX}}$ and $\mathbf{M_{RX}}$ to minimize systematic coupling of energy into the perpendicular polarization plane that may prematurely enable the photodetector in the perpendicular detection channel for scattered signals received from the $N = 1$ surface [66], in particular avoiding the use of reflective components, and must be evaluated for their capacity to rotate or depolarize incident polarized light. Misalignment of the transmit and receive polarization planes must be calibrated for cross talk [5].

The ability of the instrument to range to sequential surfaces in the shallow regime requires transmission of linearly polarized light to a polarization preserving, semitransparent first surface followed by a depolarizing second surface. Instrument performance can be limited by the scattering matrix $\mathbf{F}$ of the surfaces. If the scattering matrix of the first surface couples sufficient energy into the perpendicular polarization plane to enable the photodetectors in both detection channels, the pulse overlap condition remains and the depth measurement is unobtainable.

The background contribution $\vec{N}_B$ must be evaluated when optimizing the sensor using the INPHAMIS technique. Although the received scattered signals polarized in the perpendicular plane can be suppressed from the first surface through proper configuration of $\mathbf{M_{RX}}$, background polarized light oriented outside of the transmission plane will contribute to the photodetector output in the perpendicular detection channel. In the presence of polarized background, the sensor should transmit in the same plane as the background and detect in the orthogonal plane in an effort to maximize SNR_2.

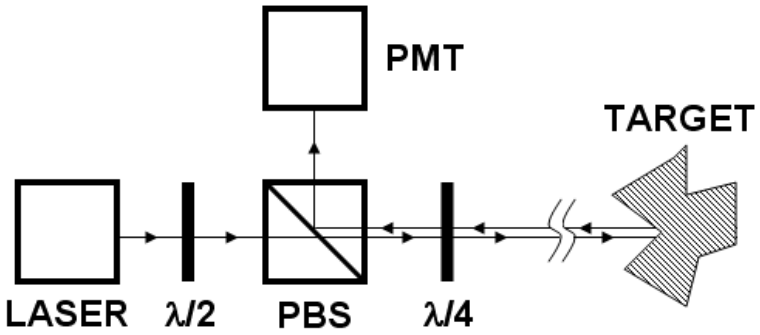

Figure 5.7: Diagram of the sensor developed to demonstrate the INPHAMIS technique.

5.5 Laboratory Demonstration

A laboratory-based sensor was developed within the dissertation research to demonstrate the applicability of the INPHAMIS technique to the lidar bathymetry measurement. In an effort to generate the most compact and inexpensive sensor design for potential future operations onboard a remote platform such as an UAS, the polarization discrimination between signals is performed in this section on a pulse-to-pulse basis using a single telescope and detector layout. The transmit and receive paths defining $\mathbf{M_{TX}}$ and $\mathbf{M_{RX}}$ are illustrated in Figure (5.7). The transmitter $\vec{S}_{TX}$ consists of a 532 nm linearly polarized laser. A halfwave plate is used to rotate the linearly polarized light exiting the laser head into alignment with the vertical transmission axis of a 532 nm polarizing beam splitter (PBS) cube. The vertically co-polarized laser light exiting the PBS passes through a quarterwave plate which is free to rotate about the optical axis. When the fast axis of the quarterwave plate is oriented 45° to the linear polarization output of the cube, the quarterwave plate retards the linear slow polarization component relative to the fast polarization component by 90°, emitting left-hand circularly polarized light towards the target water body.

When incident upon the water surface and column, the transmitted circularly polarized light reflects back to the receiver in a nearly preserving, but opposite, circular polarization state. This polarization, 180° out of phase from the transmitted state, is retarded again by the quarterwave plate oriented to 45°. The result is linearly polarized light incident upon the PBS, rotated about

the optical axis by 90° (horizontal) into the reflection axis of the PBS to a photomultiplier tube for detection.

When the quarterwave plate fast and slow axes are aligned to the PBS transmission plane, no relative phase shift is imposed by the quarterwave plate. As a result, vertically polarized laser light is transmitted to the water. The surface and column are polarization preserving, reflecting light that is primarily in the vertical plane. This linearly polarized light passes through the quarterwave plate unmodified so that the PBS does not reflect the light into the detection channel. However, when incident upon the bottom, the linearly polarized light depolarizes upon reflection due to the rough topography. The quarterwave plate has no impact on the backscattered unpolarized light, of which half is reflected by the PBS to the photodetector in the receiver.

Through discrimination of the reflected signal polarization state between laser firings, the lidar transitions between reception of water and bottom scattered signals. This translates the shallow water depth measurement into two independent range-resolved observations, where target selection is dictated by the definition of $\mathbf{M_{TX}}$ and $\mathbf{M_{RX}}$, specifically the orientation of the quarterwave plate. Rotation of the quarterwave plate permits the receiver to multiplex between detection of either state, even when surface and bottom signals are contained within the envelope of the return pulse. As such, the body of water can be effectively removed from the return signal, enabling the depolarized bottom signals to be isolated for analysis.

5.5.1 Simulation

Ranging through shallow semitransparent media using the setup in Figure (5.7) is dictated by the quarterwave plate orientation defining $\mathbf{M_{TX}}$ and $\mathbf{M_{RX}}$ and subsequent modification of transmitted and received polarization orientations. An analytical description of the technique begins by defining the associated Stokes vector of the linearly polarized laser pulse $\vec{S}_{TX}$ oriented

using a halfwave plate for maximum transmission through the polarizing beam splitter cube.

$$\vec{S}_{TX} = \begin{bmatrix} 1 \\ -1 \\ 0 \\ 0 \end{bmatrix} \tag{5.3}$$

$\mathbf{M_{TX}}$ is defined along the optical path by the halfwave plate, polarizer, and quarterwave plate. An arbitrary wave plate of phase shift γ and fast axis orientation θ is described using Mueller matrices as

$$VWP(\theta,\gamma) = \begin{bmatrix} 1 & 0 & 0 & 0 \\ 0 & \cos^2(2\theta) + \cos(\gamma)\sin^2(2\theta) & \cos(2\theta)\sin(2\theta) - \cos(2\theta)\sin(2\theta)\cos(\gamma) & -\sin(2\theta)\sin(\gamma) \\ 0 & \cos(2\theta)\sin(2\theta) - \cos(2\theta)\sin(2\theta)\cos(\gamma) & \cos(\gamma)\cos^2(2\theta) + \sin^2(2\theta) & \cos(2\theta)\sin(\gamma) \\ 0 & \sin(2\theta)\sin(\gamma) & -\cos(2\theta)\sin(\gamma) & \cos(\gamma) \end{bmatrix} \tag{5.4}$$

with a halfwave plate γ of π radians oriented to θ_H and quarterwave plate γ of $\pi/2$ radians oriented to θ_Q. The PBS is modeled as a polarizer oriented to θ_P of 0° for transmission along the vertical axis in the instrument transmitter and oriented to $\theta_P + 90^\circ$ for horizontal transmission in the receiver. The Mueller matrix describing the polarizer is described according to

$$P(\theta) = \begin{bmatrix} 0.5 & 0.5\cos(2\theta) & -0.5\sin(2\theta) & 0 \\ 0.5\cos(2\theta) & 0.5\cos^2(2\theta) & -0.5\left(\cos(2\theta)\sin(2\theta)\right) & 0 \\ 0.5\sin(2\theta) & 0.5\left(\cos(2\theta)\sin(2\theta)\right) & -0.5\sin^2(2\theta) & 0 \\ 0 & 0 & 0 & 0 \end{bmatrix} \tag{5.5}$$

During acquisition of range-resolved observations, the quarterwave plate is initially oriented to θ_Q of 45° for transmission of circularly polarized light towards the target. After an arbitrary number of laser firings in this orientation, the quarterwave plate is rotated to θ_Q of 0° for transmission of vertical linear polarization during a second set of laser firings. In both orientations the scattered light propagates in the opposite direction from the transmit path, such that the quarter-wave plate is expressed with orientation of θ_Q during signal reception.

Combining the transmitted Stokes vector in Equation (5.3) with the appropriate Mueller matrices described in Equations (5.4) and (5.5) produces the received Stokes vector

$$\vec{S}_{RX} = \left[Pol\left(\theta_P + 90\right) VWP\left(-\theta_Q, \frac{\pi}{2}\right) \mathbf{F_{1,2}} VWP\left(\theta_Q, \frac{\pi}{2}\right) Pol\left(\theta_P\right) VWP\left(\theta_H, \pi\right) \right] \vec{S}_{TX} \tag{5.6}$$

with the intensity measured by the photodetector defined as

$$I_{RX} = \begin{bmatrix} 1 & 0 & 0 & 0 \end{bmatrix} \vec{S}_{RX} \tag{5.7}$$

The Mueller matrices $\mathbf{F_{1,2}}$ represent the scattering phase function of the semitransparent media and take the form of Equation (3.12). For water surface and volume returns the magnitude of a, b, and c are all approximately 1. In this way the targets are polarization maintaining. However, for rough bottom topographies, these terms are generally of magnitude < 1.

Simulation of the normalized received intensity for surfaces of variable a is illustrated in Figure (5.8). Received signals scattered from a polarization maintaining target ($a = 1$) such as the water surface appear sinusoidal, while a depolarizing target ($a < 1$) such as ice approaches a constant intensity of 0.5. By rotating the quarterwave plate between orientations θ_Q of $45\,^\circ$ and $0\,^\circ$ during bathymetric measurements, received signals transition between polarized water surface and volume returns and depolarized bottom returns.

5.5.2 Measurements

Bathymetric measurements were made using the sensor configuration in Figure (5.7). The transmitter consisted of a CW-diode pumped passively Q-switched frequency-doubled Nd:YAG microchip laser. The laser outputs 2.45 μJ of linearly polarized 532 nm light at a repetition rate of 14.3 kHz and pulse width of 450 psec. A half-wave plate aligned the laser polarization to the vertical transmission plane of a 532 nm PBS. Light exiting the PBS was transmitted through a quarterwave plate toward a controlled target consisting of a column of water on top of a depolarizing ice substrate, used to replicate expected conditions for depth determination of a supraglacial melt lake.

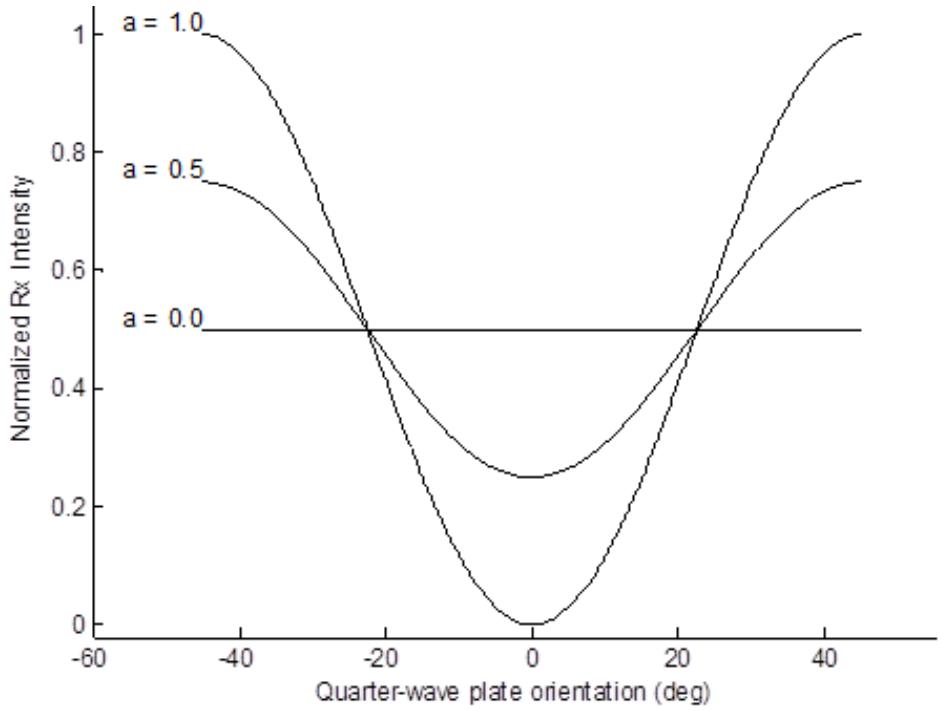

Figure 5.8: Simulation of normalized received intensity for a range of quarterwave plate orientations for targets of varying degrees of vertical linear depolarization a.

Backscattered laser light received by the sensor was collected with a photomultiplier tube, Hamamatsu model H7422P. The PMT operates with a 1 nsec rise time and 350 psec timing jitter during output of a 2.5 nsec FWHM pulse. Each PMT pulse is passed through a constant fraction discriminator (CFD) which determines the PMT signal apex independently of the signal pulse height. The CFD operates with an intrinsic timing jitter of 3.2 psec, outputting a 2.4 volt TTL-level pulse that is passed to and stored onboard a time to digital converter (TDC) with 27 psec timing resolution.

Timing data were acquired during reception of scattered signals from known water depths of 3 and 1 cm over ice in an effort to simulate a shallow supraglacial lake. The transmitted laser pulse was oriented slightly off nadir for collection of water surface and bottom returns during each measurement. In the first data set, the quarterwave plate was oriented to θ_Q of 45° for reception of polarized surface signals. The second data set was then acquired with the quarterwave plate oriented to 0° to collect backscatter from the depolarizing floor.

The TDC produces a histogram with a 27 psec bin width and one bin entry per laser firing, allowing for determination of the average time at which the detector pulses are registered. Figure (5.9) illustrates the outline of the surface and bottom digital timing histograms for each depth measurement. Visible in Figure (5.9) is an initial histogram of timing counts extracted from the water surface returns measured over multiple laser pulses with the quarterwave plate oriented to θ_Q of 45°. The second histogram is from the bottom returns measured over multiple laser pulses with the quarterwave plate oriented to θ_Q of 0°. Each histogram was normalized to its maximum count value.

The histograms shown in Figure (5.9) have a width that is dictated by pulse jitter from the PMT and the laser pulse width. Generally these distributions are expected to appear Gaussian; however, the histograms have an asymmetric shape due to operation of the PMT in the near range environment associated with the laboratory setting, requiring the PMT control supply voltage to be reduced below the nominal 0.80 V setting and resulting in abnormal detection operation of the photodetector. The CFD is set to an initial voltage discrimination threshold to pass signals

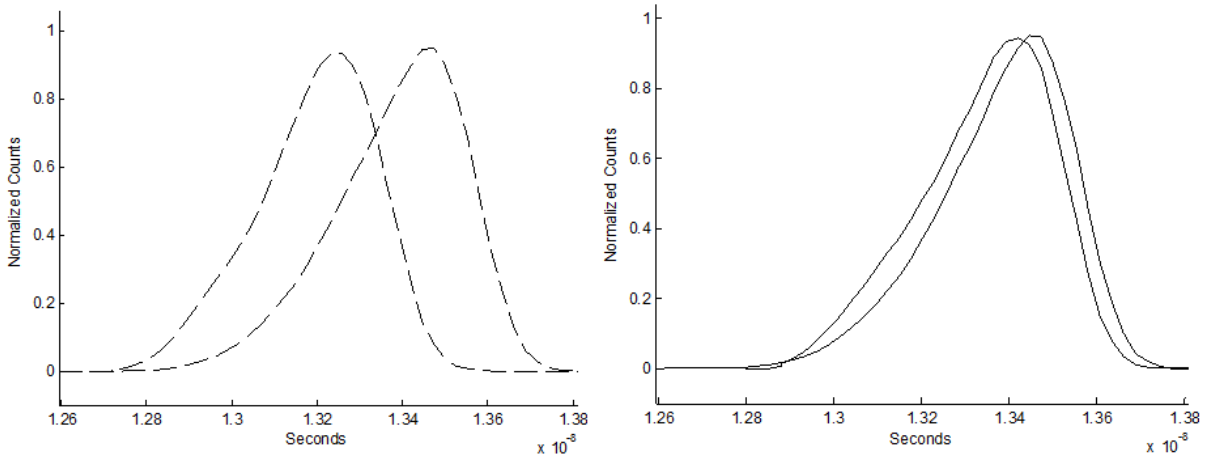

Figure 5.9: Outline of the normalized digital timing histograms for surface and bottom returns at 3.0 cm (dashed) and 1.0 cm (solid) water depths.

from surface and floor returns and suppress constant fraction discrimination of noise signals. The TDC is operated in multichannel scalar mode and initiates counting when the laser is fired. At the quarterwave plate orientation θ_Q of 45 °, the surface return is the first photon detected by the CFD and recorded by the counter. Subsequent return signals from the propagating laser pulse are not counted in shallow waters due to dead time of the electronics. At this point the TDC waits for another laser pulse to fire and a histogram of surface returns is produced as illustrated in Figure (5.9). Upon rotating the quarter-wave plate to θ_Q of 0 °, the detected signal originates from the floor and a second, distinct histogram is produced. The histograms, therefore, represent detection of the first counted photon from each pulse. If the probability of detecting a photon at time t is given by $P_d(t)$, the timing probability distribution function (PDF) for counting a photon in first count mode (FCM) is given by

$$P_{FCM}(t) = P_d(t) \int_0^t (1 - P_d(\tau))\, d\tau \tag{5.8}$$

which is the probability of detecting the photon at time t multiplied by the probability that no photons were previously detected. Thus, in instances where the photon detection probability from a single pulse approaches 1, the PDF appears Gaussian for small values of t. As t increases, the integral term dominates and causes the PDF to fall sharply. This results in the histogram asymmetry visible in Figure (5.9). Additionally, at times where the integral term dominates, uncertainty due to shot noise is minimized. This is a direct result of the integration and supports the claim that the trailing edge of the timing histogram provides the most stable reference for calculating timing delays for water depth measurement.

Taking into account the refractive index n change of water relative to air ($n = 1.33$), the water depth d is calculated as

$$d = \frac{c\Delta t}{2n} \tag{5.9}$$

where the time delay Δt is evaluated by differencing the half max of the trailing edge timing points of the constant fraction histogram for the surface returns and the constant fraction histogram for the floor returns. The results presented in Figure (5.9) produce time delays of 247 and 52 psec,

corresponding to depth measurements d of 2.7 and 0.6 cm, respectively. The 27 psec resolution of the TDC imposes a ± 3 mm uncertainty on the water depth estimate, placing the observed depths within the uncertainty of the physically measured depths of 3.0 and 1.0 cm, which possess a ± 1 mm uncertainty.

The results presented in Figure (5.9) demonstrate the reduction of governing time responsivity limitations through analysis of the polarization orientation of received scattered signals. If the conventional scalar bathymetric approach was employed, given the 450 psec laser and 2.5 nsec detector response widths, water depths less than tens of cm could not be resolved due to pulse ambiguity. By isolating detection of surface and floor returns using polarization discrimination, water depth measurements are limited only by the 27 psec resolution of the TDC. By removing the need for short laser pulses and fast detectors, lasers and detectors with other favorable performance attributes can be used. For instance, lasers of longer pulse width can transmit more energy per pulse and improve the signal-to-noise aspects of the system, lasers of more favorable transmission wavelengths can be utilized, and less expensive lasers and detectors can be employed.

To demonstrate independently the extent of the depth capability of the system, the experiments are revisited. For these measurements, the floor distance remained fixed while 1 and 3 cm water depth experiments were performed. Contrasting the setup between measurements, each floor return in the 3 cm water experiment is subject to a transit distance l of 2 cm of water compared to floor returns traveling through 2 cm of air before entering the 1 cm water depth experiment. In this sense, it is expected that the floor return for 3 cm of water would be delayed from the floor return for 1 centimeter by a factor Δ where

$$\Delta = \frac{2nl}{c} - \frac{2l}{c} = \frac{2\,(1.33)\,(0.02)}{(3 \times 10^8)} - \frac{2\,(0.02)}{(3 \times 10^8)} = 44psec \tag{5.10}$$

This is due solely to the change in n from water to air over the $2l$ roundtrip distance.

The floor results of each water depth experiment are plotted together in Figure (5.10). Inset is a zoomed-in view of the half max timing points of the trailing edges for the floor return curves corresponding to water depths of 3 and 1 cm. Trailing edge values were used due to their accuracy,

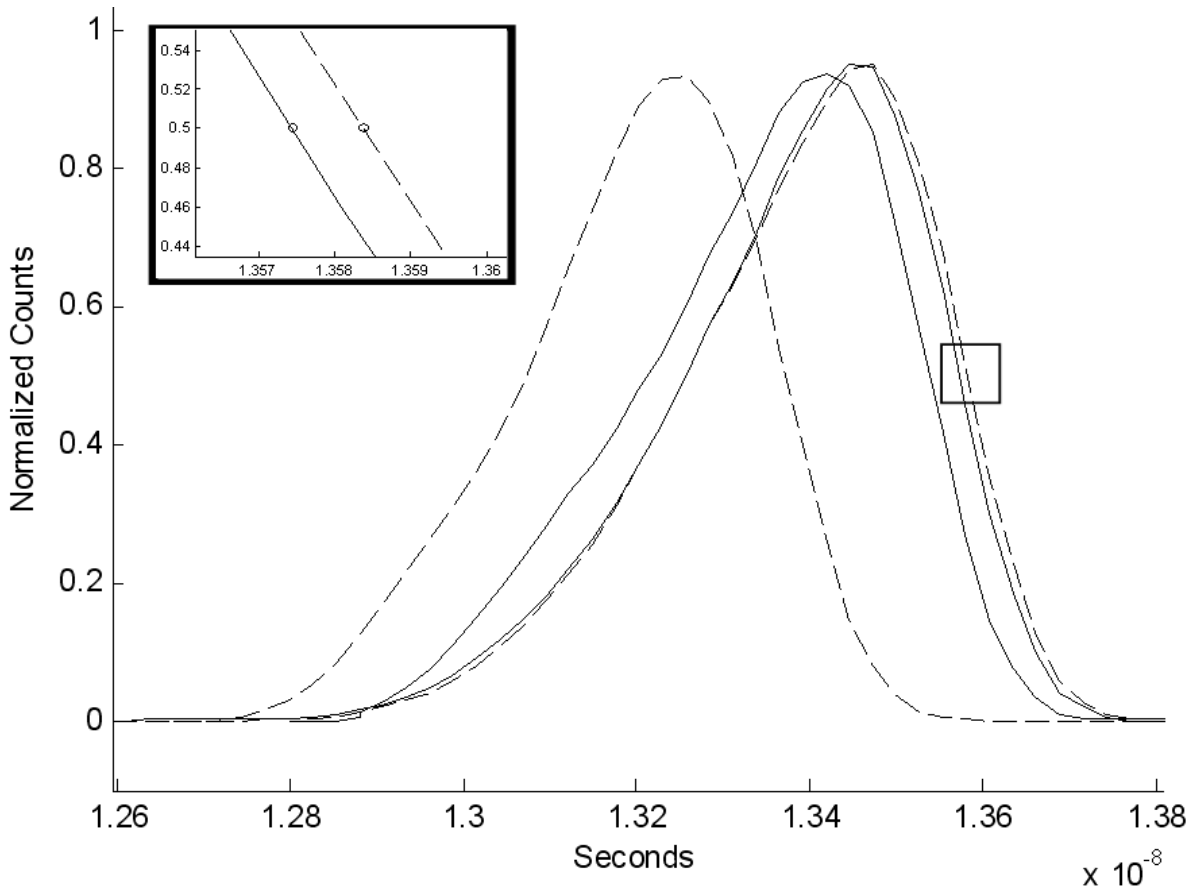

Figure 5.10: Overlay of normalized surface and bottom histograms from Figure (5.9) along with insert of timing differences between the two determined bottom returns.

repeatability, and reduced shot noise levels, as explained. At an expected Δ of 44 psec, the floor returns for each experiment would be separated by one 27 psec timing bin in the digital timing unit.

Differencing the FWHM timing points of the Figure (5.10) inset demonstrates the returns from the floor of 3 and 1 cm water depths are located in neighboring bins, although the TDC cannot determine their location better than within its 27 psec resolution. The measurement comparison demonstrates that the ultimate timing resolution of the technique is dictated by the timing bin width and presently indicates depths could be determined to within millimeters.

"The measurement comparison demonstrates that the ultimate timing resolution of the technique is dictated by the timing bin width and presently indicates depths could be determined to within millimeters."

5.6 Conclusions

While the single telescope and detector approach to the INPHAMIS technique may be the most compact and inexpensive sensor layout, operational limitations suggest a dual detection channel approach may be optimal for ALB operations. The rotating quarterwave plate and single detector approach lacks robustness. The transit time required to rotate the quarterwave plate between orientations is on the order of seconds, severely restricting spatial coverage of an airborne sensor. The single detection channel lacks simultaneity, prohibiting the sensor from providing an estimation of the depolarization ratio of target media. Additionally, the coaxial sensor layout is prone to internal scatter as the light emitted from the laser transmits through the PBS, which can reduce the lifetime of the PMT and generally hampers the discriminator and TDC electronics. Finally, the ultimate repeatability of the quarterwave plate rotation mount is unknown outside of the controlled laboratory environment, leading to concerns over polarization purity and crosstalk between detection configurations. The dual detection channel sensor is presented in Chapter 6, which increases the robustness of the INPHAMIS approach by removing all rotating components and separating

the transmit and receive optical paths. Applying the SVLE to the dual detection channel sensor results in an optimal approach to the INPHAMIS technique.

As detailed in this chapter, the INPHAMIS technique has had tangible impact on the noncontact optical remote sensing community within the time of the dissertation research, particularly in the lidar bathymetry community. In their 2012 textbook Fluvial Remote Sensing for Science and Management, Carbonneau and Piégay [23] explicitly state that *"in the future, hardware and software developments will enhance the resolution, accuracy, and types of data products derived from riverine airborne lidar surveys. First, the use of polarized lidar will probably enhance the capacities of extremely shallow water bathymetry (Mitchell et al., 2010)."* By exploiting the polarization orientation of scattered signals received from sequential media surfaces, such as water surface and bottom returns, the governing time responsivity limitations associated with conventional lidar sensors are mitigated. Range-resolved observations through semitransparent media, once confined by laser or detector pulse widths conventional lidar sensors, are now limited only by the resolution of timing electronics. The INPHAMIS technique as presented here has demonstrated 1 cm water depth with ± 3 millimeter uncertainty, more than an order of magnitude improvement over previous approaches to bathymetry lidar, with potential for mm depth measurement. Reduction of conventional limitations imposed by time responsivity decreases the need for expensive lasers and optical detectors with narrow pulse widths to measure shallow media depths, allowing for increased flexibility in component selection criteria such as wavelength. The INPHAMIS approach can equally be applied to deep water depth measurements, thus providing a complete range of depth determination capabilities.

Chapter 6

Instrumentation

6.1 Introduction

This chapter details the design and operation of a prototype polarization lidar developed within the dissertation research. The sensor applies the theory developed in Chapters 3-5 to range-resolved observations through semitransparent media to evaluate performance of the sensor architecture beyond the laboratory environment. The design of and initial measurements obtained with the sensor have led to publication [97].

6.2 Sensor Overview

A prototype polarization lidar was developed in the latter stages of the dissertation research to demonstrate the theory developed in Chapters 3-5 during range-resolved observations through semitransparent media external to the laboratory environment. A block diagram and image of the sensor are presented in Figure (6.1).

6.2.1 Design

The laser transmitter consists of a cw-diode-pumped passively Q-switched frequency-doubled Nd:YAG microchip laser. The laser outputs 2.45 μJ of linearly polarized 532 nm light at a repetition rate of 14.3 kHz and pulse width of 450 psec. The transmitted beam passes through a 5 times beam expander to achieve a divergence of 1.8 mrad. A halfwave plate aligns the laser polarization to the transmission plane of a 532 nm Glan Thompson polarizer to ensure maximum linearly polarized

output with degree of polarization (DOP) greater than 99.99%. Light exiting the polarizer is transmitted through a pair of Risley prisms configured to steer the transmitted light into alignment with the biaxial receiver. Optical leakage from the outgoing laser pulse is sampled by a fast photodiode, which time-tags the start pulse with a SensL HRMTime time-to-digital converter. At a nominal flight altitude of 300 m, typical of low flying UAS, the projection of the laser beam yields a 0.5 m diameter footprint on the ground.

Table 6.1: Transmitter and Receiver Specifications of the Prototype Polarization Lidar

Parameter	**Value**
Transmitter	
Wavelength	532 nm
Laser pulse energy	2.45 μJ
Pulse repetition rate	14.3 kHz
Pulse width, FWHM	450 psec
Beam divergence	1.8 mrad
DOP	linear $>$ 99.99%
Receiver	
Aperture diameter	90 mm
Field of view	2 mrad
Spectral filter bandwidth	1 nm
PMT pulse width, FWHM	2.5 nsec
CFD pulse width, TTL	270 nsec
TDC bin width	27 psec

The receiver consists of a F/13.9 Maksutov-Cassegrain telescope with a 1250 mm focal length and 90 mm aperture. An iris located at the focal point of the telescope is adjusted to control the receiver field of view. The transmit and receive paths fully overlap at 150 m range as defined by the geometrical overlap function $G(R)$ of the sensor as illustrated in Figure (6.2). The collected light is collimated by a 25 mm positive lens and passed through an interference filter (1 nm bandwidth) and Glan Taylor polarizer. The halfwave plate and Glan Thompson polarizer in the transmitter are oriented to align the laser polarization plane with the reflection axis of the Glan Taylor polarizer in the receiver. The Glan Taylor functions as a polarization analyzer in the receiver, reflecting scattered signals oriented parallel to the transmitted polarization plane and passing perpendicular

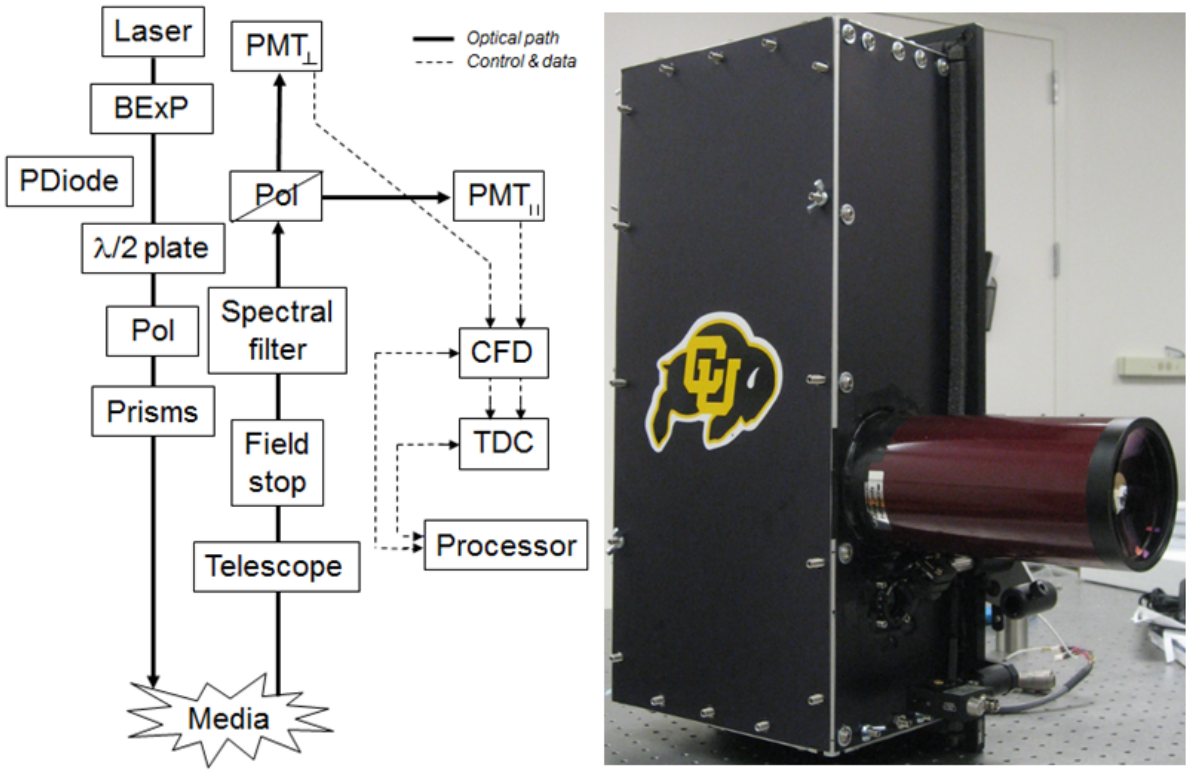

Figure 6.1: Block diagram (left) and image of the prototype polarization lidar sensor (right). The lidar transmits 532 nm laser light oriented in a linear polarization plane and simultaneously detects the parallel and perpendicular components of the received scattered light.

signals.

6.2.2 Mitigation of Polarization Effects

The SVLE of Equation (3.2) provided the foundation for the optical design of the sensor. Optimal performance of the Mueller matrices describing the transmit and receive paths $\mathbf{M_{TX}}$ and $\mathbf{M_{RX}}$ required evaluation of each optical element in the sensor for potential introduction of polarization effects along the optical path, and subsequent mitigation of these effects. To minimize systematic polarization effects of the instrument transmit and receive paths on a global scale, no reflective components were used in the system beyond the Matsukov-Cassegrain telescope, chosen for its low reflectance angles. Furthermore, the capacity of each optical element in $\mathbf{M_{TX}}$ and $\mathbf{M_{RX}}$ was evaluated for potential to modify the Stokes vector describing the transiting laser light.

The evaluation procedure is described here. Recalling Equation (3.5), a Stokes vector can be written as [18]

$$\vec{S} = S_0 \begin{bmatrix} 1 \\ p\cos(2\varepsilon)\cos(2\theta) \\ p\sin(2\varepsilon)\cos(2\theta) \\ p\sin(2\theta) \end{bmatrix} \tag{6.1}$$

where S_0 is the total intensity, p is the degree of polarization (DOP), ε is linear rotation angle and θ is the ellipticity angle as illustrated in Figure (3.3). The Stokes vector exiting each optic along the path is fully defined by these three polarization variables which are easily mapped onto the Poincare Sphere. The measurement [52] requires a polarizer and a quarterwave plate, each in a calibrated mount. The setup for each measurement are defined according to

- Setup 1: sensor optical component → polarizer → detector
- Setup 2: sensor optical component → quarterwave plate → polarizer → detector, as illustrated in Figure (6.3).

Beginning with Setup 1, the polarizer is rotated to maximize the amount of signal on the detector,

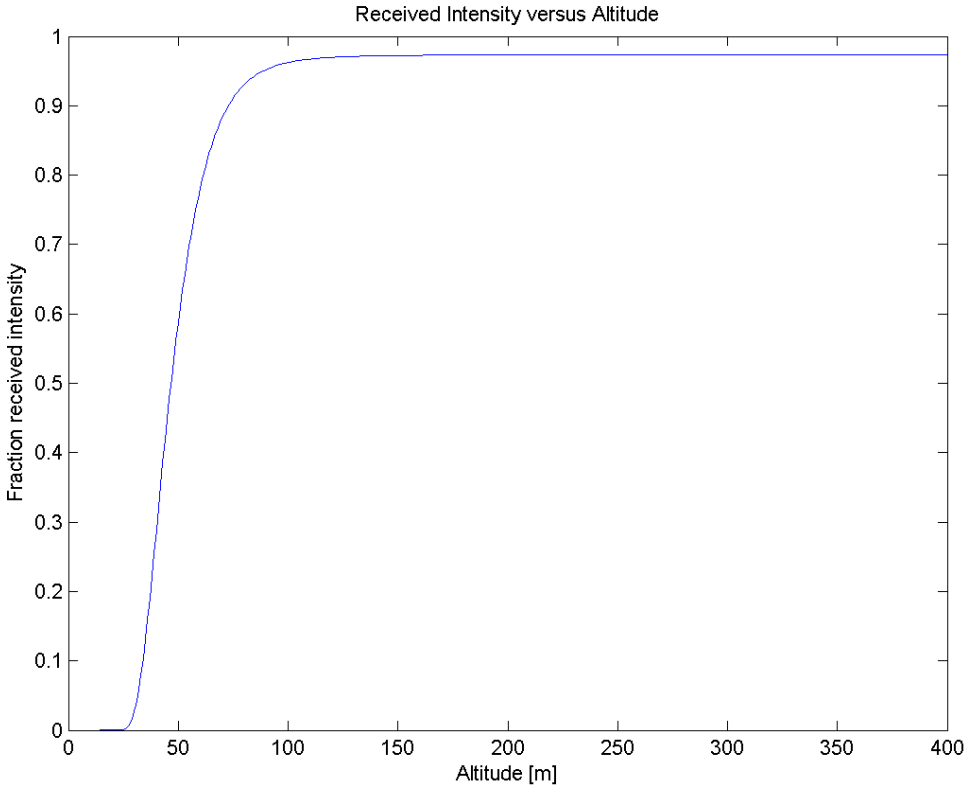

Figure 6.2: Geometrical overlap function $G(R)$ of the prototype polarization lidar as a function of range. The transmit and receive paths overlap at 150 m range such that $\geq 97\%$ of the scattered signal is received by the telescope.

I_{max1}. Since detectors are prone to saturation, the polarizer is then rotated to minimize the signal on the detector, I_{min1}. The angle of the polarizer, θ_{pol1}, is recorded to determine the linear rotation angle of the Stokes vector,

$$\varepsilon = 90^\circ + \theta_{pol1} \tag{6.2}$$

and the total intensity of the Stokes vector is calculated according to

$$S_0 = I_{min1} + I_{max1} \tag{6.3}$$

The quarterwave plate is inserted into the optical path to produce Setup 2 and rotated sequentially with the polarizer to minimize the signal on the detector, I_{min2}, at the new polarizer position θ_{pol2}. If the fast axis of the quarterwave plate is unknown, only the absolute value of the ellipticity angle can be determined according to

$$\theta = |\theta_{pol1} - \theta_{pol2}| \tag{6.4}$$

The polarizer is rotated to maximize the signal on the detected, I_{max2}. The DOP given by

$$p = 1 - \frac{2I_{min2}}{I_{max2} + I_{min2}} \tag{6.5}$$

which normalizes out the efficiency of the quarterwave plate, providing the most accurate measurement of p.

Having acquired the necessary measurements to define S_0, p, ε, and θ, the Stokes vector exiting each element of $\mathbf{M_{TX}}$ and $\mathbf{M_{RX}}$ is evaluated using Equation (6.1). Measuring the Stokes vector exiting each element along the path indicates the polarization performance of each element. The sensor developed in the dissertation is motivated by the evaluation of depolarizing semitransparent media. As such, $\mathbf{M_{TX}}$ and $\mathbf{M_{RX}}$ have been configured to maximize the DOP of the transmitted laser energy and minimize the potential for optical elements to retard or depolarize the transiting signal.

As discussed in Chapter 3, the scalar approach to polarization gives quantitative description as to *how much* the transmitted polarization orientation has changed, not *how* the polarization

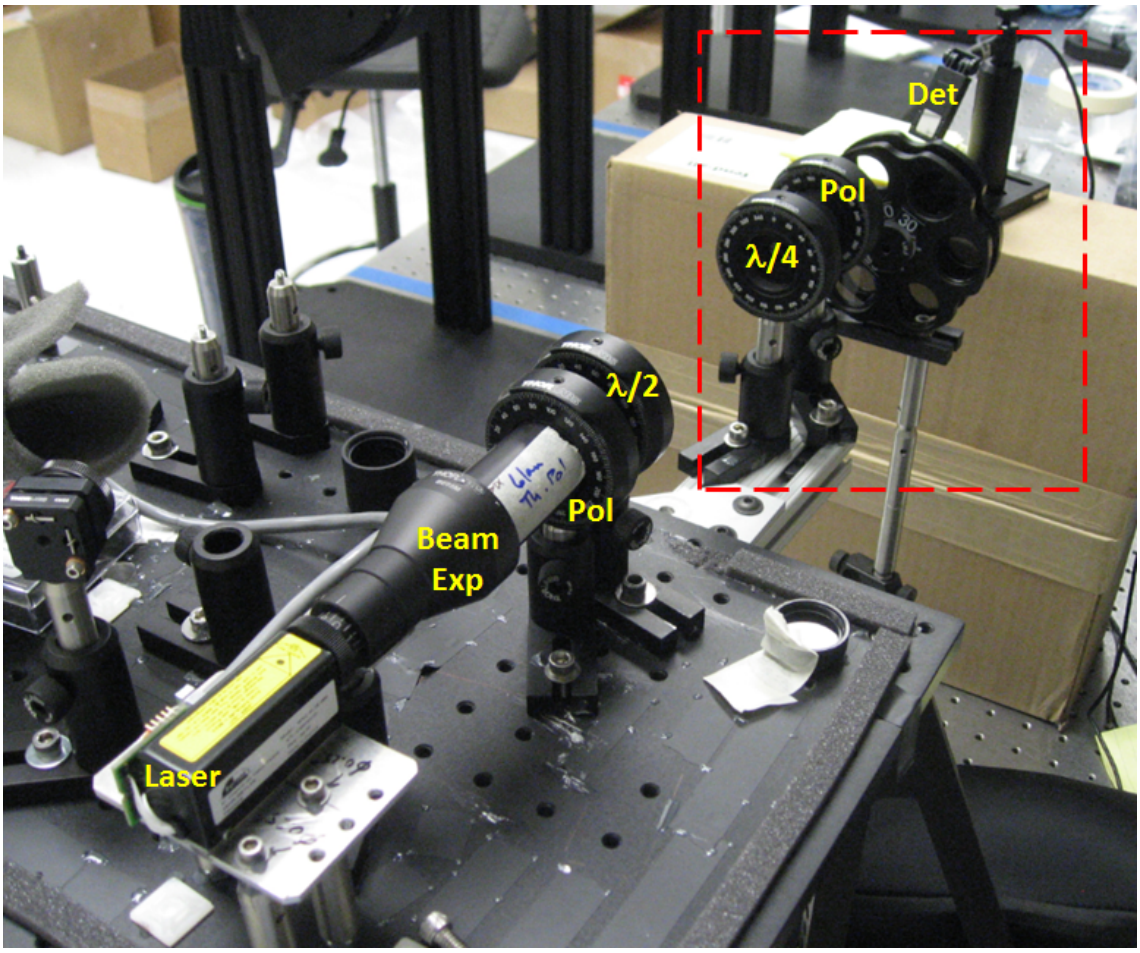

Figure 6.3: Measurement setup for the process of evaluating the capacity of each optical element in $\mathbf{M_{TX}}$ and $\mathbf{M_{RX}}$ to modify the Stokes vector of the transiting laser light. Analyzing optics are highlighted by the red dashed box and consist of a quarterwave plate, polarizer, and photodetector. Based on the results of the measurement shown here, it was determined that the halfwave plate decoupled the polarization of the transiting laser signal. As a result, the positions of the halfwave and polarizer were reversed, enabling the polarizer to reject the cross-polarized component.

changed. To highlight the performance restrictions introduced by the scalar approach, example Stokes vector measurements are presented here, beginning with the laser. Using the setup described in this subsection as illustrated in Figure (6.4), the total intensity of the laser was measured to $S_0 = 29.3mW$, linear rotation angle $\varepsilon = 90\,^\circ$, ellipticity angle $\theta = 28\,^\circ$, and degree of polarization $p = 0.6785$ resulting in a measured Stokes vector exiting the laser of

$$\vec{S}_{TX} = 0.0293 \begin{bmatrix} 1 \\ -0.379 \\ 0 \\ 0.562 \end{bmatrix} \tag{6.6}$$

The measured Stokes vector exiting the laser indicates that the laser transmits in the vertical linear plane with a significant elliptically polarized component. In addition, the laser transmits a large unpolarized component (0.32). The demand for the SVLE is immediately evident based on the measurement. Without analyzing the polarization performance of the laser, the received signal scattered from a semitransparent media will contain a cross-polarized component with ambiguous origin.

The performance of each element of the sensor $\mathbf{M_{TX}}$ and $\mathbf{M_{RX}}$ was evaluated in similar fashion. Figure (6.3) illustrates measurement of the Stokes vector exiting the laser, beam expander, Glan Thompson polarizer, and halfwave plate train of optics. The halfwave plate was found to decouple the incident polarization, requiring the positions of the Glan Thompson polarizer and halfwave plate to be reversed in an effort to maximize the DOP exiting the sensor transmit path. Following analysis of each element in the transmit path, the resulting Stokes vector exiting the instrument was configured to transmit linear vertical polarization with $S_0 = 3.1mW$, linear rotation angle $\varepsilon = 90\,^\circ$, ellipticity angle $\theta = 0\,^\circ$, and $p = 0.9999$ such that

$$\vec{S}_{TX}\mathbf{M_{TX}} = 0.0031 \begin{bmatrix} 1 \\ -0.99 \\ 0 \\ 0 \end{bmatrix} \tag{6.7}$$

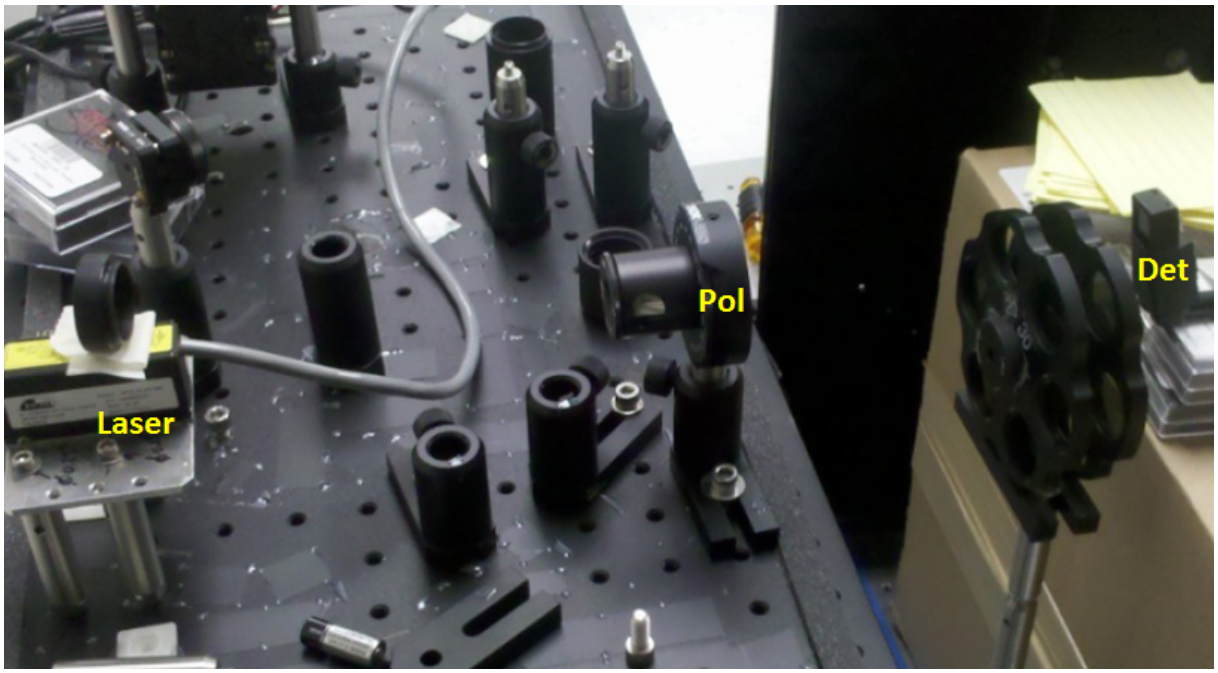

Figure 6.4: Measurement of the Stokes vector exiting the microchip laser.

In similar fashion, each element of the sensor receive path defining $\mathbf{M_{RX}}$ was evaluated for potential polarization modification of the transiting received scattered signal. Figure (6.5) illustrates measurement of the Stokes vector exiting the telescope. A known Stokes vector defined by the output of the laser, beam expander, and Glan Thompson polarizer optical train is input to the telescope. Ten exiting Stokes vectors were measured with the telescope rotated about its optical axis and displaced in the plane orthogonal to the optical axis. The results indicated negligible modification of the transiting laser light.

6.2.3 Detection

Received signals scattered from semitransparent media are collected by dual dynode chain photomultiplier tubes, Hamamatsu model H7422PA-40. PMT detectors are used in the sensor for their relatively low cost, single photon sensitivity, large active apertures, nanosecond FWHM output, and high internal gains ($10^5 - 10^6$). Additionally, the PMT offers low dead time compared to the APD operating in photon counting or Geiger mode, which typically have dead times on the order of 50 nsec even with active quenching circuits. Each PMT operates with a 1 nsec rise time prior to output of a 2.5 nsec FWHM pulse. The detectors operate with known timing jitters of 290 and 270 psec in the parallel and perpendicular channels, respectively. The output of each PMT is input to independent channels of a dual channel constant fraction discriminator, which determines the PMT signal apex independently of the signal pulse height. The CFD operates with an intrinsic timing jitter of 3.2 psec, outputting a TTL-level pulse of 270 nsec duration. Each CFD output pulse is passed to and stored onboard the TDC, operating with a 27 psec bin width, one bin entry per laser firing, and 190 nsec dead time between consecutive registered events. Time-of-flight measurements are performed by an onboard processor, determined by differencing the TDC time tags of the laser fire ("start") event sampled by the fast photodiode and the photon return ("stop") events from each PMT.

Variability in the strength of received signals scattered from surfaces with contrasting **F** matrices, as highlighted in Figure (4.4), mandated the use of a constant fraction discrimination

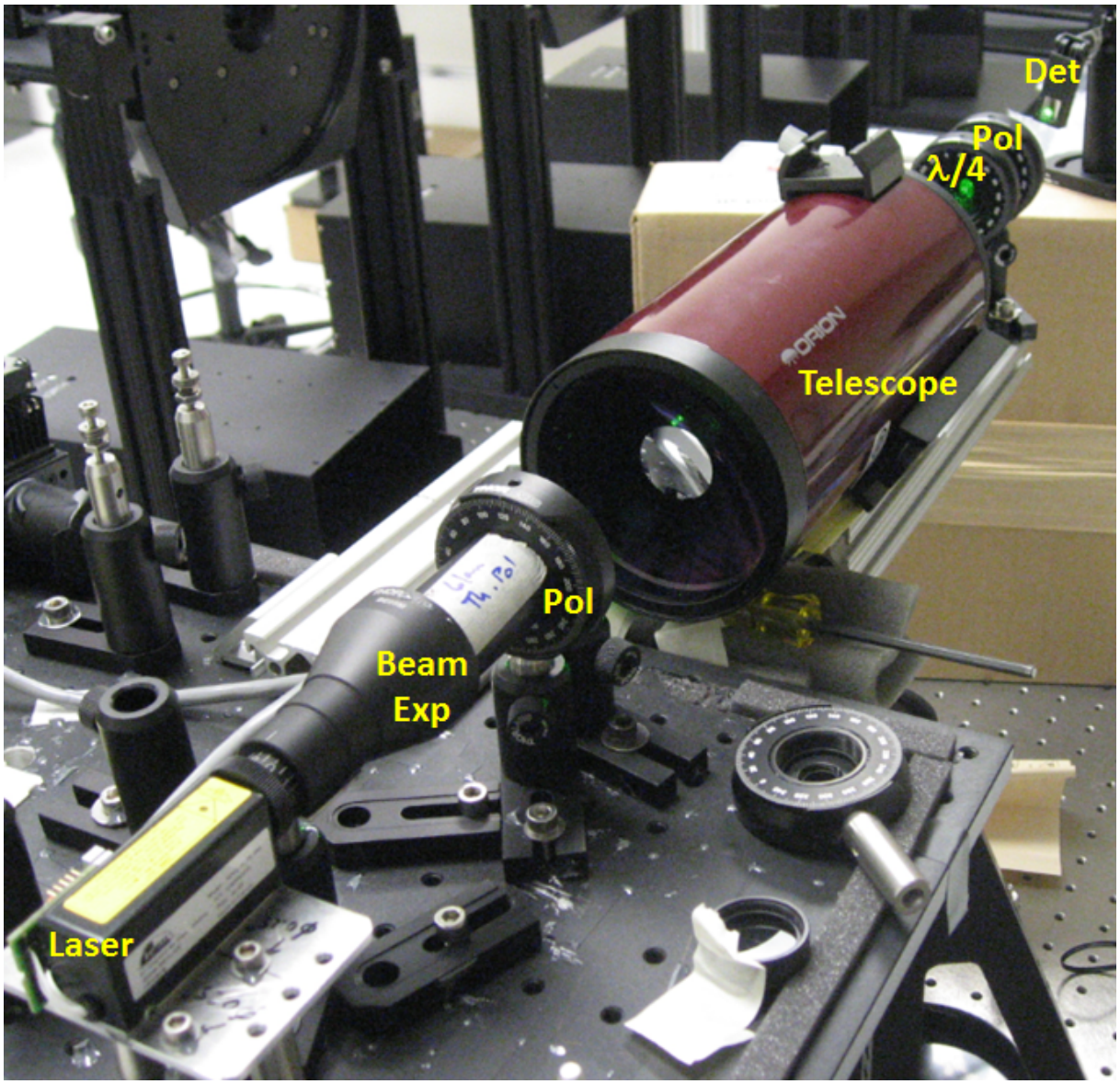

Figure 6.5: Measurement of the Stokes vector exiting the telescope. A known Stokes vector defined by the output of the laser, beam expander, and Glan Thompson polarizer optical train was input to the telescope. Ten exiting Stokes vectors were measured with the telescope is rotated about its optical axis and displaced in the plane orthogonal to the optical axis. The results indicated negligible modification of the transiting laser light.

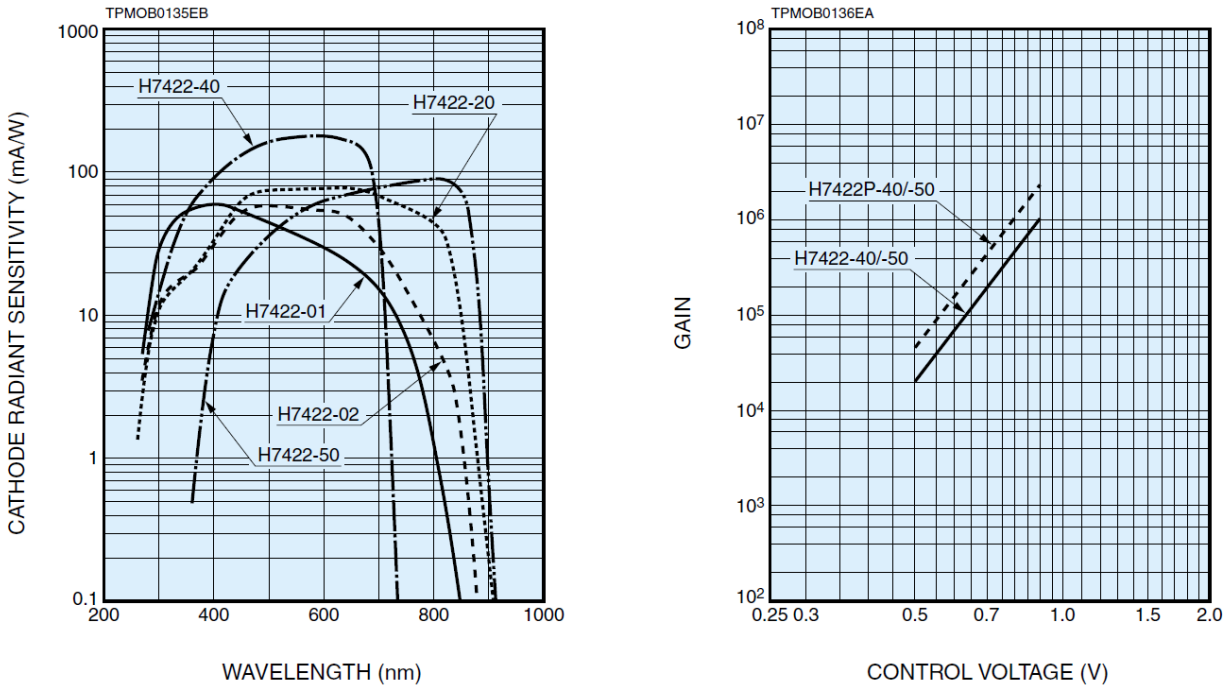

Figure 6.6: Hamamatsu specifications for photomultiplier tube cathode radiant sensitivity as a function of wavelength (left) and gain as a function of control supply voltage (right). The H7422PA-40 series photomultiplier tubes were chosen for their high radiant sensitivity at 532 nm, as well as the $10^5 - 10^6$ gain available at the nominal operational control supply voltage of 0.80 V.

scheme over a more simplistic static threshold in an effort to minimize time walk of the discriminated signals. A block diagram of the CFD circuit is provided in Figure (6.7). Electrical output from each PMT in the parallel and perpendicular detection channels are input to independent channels of the CFD. Each PMT voltage pulse is amplified and split into two components. The component passed through the top portion of the circuit is fed to a comparator that compares the PMT signal to a programmable threshold voltage, set to a level that defines when a useful real signal is arriving. The output of this comparator serves as an enable signal to qualify the output of the bottom section of the CFD. The component passed through the bottom portion of the circuit is split a second time, fractioned and delayed, and input to a second comparator. Providing suitable fractions and delays are chosen for the PMT output characteristics, the delayed signal crosses through the fractioned signal at the same point in time, regardless of the amplitude of the PMT output.

A flip-flop with a delayed clear fixes the pulse width of the 270 nsec TTL-level output. For a 450 psec laser pulse width, 2.5 nsec PMT output pulse width, and 190 nsec TDC dead time between registered events, the 270 nsec CFD output defines the governing pulse width of the lidar sensor. For each PMT output pulse (noise or signal) of sufficient amplitude to enable the CFD, an event is recorded by the TDC and the sensor is subject to a 270 nsec dead time before recovering to record a next event.

"For each PMT output pulse (noise or signal) of sufficient amplitude to enable the CFD, an event is recorded by the TDC and the sensor is subject to a 270 nsec dead time before recovering to record a next event."

A wide FOV camera is mounted on the optical bench and aligned with the sensor transmission path to provide 1 Hz digital imagery of the scene. The combined sensor (including data transfer and processing components) weighs 15 kg and runs off of standard 120 VAC with an average power consumption of 89 W. The sensor is controlled by a single operator and can be readily configured to operate autonomously onboard a UAS provided a suitable processor is chosen for the desired mission profile.

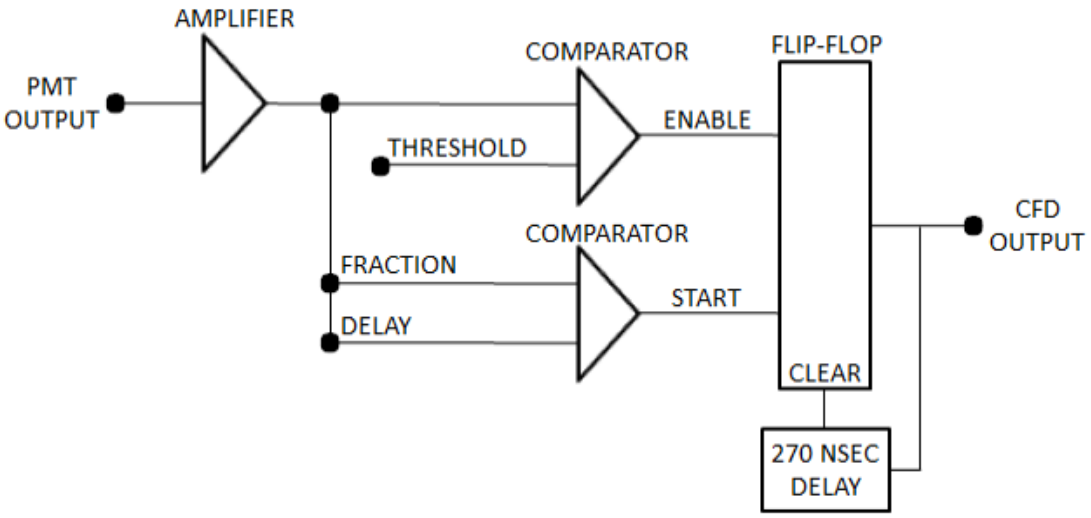

Figure 6.7: Constant fraction discriminator block diagram. Electrical output from each PMT is passed to independent channels of the CFD, which determines the PMT signal apex independently of the signal pulse height. The CFD outputs a TTL-level pulse of 270 nsec width that is passed to and stored onboard the TDC.

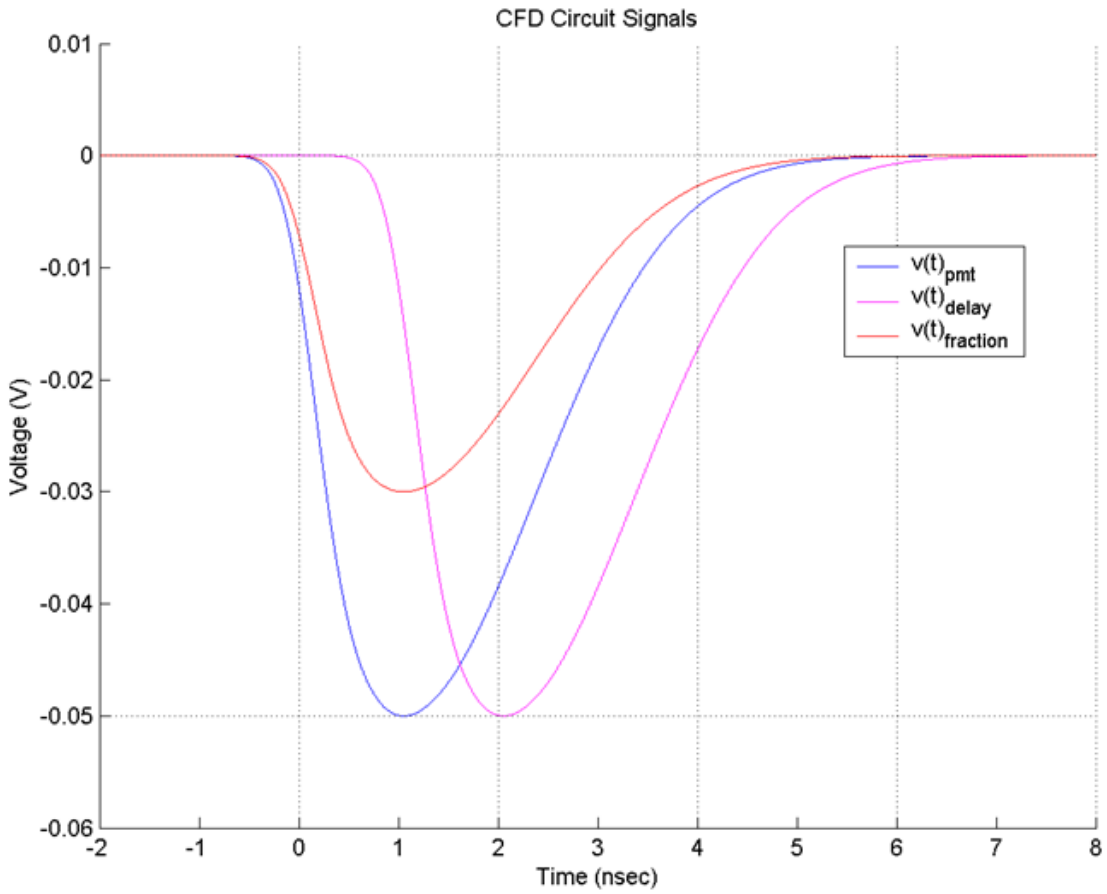

Figure 6.8: Representative signal components of the CFD circuit. Provided a suitable fraction and delay is chosen, the apex of the PMT voltage output will be discriminated at the same point in time regardless of the PMT pulse height.

6.3 Measurements

This section details range-resolved observations acquired with the sensor to demonstrate application of the polarization lidar theory developed in the dissertation research outside of the laboratory environment.

6.3.1 Polarization Indiscriminate Detection

Timing data were acquired with the sensor during reception of signals scattered from the experimental setup of Figure (6.9). An opaque surface was mounted at a known distance d_0 of 5100 cm from the lidar (340 nsec TOF) to simulate the floor of an arbitrary water body. Timing data were initially acquired in the parallel detection channel, as illustrated in Figure (6.10), to replicate the performance of a conventional lidar bathymetry sensor using no polarization discrimination in the receiver. The timing histogram results from the integration of scattered pulses for 4 seconds with at most one entry per timing bin per laser fire at the laser pulse repetition frequency of 14.3 kHz, or 70 μsec interpulse period. The CFD enable threshold voltage, k_{th} in Equations (4.36) and (4.37), was raised above the operational noise level $\overline{N}_b$, resulting in the lack of background counts. The histogram is centered around the 340 nsec TOF and has a 290 psec width dominated by pulse jitter in the parallel channel PMT. For each PMT output pulse of sufficient amplitude to enable the CFD, an event is recorded in the TDC and the lidar is subject to the governing 270 nsec dead time.

Timing data were then acquired with the sensor ranging through a semitransparent glass panel, used to simulate a still water surface, mounted between the lidar and the opaque surface. The glass surface was initially mounted at depth **A** of 4252.5 cm from d_0, corresponding to 847.5 cm from the lidar (56.5 nsec TOF). The TOF flight between signals scattered from the sequential surfaces in this configuration was 283.5 nsec. The lidar discriminates and records returns from the semitransparent surface and is subject to the governing 270 nsec CFD dead time, depicted spatially as d_{CFD} in Figure (6.9). As predicted by the theory presented in Figure (4.12), with the

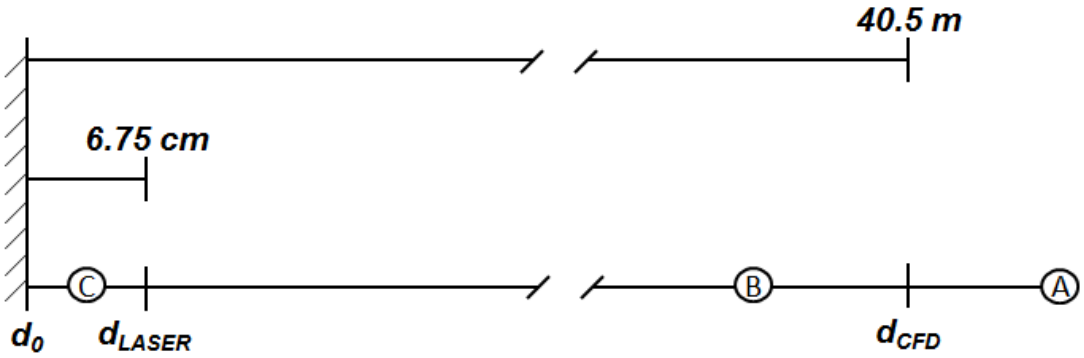

Figure 6.9: (**not to scale**) Diagram of the experimental setup. An opaque target is mounted a distance d_0 from the lidar. A semitransparent target is initially mounted at depth **A** from d_0, larger than the equivalent depth d_{CFD} defined by the 270 nsec CFD dead time. The semitransparent target is relocated to depth **B**, within d_{CFD}. Finally, the semitransparent target is relocated to depth **C**, within the equivalent depth d_{LASER} defined by the 450 psec laser pulse width.

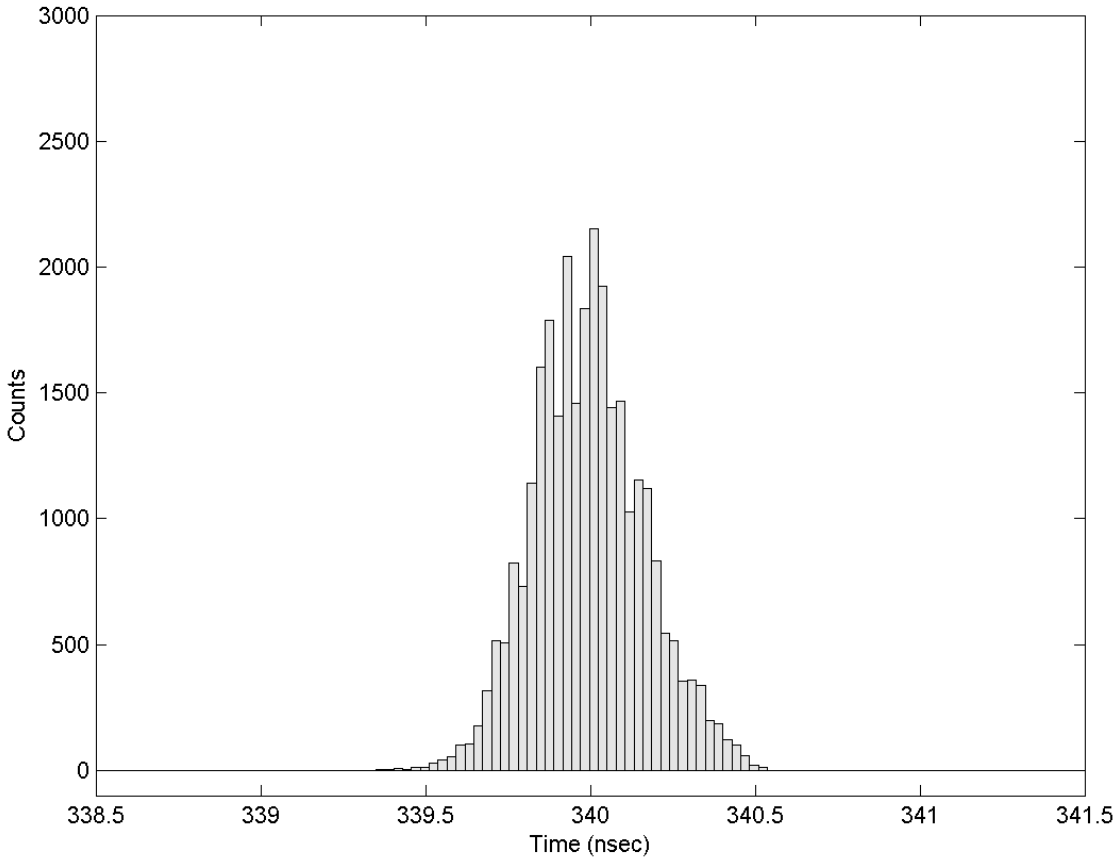

Figure 6.10: Timing histogram generated by the lidar in the parallel detection channel from a single opaque surface over a 4 sec integration period. The TDC produces a histogram with a 27 psec bin width and one bin entry per laser firing. The width of the histogram is dictated by pulse jitter from the PMT.

glass mounted at **A**, the lidar recovers from the dead time to discriminate and record returns from the opaque surface as illustrated in Figure (6.11). The differing histogram amplitudes are related to the variable PMT pulse height distribution generated by backscattered signals from each surface and subsequent probability of discrimination by the CFD.

The semitransparent surface was then translated and mounted at depth **B** of 3651 cm from d_0, corresponding to 1449 cm from the lidar (96.6 nsec TOF). The TOF flight between signals scattered from the sequential surfaces in this configuration was 243.4 nsec. As illustrated in Figure (6.12), the lidar discriminates and records returns from the glass surface. The lidar is unable to recover from the governing 270 nsec dead time, as predicted by the theory presented in Figure (4.13), and no longer records events from the opaque surface.

6.3.1.1 Considerations: Noise

The histograms of Figures (6.10) - (6.12) demonstrate timing data for backscattered signals that generate PMT output amplitudes greater than the CFD threshold voltage k_{th}, configured above the operational noise level $\overline{N}_b$ to ensure the TDC records only desired signal returns $\overline{N}_s$. The limitation to the range measurement imposed by the governing dead time is reduced in the case where signal and noise (e.g., solar background, detector dark counts) events are of similar amplitude and/or the CFD threshold k_{th} is lowered to increase the false alarm rate. In this case, any PMT output pulse of sufficient amplitude to enable the CFD will subject the lidar to the governing 270 nsec dead time. For deterministic signal returns from a media surface, the dead time is initiated within the pulse jitter of the PMT. Due to the random nature of noise events, however, the 270 nsec dead time is initiated randomly.

As predicted by the theory presented in Figure (4.14), if the sensor is permitted sufficient integration time, the random occurrence of the governing CFD dead time permits the TDC to record returns from sequential surfaces with differential TOF less than 270 nsec. This occurrence is demonstrated in Figure (6.13). Here, the glass surface remains mounted at depth **B**. The CFD threshold voltage is lowered to enable registration of noise events. Due to the random nature of

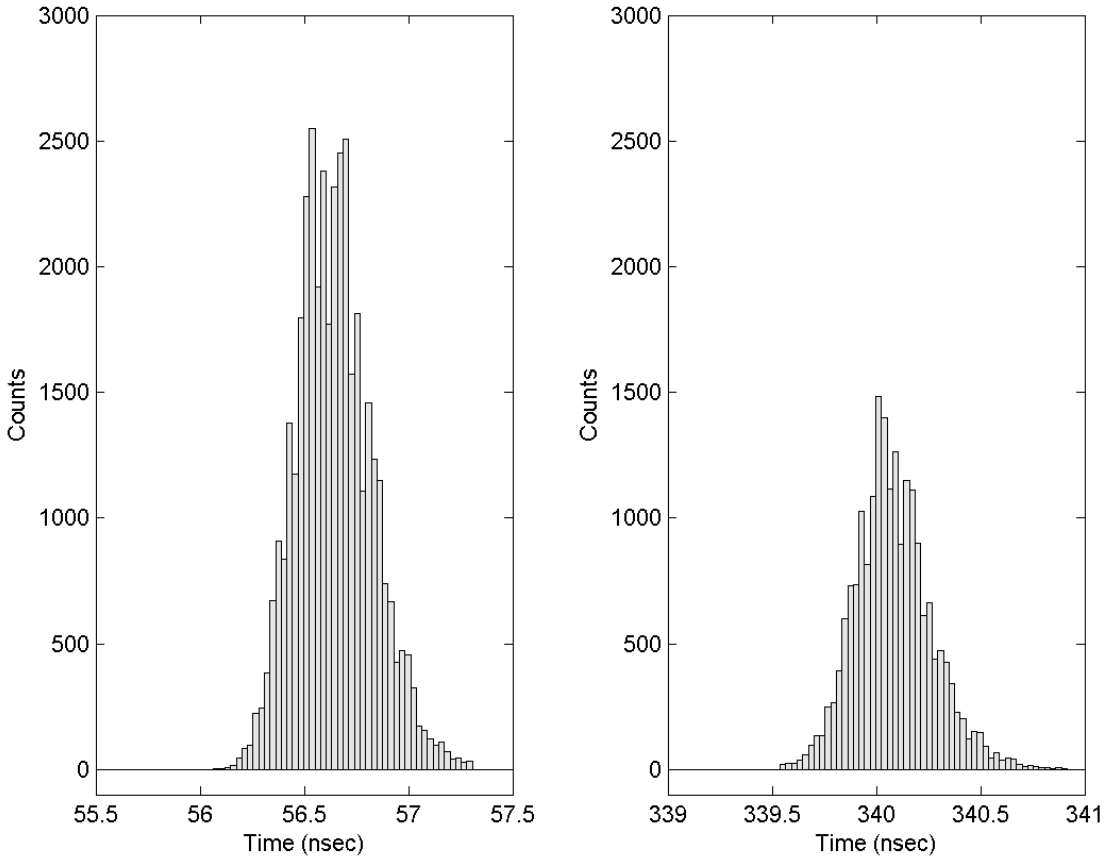

Figure 6.11: Timing histograms simultaneously acquired from an opaque surface (right) mounted at 4252.5 cm depth from a semitransparent surface (left) over a 4 sec integration period.

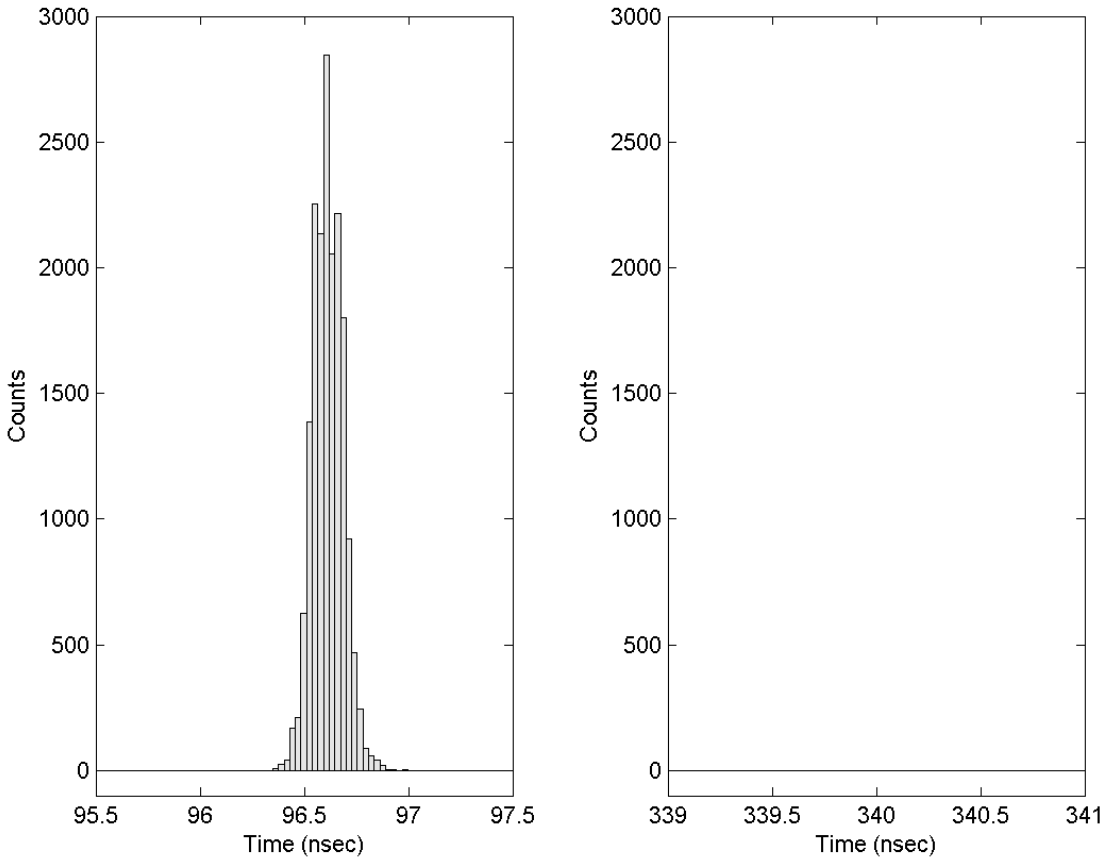

Figure 6.12: Timing histogram acquired from a semitransparent surface (left) over a 4 sec integration period. The opaque surface is mounted at 3651 cm depth, within the governing 270 nsec dead time of the lidar. As a result, no timing histogram is acquired from the opaque surface (right).

the noise events, the governing CFD dead time is now randomly distributed. This effect periodically prohibits the instrument from recording events from the semitransparent surface, permitting discrimination of returns from the opaque surface. As the lidar integrates for an extended period, timing histograms are generated from both surfaces, and depths less than those dictated by the dead time of the CFD can be resolved.

Severe noise levels can statistically render the instrument blind to both surfaces and therefore must be characterized for a given measurement environment in order to configure the CFD enable threshold appropriately. Additional attention must be paid to the receiver field of view and spectral filter in an effort to minimize contribution to the detected events from out of band wavelengths.

6.3.1.2 Considerations: Laser/Detector Pulse Width

Chapter 4.3.4 detailed the benefits that arise for the depth measurement by introducing the randomness of discriminated noise events, which provide an approach to mitigate the governing electrical dead time of the CFD for polarization indiscriminate detection at the expense of increased integration time. However, limitation to the range measurement remains for sequential media surfaces with separation distance less than the spatial width of the combined laser/detector pulse. In this optical regime, returns from sequential surfaces are contained within the envelope of the laser/detector pulse width. For the lidar described in this subsection, in the event sequential surface returns are contained within the envelope of the laser/detector pulse, the CFD will determine the signal apex of the resulting PMT output and generate a single TTL output pulse to be recorded by the TDC. While discrimination of noise events provides a means to reduce the severity of the governing electrical CFD dead time, operation in the shallow regime remains limited in this prescribed configuration for returns enveloped by the convolved pulse width of the laser and detector.

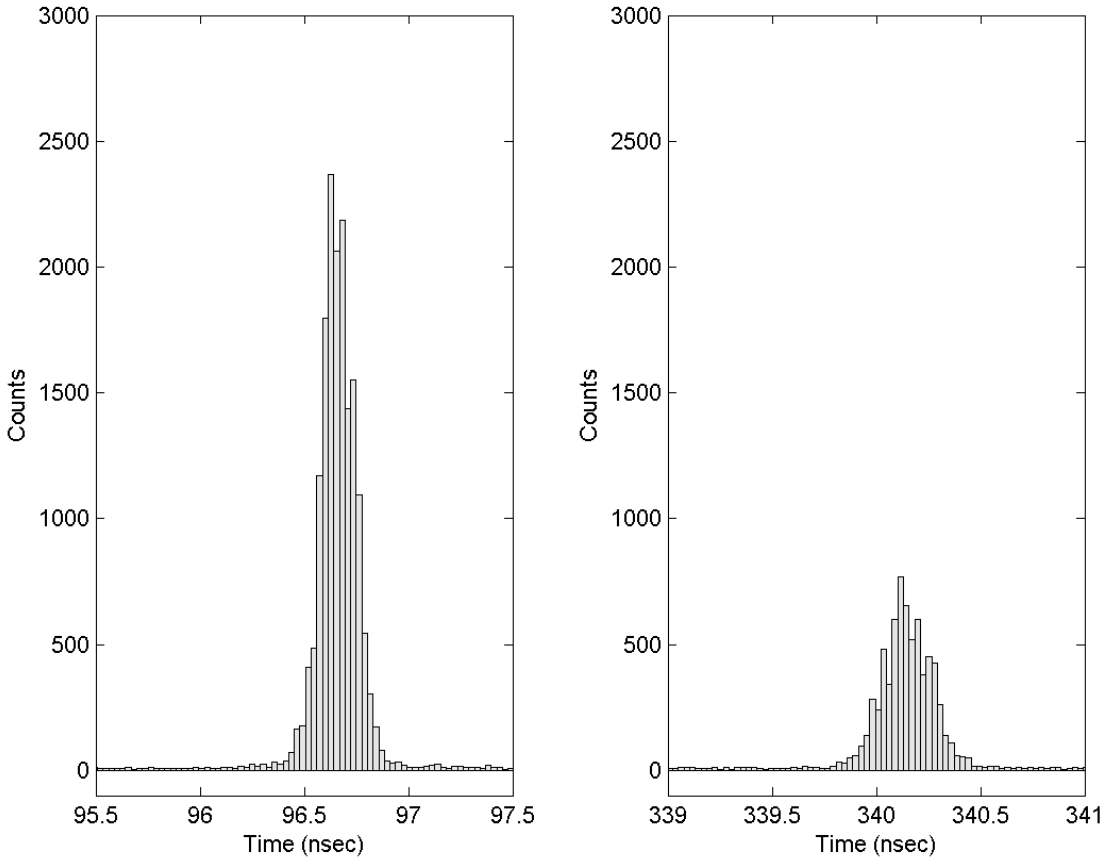

Figure 6.13: Timing histograms simultaneously acquired from an opaque surface (right) mounted at 3651 cm depth from a semitransparent surface (left) over a 20 sec integration period. The CFD voltage threshold is lowered to discriminate noise events, generating a randomly occurring 270 nsec dead time.

6.3.2 Polarization Discriminate Detection

The prototype polarization lidar described in this chapter utilizes dual detection channels and optical polarization discrimination to overcome the governing limit on time responsivity imposed by the laser/detector pulse width. To demonstrate the capacity of the dual detection channel approach to achieve high-resolution ranging through semitransparent media, the measurements of Section 6.3.1 are revisited.

6.3.2.1 Overcoming the Limitation Imposed by CFD Pulse Width

To demonstrate the capability of the prototype lidar to measure depth between sequential surfaces within the governing CFD pulse width, additional timing histograms were acquired using the setup of Figure (6.12). Here, the glass surface remained mounted at depth **B** from d_0. Unlike the single detection channel measurement, however, timing histograms were simultaneously integrated by the parallel and perpendicular detection channels in the receiver. When incident upon the glass surface, a portion of the transmitted linearly polarized light reflects back to the receiver in a nearly preserved orientation and degree of polarization. The result is linearly polarized light incident upon and reflected by the Glan Taylor polarizer to the PMT for detection of the scattered parallel polarized signal. The CFD in the parallel detection channel discriminates the PMT voltage output and is subject to the governing 270 nsec dead time. Energy scattered from the surface into the perpendicularly polarized plane is of insufficient intensity to enable the CFD in the perpendicular detection channel.

A portion of the laser light transmits through the semitransparent glass surface and incidents the opaque surface. This light depolarizes upon reflection due to the rough topography of the surface. Returning to the lidar, half of the scattered light is passed through, and half is reflected, by the Glan Taylor polarizer to the PMT in each detection channel. The CFD in the perpendicular detection channel discriminates the PMT voltage output and is subject to the 270 nsec dead time. Reception of scattered light from the polarization preserving glass surface previously enabled the

CFD in the parallel channel; therefore, no event is recorded from the depolarizing surface in the parallel detection channel.

This capability to overcome the limitation on range measurement imposed by the governing CFD dead time is illustrated in Figure (6.14). By discriminating the polarization orientation of scattered signals for each transmitted laser pulse, the lidar simultaneously acquires timing histograms from the sequential surfaces. This translates the shallow media range measurement into two surface altimetry measurements, where target selection is dictated by the propensity of the surface to decouple energy into the perpendicular polarization plane. The polarization preserving surface is effectively removed from the measurement in the perpendicular detection channel, enabling the depolarizing surface signals to be isolated for analysis. Thus an additional benefit of the polarization lidar approach is the capacity of the sensor to overcome the governing electrical dead time via discrimination of optical signals, eliminating the lengthy integration time required by conventional sensors to mitigate the dead time limitation through discrimination of the randomly occurring noise events.

6.3.2.2 Overcoming the Limitation Imposed by Laser/Detector Pulse Width

To demonstrate the capability of the lidar to measure depth between sequential surfaces enveloped by the laser/detector pulse width, timing data were acquired during reception of signals scattered from the glass surface mounted at depth **C** of 2.4 cm from d_0 as illustrated in Figure (6.15). Note here that the glass panel is physically measured to 0.95 cm thickness, placing the front surface of the glass 3.35 cm from the opaque surface. With a laser of 450 psec pulse width (13.5 cm spatial equivalent), scattered optical signals from the sequential surfaces overlap within the envelope of the laser pulse, depicted spatially as d_{LASER} in Figure (6.9). Conventional lidar sensors, performing the range measurement with a polarization indiscriminate detection approach, are subject to this intrapulse ambiguity, even in the presence of noise.

Two measurements were conducted with the glass mounted at **C**. First, timing histograms from the opaque surface were simultaneously integrated over 30 sec in the parallel and perpendicular

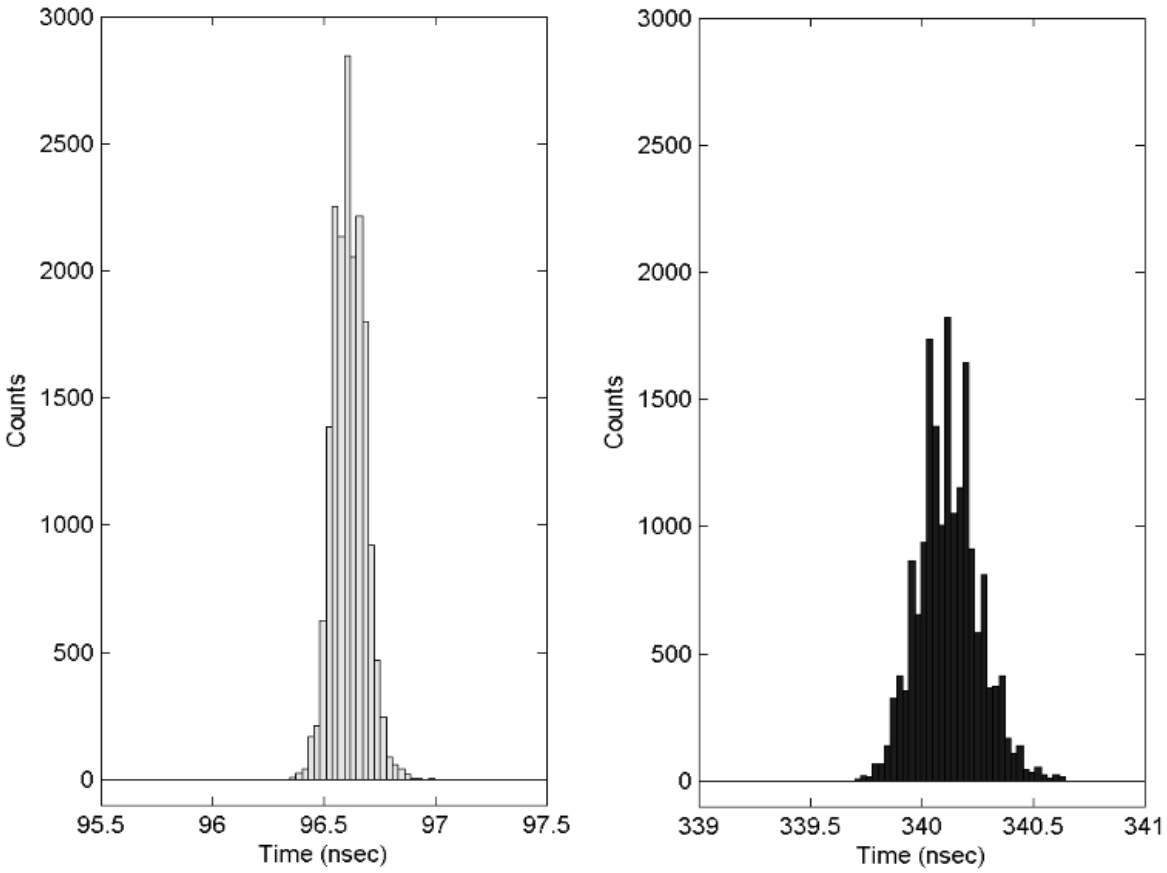

Figure 6.14: Timing histograms simultaneously acquired from an opaque surface (right) mounted at 3651 cm depth from a semitransparent surface (left) over a 4 sec integration period. Data at left are acquired in the parallel detection channel; at right in the perpendicular channel.

detection channels in the absence of the glass surface, providing a baseline range measurement to the depolarizing surface. The semitransparent glass surface was then reinserted into the optical path and timing histograms were integrated in both channels to demonstrate the capability of the lidar to measure the depth between sequential surfaces at sub-laser pulse width resolution.

> ***"Conventional lidar sensors, performing the range measurement with a polarization indiscriminate detection approach, are subject to this intrapulse ambiguity, even in the presence of noise."***

Figure (6.16) illustrates the envelope of the timing histograms, the width of which corresponds to the respective jitter of each PMT. To remove discrepancies in integrated counts per bin between channels and highlight the timing resolution of the lidar, the histograms were integrated over 30 sec and normalized to their respective maximum count value. Range to the opaque surface registers 5409.6 cm (360.64 nsec TOF) in both detection channels, measured at the apex of the timing histograms. Inserting the semitransparent surface into the optical path physically reduces the range to the first surface by a distance l of 3.35 cm. As a result, it is expected that the peak of the semitransparent surface timing histogram t_{semi} will advance in time to

$$t_{semi} = 360.64 - \frac{2l}{c} = 360.64 - \frac{2\,(0.0335)}{c} = 360.42nsec \tag{6.8}$$

which agrees with the TDC measurement of 5406.8 cm (360.45 nsec TOF) to within the precision of a ± 0.4 cm bin width.

Contrasting the setup between experiments, light scattered from the opaque surface is subject to a transit distance l of 0.95 cm of glass compared to 0.95 cm of air. Given the refractive index n = 1.7 of the glass, inserting the panel into the optical path is expected to delay the opaque surface return t_{opaq} in time by

$$t_{opaq} = \frac{2nl}{c} - \frac{2l}{c} = \frac{2\,(1.7)\,(0.0095)}{c} - \frac{2\,(0.0095)}{c} = 0.044nsec \tag{6.9}$$

due solely to the change in n from air to glass over the $2l$ roundtrip distance. The expected

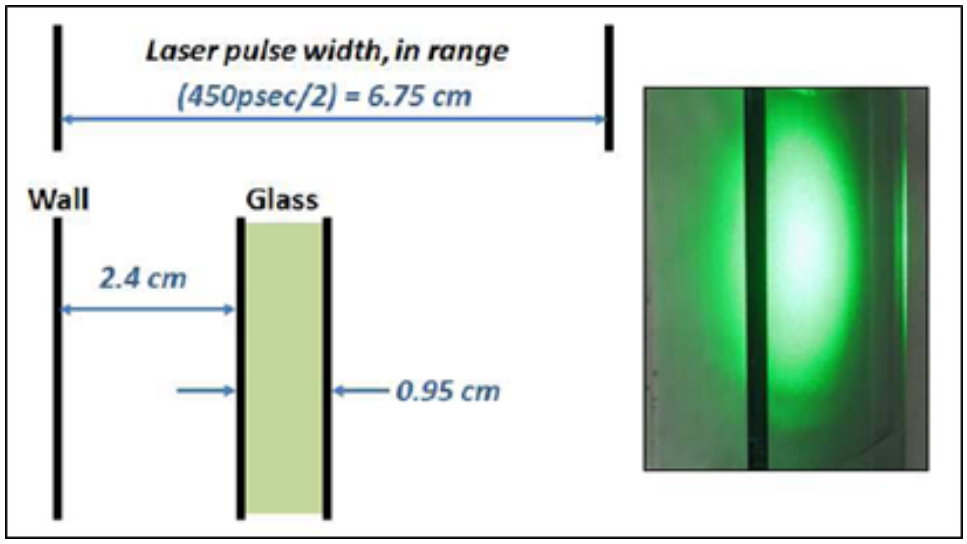

Figure 6.15: Measurement configuration in which the glass surface is mounted at depth of 2.4 cm from the wall. The 450 psec pulse width of the laser corresponds to 6.75 cm in range. Utilizing the INPHAMIS approach, timing histograms were integrated in the parallel and perpendicular detection channels to demonstrate the capability of the sensor to measure the depth between sequential surfaces at sub-laser pulse width resolution.

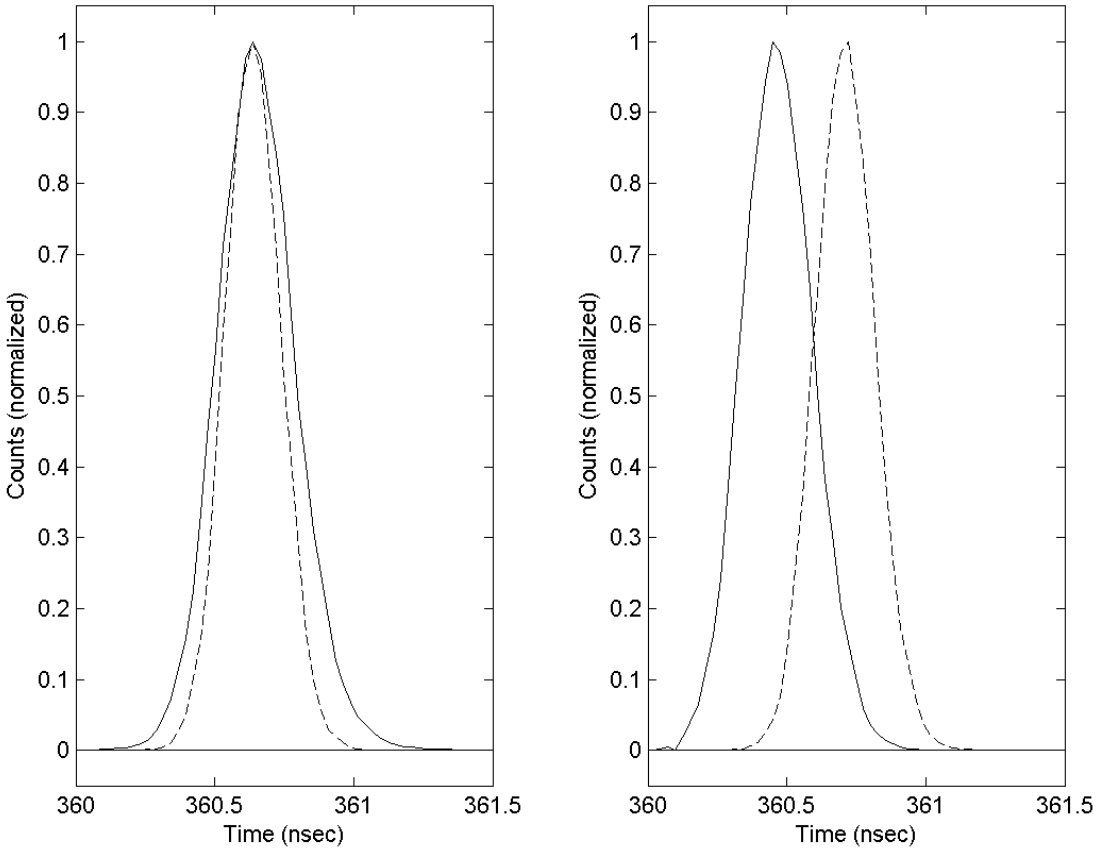

Figure 6.16: Envelope of normalized timing histograms simultaneously acquired over a 30 sec integration period for the parallel (solid) and perpendicular (dashed) detection channels, from an opaque surface (left) and semitransparent surface mounted between the lidar and opaque surface (right).

apparent shift to 5410.2 cm (360.68 nsec TOF) agrees closely with the range measurement of 5410.8 cm (360.72 nsec TOF) to within ± 0.4 cm.

To more accurately replicate the operational environment of a lidar bathymetry sensor, the experiment presented in this subsection was repeated with the sensor pointed in the nadir direction, ranging to a container filled with water as depicted in Figure (6.17). A plastic substrate was submerged under water, the surface of which was roughened to simulate depolarizing ice. The sensor was mounted external to a window hatch installed on the fourth floor of the building, at a known range of approximately 12 meters from the ground upon which the container was mounted. Timing histograms were integrated in the parallel and perpendicular detection channels. Differencing the apex of each timing histogram resulted in a measured delay of 189 psec, corresponding to a depth of

$$d = \frac{(3e^{8})(189e^{-12})}{2(1.33)} = 2.1cm \tag{6.10}$$

compared to the physically measured depth of 2.0 cm, which possesses a ±1 mm uncertainty, within a single TDC bin width.

The dual detection channel approach and results illustrate several unique aspects of the polarization technique. First, the technique enables sub-laser/detector pulse width depth resolution that is limited only by the timing resolution of the TDC. In this setup, the precision of the measurement is established by the 27 psec bin resolution of the TDC. Second, the technique removes the dependency on short laser pulses and fast detectors, allowing for increased flexibility in laser selection criteria and enabling more affordable and less complex lidar components to be employed while still achieving significant improvements in shallow water depth measurements.

Both detection channels were calibrated in the time domain to account for differences in optical and electrical path lengths. Due to the physical setup of the instrument, the optical path length between the Glan Taylor polarizer and the detector face in the perpendicular channel is 9.5 cm longer than the parallel channel. Additional timing offsets exist due to the variability of cabling used to connect the PMT, CFD, and TDC electrical paths in each channel. Timing calibration

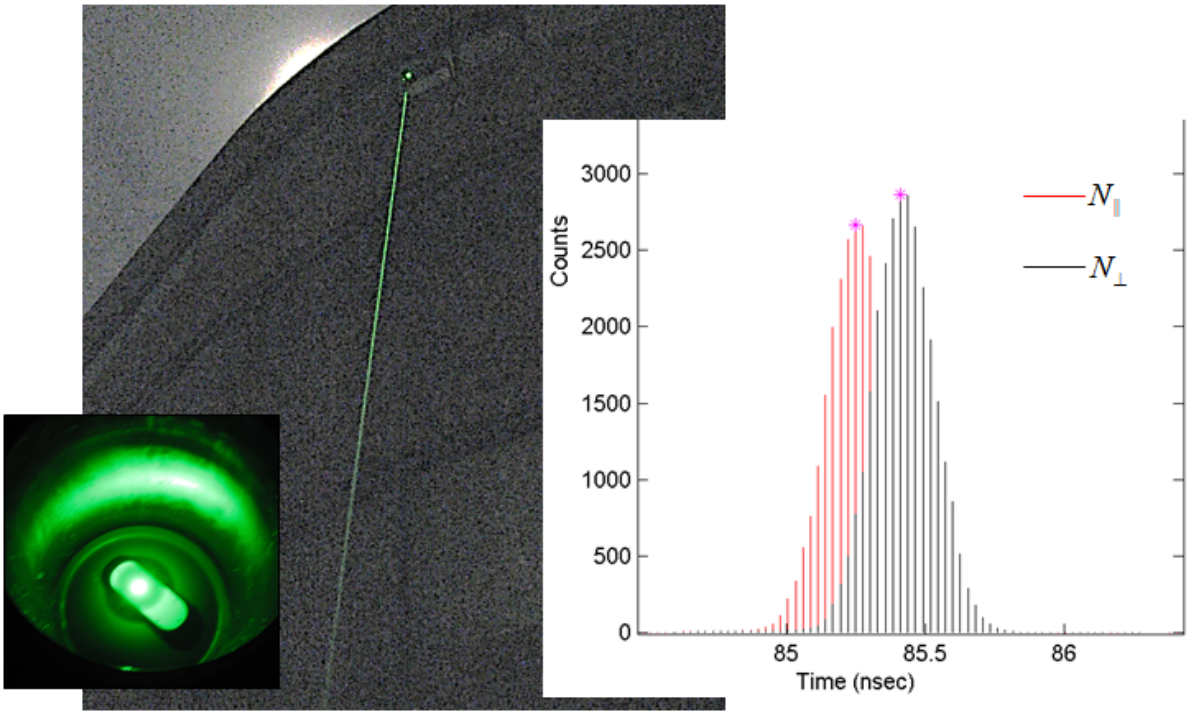

Figure 6.17: Experimental configuration for the water depth measurement. The sensor was mounted to point vertically downward from an open hatch, ranging to a container of water with a submerged plastic substrate (left), the surface of which was roughened to simulate depolarizing ice. Timing histograms were integrated in the parallel and perpendicular detection channels (right), producing a water depth measurement at sub-laser pulse width resolution.

was accomplished by ranging to the depolarizing opaque surface in the absence of the glass panel. Timing histograms were acquired over a 30 sec integration period in the parallel and perpendicular channels, and normalized to their maximum respective count value. The histogram acquired in the perpendicular channel was shifted forward in time 56 TDC bins (1.512 nsec) to match the peak bin to that of the parallel channel, as demonstrated at left in Figure (6.16). The resulting error in range measurements between detection channels is defined as one half of a TDC bin width, or 4 mm in air.

6.3.2.3 Linear Depolarization Estimate

The prototype polarization lidar described in this chapter overcomes traditional governing pulse width limitations through simultaneous detection of signals scattered in the polarization planes parallel and perpendicular to the transmitted laser light. In addition to timing information, the detected signals also contain polarization information about the scattering properties of the semitransparent media surface. This information can be evaluated to differentiate between surface types, such as water and ice [118], by measuring the propensity of the surface to depolarize incident light into the perpendicular polarization plane.

Linear depolarization may be characterized by ratioing the parallel and perpendicular polarization components of the backscattered light. The resulting linear depolarization ratio is defined as [51]

$$\delta = \frac{N_{\perp}}{N_{\parallel}} \tag{6.11}$$

where $N_{\perp}$ and $N_{\parallel}$ are the components of the detected signal polarized perpendicular and parallel to the transmitted beam, respectively. Ratioing the integrated timing histograms from a single surface in both detection channels leads to the generation of a depolarization ratio δ for the surface.

The expectation of a weak perpendicularly polarized signal from the bottom surface was a driving requirement for the optical layout of the prototype lidar. Consequently the optical design of the system was optimized for maximum SNR of the perpendicular detection channel. Providing an accurate measurement of the surface depolarization ratio requires calibration of the lidar, including

a parameterization of gain offsets induced by the Glan-Taylor polarizing beamsplitter, PMT detectors, and cross talk between the two receiver channels due to receiver and transmitter misalignment in polarization. Hayman [66] describes a generalized approach to calibrate a lidar system for depolarization estimates, particularly when significant optical retardance is present. Building upon this work, the prototype lidar has been designed with minimal reflecting elements in an effort to minimize optical retardance, and the methods of Alvarez [5, 70] are applied to the calibration. In this case, the digitized signals $\vec{Q}$ stored in the TDC are proportional to the observed photon counts at the detector faces, $\vec{N}$. Here,

$$\vec{Q} = G\vec{N} \tag{6.12}$$

where G is a constant and accounts for the electro-optic gain offset between receiver channels, including PMT quantum efficiencies, amplifier gains, and line losses through the PMT, CFD, and TDC electrical paths. Misalignment between the transmitter and receiver polarization planes by an angle θ introduces a degree of polarization cross talk into the measured depolarization ratio. In this condition, a fraction of the parallel signal is leaked into the perpendicular channel, or vice versa. Without properly calibrating the lidar, these effects contaminate the measurements from which the depolarization ratio δ is derived.

The range-resolved polarization ratio m observed by the lidar is a function of the gain ratio G, the misalignment angle θ, and the depolarization ratio δ of the scattering surface. The observed ratio takes the form

$$m\left(r\right) = G\left[\frac{\delta\left(r\right) + tan^2\left(2\theta\right)}{1 + \delta\left(r\right) tan^2\left(2\theta\right)}\right] \tag{6.13}$$

To calibrate the lidar, a halfwave plate was inserted into the transmit path immediately following the Risley prisms, and timing histograms were integrated from the target surface over a sequence of controlled halfwave plate calibration angles ϕ_j. For each timing histogram acquired at each calibration angle, the effective offset angle is the sum of the misalignment angle θ between the transmit and receive planes and the calibration angle ϕ. Acquiring timing histograms for three or more halfwave plate calibration angles generates a data set with controlled amounts of polarization

cross talk between detection channels. For the jth calibration angle, ϕ_j, the range-resolved observed polarization ratio is now defined as

$$m_j(r) = G\left[\frac{\delta(r) + tan^2[2(\theta + \phi_j)]}{1 + \delta(r)\, tan^2[2(\theta + \phi_j)]}\right] \tag{6.14}$$

where $m_j(r)$ and ϕ_j are measured and $\delta(r)$, G, and θ are evaluated during the calibration process.

As illustrated in Figure (6.18), timing histograms were integrated in the parallel and perpendicular detection channels for signals scattered from the opaque surface of Figure (6.9) for calibration angles $\phi_j = 0°, 10°, \ldots, 90°$, as well as $\phi_j = 45°$ for reference. Observed polarization ratios m_j were generated for each calibration angle ϕ_j by summing the histogram counts in the parallel and perpendicular detection channels and taking their ratio. Evaluating Eq. (6.14) via the observed ratios and a nonlinear least squares algorithm resulted in values of $G = 1.67$ and $\theta = 2.53°$ for the systematic gain and misalignment angle of the lidar, and a $\delta = 0.52$ of the opaque surface.

Thus, an added benefit of the polarization technique beyond improved ranging through semitransparent media is the ability to characterize the depolarization ratio of the scattering surface. This can be used to classify differing bounding surfaces of semitransparent media, owing to their relative roughness and propensity to decouple the incident polarized signal [37]. For example, the δ of sand and still water, typical bathymetric surfaces, were measured with the sensor to 0.55 and 0.01, respectively, using Eq. (6.13) and the systematic values of G and θ. In addition to providing depth measurements of shallow coastal waters, the approach can therefore be used to identify land-water transitions and provide an estimate of relative surface water roughness due to wave activity caused by surface winds.

To demonstrate the capacity of the prototype lidar to classify differing surfaces based on their measured depolarization ratio, the experiment presented in this subsection was repeated with the sensor pointed horizontally, ranging to a neighboring building at known range of approximately 245 m. As depicted in Figure (6.19), timing histograms were integrated in the parallel and perpendicular detection channels with the transmitted laser beam illuminating various differing surfaces of the building. Figure (6.19a) presents timing data acquired with the sensor ranging to a 2nd floor

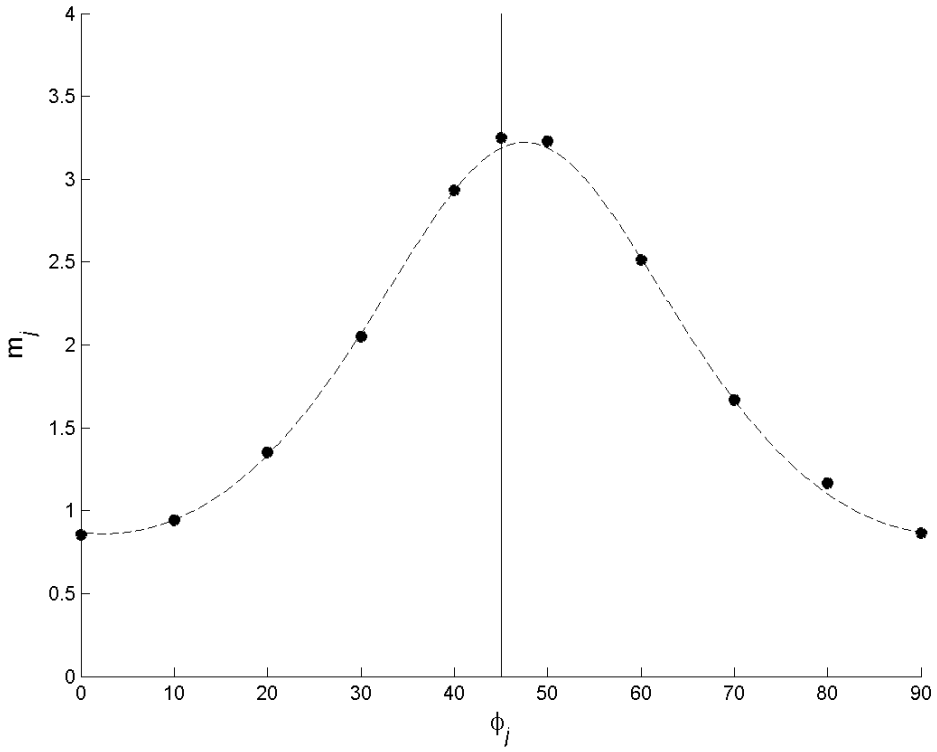

Figure 6.18: Observed depolarization ratio m_j versus halfwave plate calibration angle ϕ_j. Point data were obtained by taking the sum and ratio of timing histograms in the parallel and perpendicular detection channels for $\phi_j = 0°, 10°, \ldots, 90°$. Data were also acquired for $\phi_j = 45°$ for reference. A nonlinear least squares analysis generated values of $G = 1.67$, $\delta = 0.52$, and $\theta = 2.53°$.

window to mimic a smooth water surface; Figure (6.19b) presents timing data acquired from a brick siding to mimic a depolarizing ice bottom. The counts in each channel are integrated during the range window denoted by the vertical dashed lines and ratioed, accounting for the timing and gain offsets described in this subsection.

The results of the range experiment are plotted together in Figure (6.20). Here, the variable depolarization ratio generated by differing surfaces is evident. Polarization-maintaining surfaces such as the windows produce low depolarization ratios ($\delta < 1$) while depolarizing surfaces are distinguished by their variable propensity to decouple the polarized light transmitted by the sensor. Recalling the supraglacial melt lake from Figure (2.8), the experiment is extrapolated to simulate performance of the sensor operating over the GIS. Polarization maintaining surfaces such as the air/water interface will tend to preserve the incident laser polarization, while ice will tend to depolarize the laser light. Evaluation of the measured depolarization ratios during flight operations may aid in classification of ice-water transitions along the perimeter of melt lakes, as well as differing ice surfaces along the ice sheet.

6.4 Conclusions

The experiments and timing data presented in this chapter demonstrate elimination of conventional governing pulse width limitations through exploitation of the variability between the polarization orientation of signals scattered from differing surfaces. The 2.5 nsec PMT pulse width of the prototype sensor presented here limits the conventional, single detection channel approach to a shallow depth measurement between sequential surfaces to tens of cm, even in the presence of randomly initiated noise events. However, by isolating detection of intrapulse surface and bottom returns through polarization discrimination in the lidar receiver, the dual surface depth measurement is transformed into two single surface range-resolved measurements, each now limited only by the 27 psec resolution of the TDC.

As demonstrated, performance of the polarization lidar is optimized through design and operation within the Stokes Vector Lidar Equation. Without proper identification of the polarization

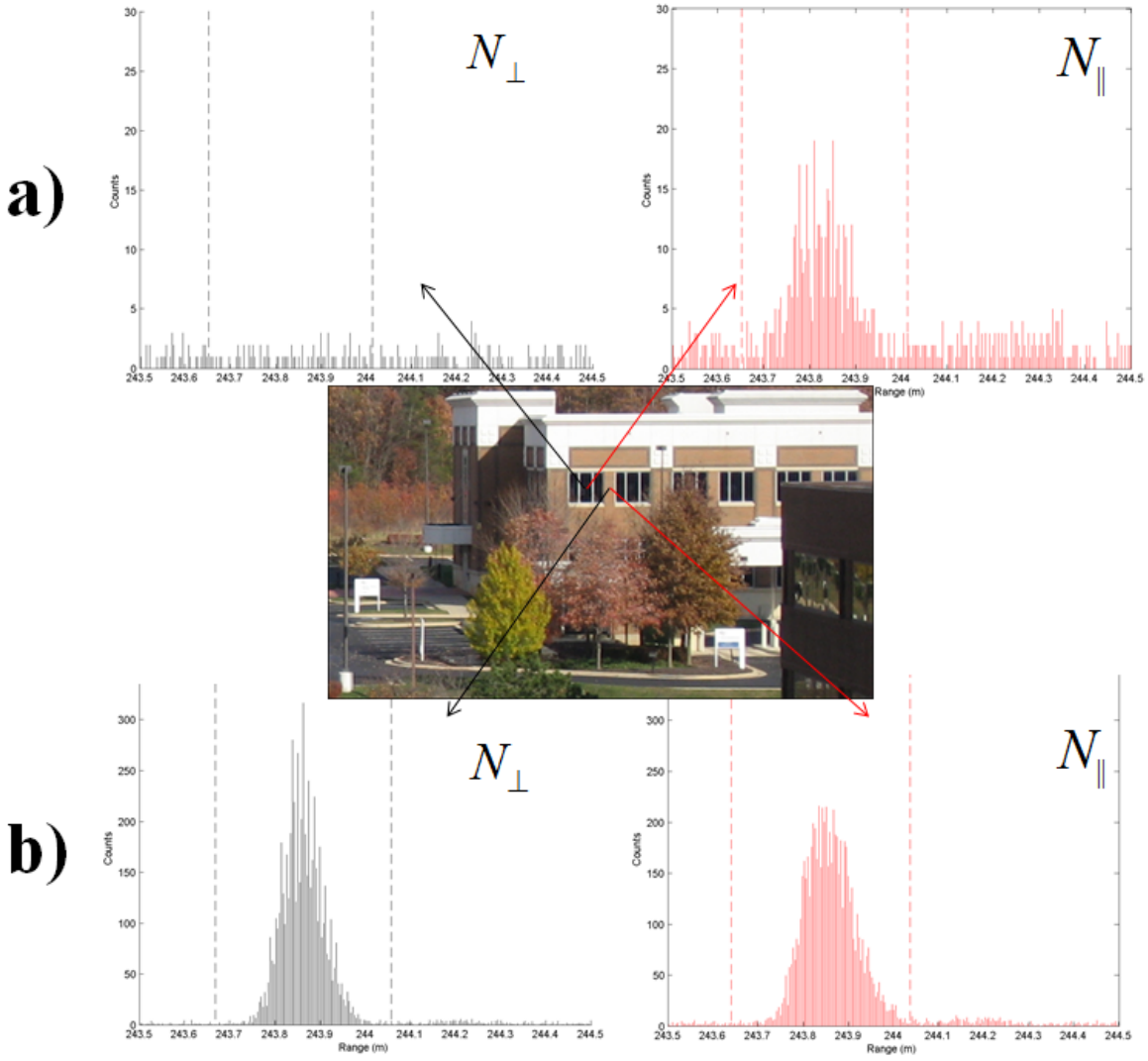

Figure 6.19: Timing histograms integrated in the parallel and perpendicular detection channels for differing surfaces of the building. Integrating and ratioing the counts during the interval defined by the vertical dashed lines permits generation of a depolarization ratio which can be used to classify differing surfaces based on their propensity to decouple the incident laser signal.

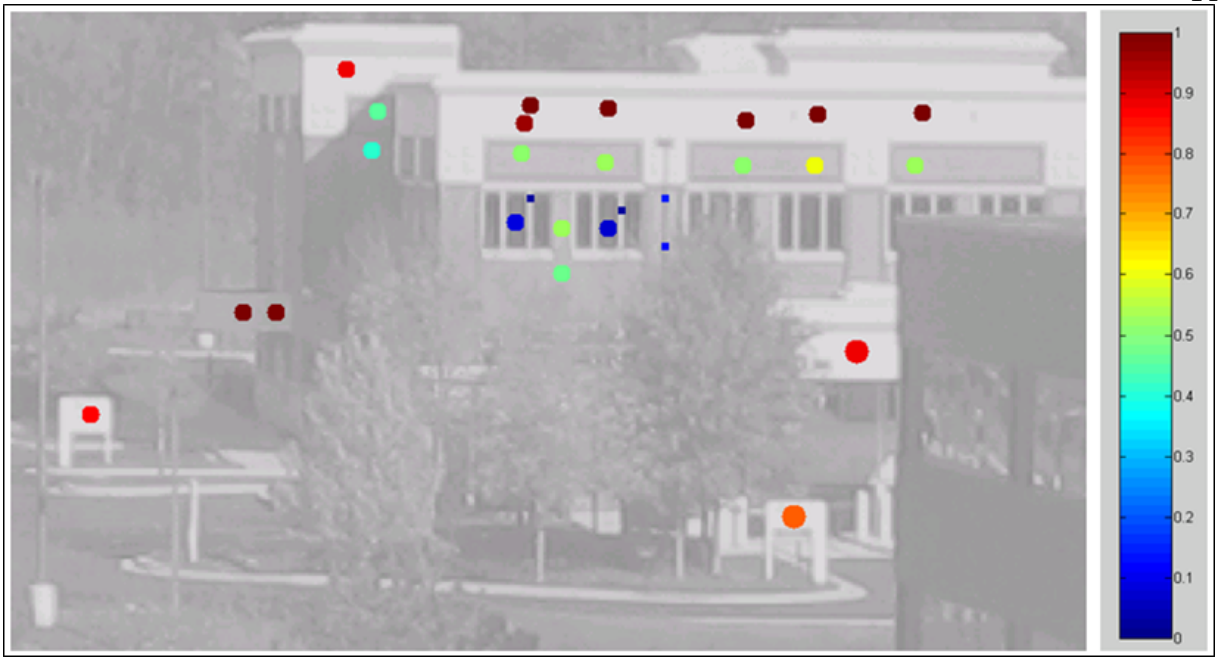

Figure 6.20: Plot of the depolarization ratio for each surface illuminated during the experiment. Polarization maintaining surfaces such as the 2nd floor windows produce low depolarization ratios ($\delta < 1$) while depolarizing surfaces are distinguished by their variable δ values.

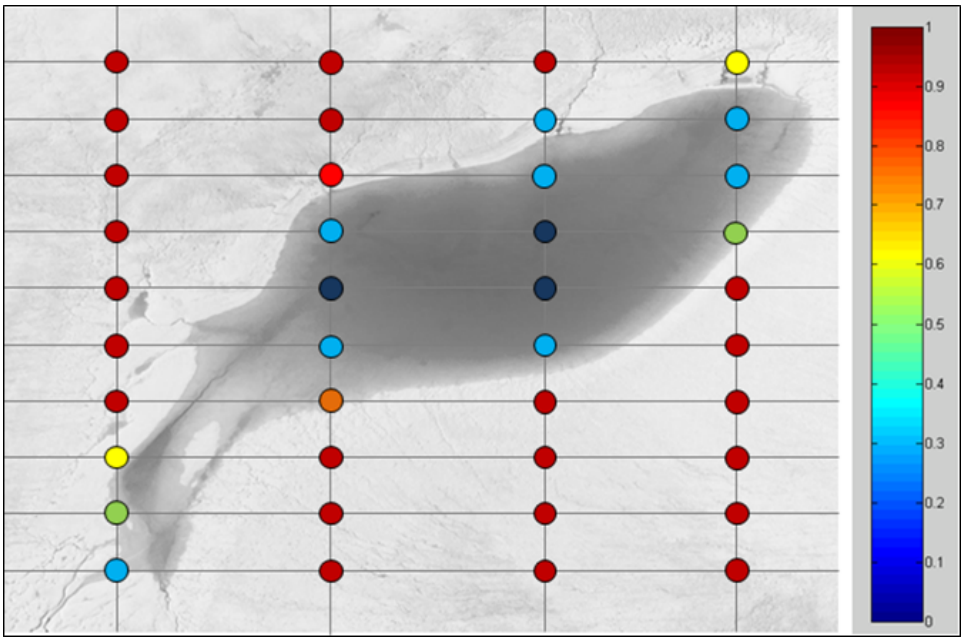

Figure 6.21: Theoretical depolarization ratio data acquired during flight of the sensor onboard a UAS over the supraglacial melt lake from Figure (2.8). Evaluation of the measured depolarization ratios during flight operations may aid in classification of water/ice boundaries as well as differing ice surfaces.

performance characteristics of the lidar sensor, including each element defining $\mathbf{M_{TX}}$ and $\mathbf{M_{RX}}$ as well as the scattering matrix $\mathbf{F}$ under interrogation, the acquired depolarization data is only indicative of a change in polarization and does not adequately explain how the polarization orientation changed. Specific applications of the polarization approach, such as INPHAMIS, require the SVLE approach in order to properly configure the sensor and prevent sensor-induced contamination of first surface scatter.

The ability of the sensor to range to sequential surfaces in the shallow regime requires transmission of linearly polarized light to a polarization preserving, semitransparent first surface followed by a depolarizing second surface. Instrument performance can be limited by the scattering matrix $\mathbf{F}$ of the surfaces. If the $\mathbf{F}$ of the first surface decouples sufficient energy into the perpendicular polarization plane and enables the CFD in both detection channels, the TDC is unable to record events from the second surface and a depth measurement is unobtainable. The sensor is configured to minimize systematic coupling of energy into the perpendicular polarization plane that may prematurely enable the CFD in the perpendicular detection channel. The Stokes vector $\vec{S}_{TX}$ describing the transmitted polarization orientation has been optimized for maximum linearity and DOP. The Mueller matrices of the transmitter and receiver paths, $\mathbf{M_{TX}}$ and $\mathbf{M_{RX}}$ respectively, avoid the use of reflective components and have been evaluated with negligible capacity to rotate or depolarize incident polarized light. As detailed, misalignment of the transmit and receive polarization planes has been calibrated for cross talk.

Although the dual channel approach provides an estimate of first surface linear depolarization, estimating depolarization of sequential surfaces in the shallow water regime is challenging. For laser light incident on a polarization preserving first surface and depolarizing second surface, the CFD in the parallel detection channel will be enabled initially from the first surface statistically. In the shallow regime, the CFD in the parallel channel is unable to recover from the 270 nsec dead time to discriminate returns from the depolarizing second surface. As a result, the estimate from the second surface is biased toward an increased depolarization ratio δ. A relative change in depolarization of the second surface can be evaluated, but a depolarization ratio cannot be measured without

accounting for the parallel-polarized signal scattered by the second surface but not detected due to the statistics of first surface detection.

The single telescope and detector approach to laser ranging presented in Chapter 5 for the INPHAMIS technique offered a compact and inexpensive sensor layout, with associated concerns regarding operational robustness. The prototype lidar presented in this chapter utilizes the dual detection channel approach to mitigate several of the limitations imposed by a single detection channel. The prototype sensor has no moving parts, permitting comprehensive calibration of the sensor prior to flight operations with minimal potential for future misalignment due to the rotating optics associated with the single channel sensor. The dual detector measurement facilitates simultaneous integration of timing histograms in the parallel and perpendicular detection channels, enabling derivation of the depolarization ratio throughout the flight profile. The biaxial optical layout enables the transmit and receive paths to be fully isolated to prevent scattering internal to the sensor from prematurely reaching the photodetector and enabling the detection electronics.

Chapter 7

Conclusions and Recommendations

7.1 Conclusions

This dissertation has detailed the development of a novel polarization lidar approach to range-resolved observations through distant shallow media. The research has provided the first depth measurement of distant extremely shallow media using a laser ranging sensor. Evolution of the measurement has been presented, from concept to laboratory demonstration to development of prototype instrumentation, which has led to publication [99, 97] and patent [98]. The research is performed in the context of lidar bathymetry and has had tangible impact on the community. In their 2012 book Fluvial Remote Sensing for Science and Management, Carbonneau and Piégay [23] explicitly state that *"in the future, hardware and software developments will enhance the resolution, accuracy, and types of data products derived from riverine airborne lidar surveys. First, the use of polarized lidar will probably enhance the capacities of extremely shallow water bathymetry (Mitchell et al., 2010)."*

Chapters 3 and 4 have demonstrated that a comprehensive approach to range resolved observations through shallow media is provided by a Stokes vector and Mueller matrix description of polarization lidar, comprehensively described by the Stokes Vector Lidar Equation. The conventional scalar approach to lidar quantifies how much the polarization has changed, without identifying the responsible components along the optical path. As a result, the systematic effects of retardance, diattenuation, and depolarization and their contribution to the polarization measurement remain unquantified.

Chapter 5 described the Intrapulse Phase Modification Induced by Scattering technique, which has been developed and patented within the dissertation research. INPHAMIS analyzes naturally-occurring modifications to the polarization orientation transmitted by the sensor, induced by the scattering process. For range resolved observations through shallow media, the INPHAMIS technique has the capacity to transform the dual surface depth measurement into two distinct single surface range-resolved observations, provided the scattering phase matrices of each surface are unique. As a result, conventional limitations on range-resolved observations of shallow media, introduced by the governing time responsivity of the sensor, are effectively removed. Performance of the INPHAMIS technique is optimized within the context of the Stokes Vector Lidar Equation by accounting for and mitigating systematic effects of retardance, diattenuation, and depolarization along the optical path. Operation of the technique was demonstrated for a simulated supraglacial melt lake, demonstrating 1 cm water depth measurement with ± 3 mm uncertainty.

Chapter 6 detailed the design and operation of a prototype polarization lidar developed within the dissertation research to demonstrate applicability of the theory developed in Chapters 3-5 to range resolved observations through shallow media beyond the laboratory environment. The low SNR detection approach was introduced in Chapter 4 as a means to optimize the collection efficiency of range measurements and integrated with the polarization lidar theory to develop a sensor suitable for operations onboard remote platforms where mass, volume, and power restrictions often constrain sensor architecture. The sensor presented in Chapter 6 is particularly attractive for operations over remote locations such as the GIS, where manned field campaigns can be logistically expensive and often pose dangers to those involved due to harsh terrain. Platforms such as UAS offer potential for high-coverage, long-term monitoring of supraglacial melt lakes at low cost.

7.2 Recommendations

The approach to range-resolved observations developed in the dissertation research is fully general and applicable to depth measurement of shallow media bounded by surfaces defined by a unique scattering phase matrix. While the dissertation details research performed in the context

of lidar bathymetry, additional areas of remote depth sensing can benefit from the research. For example, in the biomedical field, polarimetric imaging has been used to identify areas of tissue abnormalities in patients [8], in many cases preventing the patient from undergoing a painful and potentially harmful biopsy to facilitate a proper diagnosis. The images provide an indication of the tissue's capacity to depolarize the incident light, which can serve as an indicator of potentially cancerous cells [106]. Unlike the surface imagery used in the field today, the polarization measurement approach developed in the dissertation may enable evaluation of the surface scattering properties of the tissue as well as an estimate of the depth of abnormal cells, permitting a noncontact measurement of the volume occupied by cancerous cells and providing additional insight into the patient's condition. In addition to depolarizing media such as tissues, bodies of water, etc., diattenuating and retarding surfaces could be considered in future exploration of shallow media.

The dissertation research can be applied to range-resolved observations through shallow media in solid, liquid, or gaseous form where the scattering phase matrices defining the bounding surfaces differ and the received scattered signals can be analyzed and isolated by the Mueller matrix describing the lidar receiver configuration. Furthermore, the approach to remote shallow media depth measurement developed within the research can be applied to additional range-resolved observations in which the first surface is penetrable, the bounding surfaces are detectable, and the range information acquired from each surface is unique. Application of the approach through analysis of polarization information has been presented in this dissertation. Future generations of researchers will evaluate applicability of the approach through utilization of alternative range information; for example, utilization of unique spectral signatures received from each surface.

Bibliography

[1] W. Abdalati and K. Steffen. Greenland ice sheet melt extent: 1979-1999. Journal of Geophysical Research, 106:33983–33988, 2001.

[2] J. Abshire, X. Sun, H. Riris, J. Sirota, J. McGarry, S. Palm, D. Yi, and P. Liiva. Geoscience laser altimeter system (glas) on the icesat mission: On-orbit measurement performance. Geophysical Research Letters, 32:12345–123456, 2005.

[3] T. Allouis, J. Bailly, Y. Pastol, and C. Roux. Comparison of lidar waveform processing methods for very shallow water bathymetry using raman, near-infrared and green signals. Earth Surface Processes and Landforms, 2010.

[4] Tristan Allouis, Jean-Stéphane Bailly, and Denis Feurer. Assessing water surface effects on lidar bathymetry measurements in very shallow rivers: A theoretical study. In Second ESA Space for Hydrology Workshop, Geneva, CHE, pages 12–14, 2007.

[5] J. Alvarez, M. Vaughan, C. Hostetler, W. Hunt, and D. Winker. Calibration technique for polarization-sensitive lidars. Journal of Atmospheric and Oceanic Technology, 23:683–699, 2006.

[6] Markus-Christian Amann, Thierry Bosch, Marc Lescure, Risto Myllyla, and Marc Rioux. Laser ranging: a critical review of usual techniques for distance measurement. Optical Engineering, 40(1):10–19, 2001.

[7] G. Ammon and S. Russell. A laser tracking and ranging system. Applied Optics, 9(10):2256–2260, 1970.

[8] R. Anderson. Polarized light examination and photography of the skin. Arch Dematol, 127:1000–1005, 1991.

[9] C. Bachmann, M. Montes, R. Fusina, C. Parrish, J. Sellars, A. Weidemann, W. Goode, C. Nichols, P. Woodward, K. McIlhany, V. Hill, R. Zimmerman, D. Korwan, B. Truitt, and A. Schwarzchild. Very shallow water bathymetry retrieval from hyperspectral imagery at the virginia coast reserve (vcr'07) multi-sensor campaign. 2008.

[10] C. Bachmann, M. Montes, R. Fusina, C. Parrish, J. Sellars, A. Weidemann, W. Goode, C. Nichols, P. Woodward, K. McIlhany, V. Hill, R. Zimmerman, D. Korwan, B. Truitt, and A. Schwarzchild. Bathymetry retrieval from hyperspectral imagery in the very shallow water limit: a case study from the 2007 virginia coast reserve (vcr'07) multi-sensor campaign. Marine Geodesy, 33:53–75, 2010.

[11] E Bahar and X Shi. The scattering and depolarization of electromagnetic waves by random rough surfaces with different scales of roughness: new full wave solutions. International Journal of Remote Sensing, 19(11):2171–2185, 1998.

[12] Y. Balin, B. Kaul, G. Kokhanenko, and D. Winker. Applications of circularly polarized laser radiation for sensing of crystal clouds. Optics Express, 17:6849–6859, 2009.

[13] L. Bartolini, L. Dominicis, M. Collibus, G. Fornetti, M. Francucci, M. Guarneri, E. Paglia, C. Poggi, and R. Ricci. Polarimetry as tool to improve phase measurement in an amplitude modulated laser for submarine archaeological sites inspection. Proceedings of SPIE, 6618, 2007.

[14] N. Battaglia. Utility of satellite lidar waveform data in shallow water. Technical report, DTIC Document, 2010.

[15] G. Baumgarten, K. Fricke, and G. Cossart. Investigation of the shape of noctilucent cloud particles by polarization lidar technique. Geophysical Research Letters, 29:12345–123456, 2002.

[16] G. Berkovic and E. Shafir. Optical methods for distance and displacement measurements. Advances in Optics and Photonics, 4(4):441–471, 2012.

[17] B. Blair, D. Rabine, and M. Hofton. The laser vegetation imaging sensor: a medium-altitude, digitisation-only, airborne laser altimeter for mapping vegetation and topography. ISPRS Journal of Photogrammetry and Remote Sensing, 54:115–122, 1999.

[18] Max Born and Emil Wolf. Principals of optics. Oxford: Pergamon, 1980.

[19] G. Boulton and K. Dobbie. Slow flow of granular aggregates: the deformation of sediments beneath glaciers. Phil. Trans. R. Soc. Lond. A, 356:2713–2745, 1998.

[20] J. Box, D. Bromwich, B. Veenhuis, L. Bai, J. Stroeve, J. Rogers, K. Steffen, T. Haran, and S. Wang. Greenland ice sheet surface mass balance variability (19882004) from calibrated polar mm5 output. Journal of Climate, 19:2783–2800, 2006.

[21] J. Box and K. Ski. Remote sounding of greenland supraglacial melt lakes: implications for subglacial hydraulics. Journal of Glaciology, 53, 2007.

[22] J. Bufton, F. Hoge, and R. Swift. Airborne measurements of laser backscatter from the ocean surface. Applied Optics, 22:2603–2618, 1983.

[23] P. Carbonneau and H. Piégay. Fluvial remote sensing for science and management, 2012.

[24] A. Carswell and S. Pal. Polarization anisotropy in lidar multiple scattering from clouds. Applied Optics, 19:4123–4126, 1980.

[25] M. Chaplin, 2013. [Online; accessed 16-March-2013].

[26] F. Chen, Y. Kun-tao, and K. Ming-wu. Polarization detection technology of underwater targets for airborne lidar. Proc. of SPIE, 6150, 2006.

[27] R. Chipman and S. Lu. Decomposition of mueller matrices. Proc. of SPIE, 3120, 1997.

[28] Russell A Chipman. Polarimetry. Handbook of optics, 2:0–1, 1995.

[29] J. Churnside. Polarization effects on oceanographic lidar. Opt. Express, 16:1196–1207, 2008.

[30] J. Churnside and P. McGillivary. Optical properties of several pacific fishes. Applied Optics, 36:6011–6020, 1997.

[31] J. Churnside, J. Wilson, and V. Tatarskii. Lidar profiles of fish schools. Applied Optics, 30:2925–2927, 1991.

[32] J. Churnside, J. Wilson, and V. Tatarskii. Airborne lidar for fisheries applications. Opt. Eng., 40:406–414, 2001.

[33] T. Cossio, K. Slatton, W. Carter, K. Shrestha, and D. Harding. Predicting topographic and bathymetric measurement performance for low-snr airborne lidar. IEEE Transactions on Geoscience and Remote Sensing, 47, 2009.

[34] Tristan Cossio. Prediction of topographic and bathymetric measurement performance of airborne low-SNR lidar systems. PhD thesis, University of Florida, 2009.

[35] S. Das, I. Joughin, M. Behn, I. Howat, M. King, D. Lizarralde, and M. Bhatia. Fracture propagation to the base of the greenland ice sheet during supraglacial lake drainage. Science, 320, 2008.

[36] B. DeBoo, J. Sasian, and R. Chipman. Degree of polarization surfaces and maps for analysis of depolarization. Optics Express, 12:4941–4958, 2004.

[37] B. DeBoo, J. Sasian, and R. Chipman. Depolarization of diffusely reflecting man-made objects. Applied Optics, 44:5434–5445, 2005.

[38] J. Degnan. Unified approach to photon-counting microlaser rangers, transponders, and altimeters. Surveys in Geophysics, 22:431–447, 2001.

[39] J. Degnan. Photon-counting multikilohertz microlaser altimeters for airborne and spaceborne topographic measurements. Journal of Geodynamics, 34:503–549, 2002.

[40] J. Degnan, J. McGarry, T. Zagwodzki, P. Dabney, J. Geiger, R. Chabot, C. Steggerda, J. Marzouk, and A. Chu. Design and performance of a 3-d imaging, photon-counting, microlaser altimeter operating from aircraft cruise altitudes under day or night conditions. Proceedings of SPIE, 4546, 2002.

[41] Massimo Del Guasta, Edgar Vallar, Olivier Riviere, Francesco Castagnoli, Valerio Venturi, and Marco Morandi. Use of polarimetric lidar for the study of oriented ice plates in clouds. Applied optics, 45(20):4878–4887, 2006.

[42] J. Dowdeswell. The greenland ice sheet and global sea-level rise. Science, 311:963–964, 2006.

[43] Marino Eccher. How much oil has spilled in the gulf? @ONLINE.

[44] V.I. Feigels and Y.I. Kopilevich. Russian airborne lidar for oceanography. In Society of Photo-Optical Instrumentation Engineers (SPIE) Conference Series, volume 2111, pages 127–141, 1993.

[45] V. Feygels, C. Wright, Y. Kopilevich, and A. Surkov. Narrow field-of-view bathymetric lidar: theory and field test. Proceedings of SPIE, 5155, 2003.

[46] P.H. Flamant. Atmospheric and meteorological lidar: from pioneers to space applications. Comptes Rendus Physique, 6(8):864–875, 2005.

[47] C. Flynn, A. Mendoza, Y. Zheng, and S. Mathur. Novel polarization-sensitive micropulse lidar measurement technique. Optics Express, 15:2785–2790, 2007.

[48] R. Gauldie, S. Sharma, and C. Helsley. Lidar applications to fisheries monitoring problems. Can. J. Fish. Aquat. Sci., 53:1459–1468, 1996.

[49] S. Georgiou, A. Shepherd, M. McMillan, and P. Nienow. Seasonal evolution of supraglacial lake volume from aster imagery. Annals of Glaciology, 50:95–100, 2009.

[50] G. Gilbert and J. Pernicka. Improvement of underwater visibility by reduction of backscatter with a circular polarization technique. Applied Optics, 6:741–756, 1967.

[51] G. Gimmestad. Reexamination of depolarization in lidar measurements. Applied Optics, 47:3795–3802, 2008.

[52] D. Goldstein. Polarized Light, 2nd Ed. CRC Press, 2003.

[53] G. Guenther. Airborne laser hydrography: system design and performance factors. NOAA Professional Paper Series, National Ocean Service 1, 1985.

[54] G. Guenther, M. Brooks, and P. LaRocque. New capabilities of the shoals airborne lidar bathymeter. Remote Sensing of Environment, 73:247–255, 2000.

[55] G. Guenther, A. Cunningham, P. LaRocque, and D. Reid. Meeting the accuracy challenge in airborne lidar bathymetry. In Proceedings of 20th EARSeL Symposium: Workshop on Lidar Remote Sensing of Land and Sea, 2000.

[56] G. Guenther, P. LaRocque, and W. Lillycrop. Multiple surface channels in shoals airborne lidar. Proceedings of SPIE, 2258, 1994.

[57] G. Guenther and R. Thomas. System design and performance factors for airborne laser hydrography. In Proceedings Oceans '83, pages 425–430, 1983.

[58] G.C. Guenther and L.R. Goodman. Laser applications for near-shore nautical charting. In 22nd Annual Technical Symposium, pages 174–183. International Society for Optics and Photonics, 1978.

[59] G.C. Guenther and DF Maune. Airborne lidar bathymetry. Digital elevation model technologies and applications: the DEM users manual, 2:253–320, 2007.

[60] X. Guo, M. Wood, N. Ghosh, and I. Vitkin. Depolarization of light in turbid media: a scattering event resolved monte carlo study. Applied Optics, 49, 2010.

[61] B. Gutelius. Airborne lidar bathymetry: sea, shore and more. Lidar Magazine, 2, 2012.

[62] D. Hall, S. Nghiem, C. Schaaf, N. DiGirolamo, and G. Neumann. Evaluation of surface and near-surface melt characteristics on the greenland ice sheet using modis and quikscat data. Journal of Geophysical Research, 114, 2009.

[63] D. Harding. Pulsed laser altimeter ranging techniques and implications for terrain mapping. Topographic Laser Ranging and Scanning Principles and Processing, pages 173–194, 2009.

[64] M. Hayman. Optical theory for advancement of polarization lidar. PhD thesis, University of Colorado Boulder, 2011.

[65] M. Hayman and J. Thayer. Accounting for system affects in depolarization lidar. In Conference on Lasers and Electro-Optics/International Quantum Electronics Conference, 2009.

[66] M. Hayman and J. Thayer. Explicit description of polarization coupling in lidar applications. Optics Letters, 34(5):611–613, 2009.

[67] M. Hayman and J. Thayer. Lidar polarization measurements of pmcs. Journal of Atmospheric and Solar-Terrestrial Physics, In Press, Corrected Proof:–, 2010.

[68] M. Hayman and J. P. Thayer. General description of polarization in lidar using stokes vectors and polar decomposition of mueller matrices. J. Opt. Soc. Am. A, 29:400–409, 2012.

[69] G. Hickman and J. Hogg. Application of an airborne pulsed laser for near shore bathymetric measurements. Remote Sensing of Environment, 1:47–58, 1969.

[70] W. Hunt, D. Winker, M. Vaughan, and K. Powell. Calipso lidar description and performance assessment. Journal of Atmospheric and Oceanic Technology, 26:1214–1228, 2009.

[71] J. Irish and W. Lillycrop. Scanning laser mapping of the coastal zone: the shoals system. ISPRS Journal of Photogrammetry and Remote Sensing, 54:123–129, 1999.

[72] J. Irish and T. White. Coastal engineering applications of high-resolution lidar bathymetry. Coastal Engineering, 35:47–71, 1998.

[73] RA Jarvis. A perspective on range finding techniques for computer vision. Pattern Analysis and Machine Intelligence, IEEE Transactions on, (2):122–139, 1983.

[74] I. Joughin, S. Das, M. King, B. Smith, I. Howat, and T. Moon. Seasonal speedup along the western flank of the greenland ice sheet. Science, 320:781–783, 2008.

[75] C.O. Justice, E. Vermote, J.R.G. Townshend, R. DeFries, D.P. Roy, D.K. Hall, V.V. Salomonson, J.L. Privette, G. Riggs, A. Strahler, W. Lucht, R.B. Myneni, Y. Knyazikhin, S.W. Running, R.R. Nemani, Zhengming Wan, A.R. Huete, W. Van Leeuwen, R.E. Wolfe, L. Giglio, J. Muller, P. Lewis, and M.J. Barnsley. The moderate resolution imaging spectroradiometer (modis): land remote sensing for global change research. Geoscience and Remote Sensing, IEEE Transactions on, 36(4):1228 –1249, jul 1998.

[76] Ilkka P. Kaisto, Juha T. Kostamovaara, Ilkka Moring, and Risto A. Myllylae. Laser range-finding techniques in the sensing of 3-d objects. pages 122–133, 1990.

[77] Bruno V Kaul. Lidar equation for sensing optically anisotropic media. In Remote Sensing, pages 332–339. International Society for Optics and Photonics, 1998.

[78] W. Kaula, G. Schubert, R. Lingenfelte, W. Sjogren, and W. Wollenhaupt. Apollo laser altimetry and inferences as to lunar structure. In Proceedings of the 5th Lunar Conference, volume 3.

[79] A. Kilpela. Pulsed time-of-flight laser range finder techniques for fast, high precision measurement applications, 2004.

[80] H. Kim, P. Cervenka, and C. Lankford. Development of an airborne laser bathymeter. NASA Technical Note, D-8079, 1975.

[81] P. Kinzel, C. Wright, J. Nelson, and A. Burman. Evaluation of an experimental lidar for surveying a shallow, braided, sand-bedded river. Journal of Hydraulic Engineering, 133, 2007.

[82] M. Krawczynski, M. Behn, S. Das, and I. Joughin. Constraints on the lake volume required for hydro-fracture through ice sheets. Geophysical Research Letters, 36, 2009.

[83] P.E. LaRocque and G.R. West. Airborne laser hydrography: an introduction. In Proc. ROPME/PERSGA/IHB Workshop on Hydrographic Activities in the ROPME Sea area and Red Sea, volume 4, pages 1–15, 1999.

[84] D Levitan. Laser eyes spy a big melt in the arctic. Spectrum, IEEE, 50(2):9–10, 2013.

[85] W.J. Lillycrop, J.M. Wozencraft, R.W. Pope, et al. Airborne lidar hydrography: a vision for tomorrow. Sea Technology, 43(6), 2002.

[86] S. Lu and R. Chipman. Interpretation of mueller matrices based on polar decomposition. J. Opt. Soc. Am. A, 13:1106–1113, 1996.

[87] S. Luthcke, H. Zwally, W. Abdalati, D. Rowlands, R. Ray, R. Nerem, F. Lemoine, J. McCarthy, and D. Chinn. Recent greenland ice mass loss by drainage system from satellite gravity observations. Science, 314:1286–1289, 2006.

[88] M. Luthje, D. Feltham, P. Taylor, and M. Worster. Modeling the summertime evolution of sea-ice melt ponds. Journal of Geophysical Research, 111, 2006.

[89] Lori A Magruder, Michael E Wharton III, Kevin D Stout, and Amy L Neuenschwander. Noise filtering techniques for photon-counting ladar data. In Proceedings of SPIE, volume 8379, page 83790Q, 2012.

[90] S. McGee, 2010. [Online; accessed 8-March-2013].

[91] M. McGill, D. Hlavka, W. Hart, S. Scott, J. Spinhirne, and B. Schmid. Cloud physics lidar: instrument description and initial measurement results. Applied Optics, 41:3725–3734, 2002.

[92] M. McMillan, P. Nienow, A. Shepherd, T. Benham, and A. Sole. Seasonal evolution of supraglacial lakes on the greenland ice sheet. Earth and Planetary Science Letters, 262:484–492, 2007.

[93] R. Measures. Laser remote sensing: fundamentals and applications. Krieger Publishing Company, 1984.

[94] E. Miasnikov and T. Kondranin. Effectiveness of the polarization discrimination technique for underwater viewing systems. Ocean Optics XI, 1750:433–442, 1992.

[95] D. Miller. A really inconvenient truth: Dan miller, 2009. [Online; accessed 21-February-2013].

[96] S. Mitchell and J. P. Thayer. Enhanced characterization of semitransparent media through application of polarization lidar. In 26th International Laser Radar Conference, 2012.

[97] S. Mitchell and J. P. Thayer. (In Review) Ranging through shallow semitransparent media with polarization lidar. Journal of Atmospheric and Oceanic Technologies, 2013.

[98] S. Mitchell, J. P. Thayer, M. Hayman, et al. Remote measurement of shallow depths in semi-transparent media, January 4 2013. WO Patent 2,013,003,771.

[99] S. Mitchell, J.P. Thayer, and M. Hayman. Polarization lidar for shallow water depth measurement. Applied optics, 49(36):6995–7000, 2010.

[100] M. Moussavi, W. Abdalati, and T. Scambos. A simulator to assess the bathymetric capabilities of a space-borne lidar over shallow supraglacial lakes. American Geophysical Union Fall Meeting, 2012.

[101] A. Nayegandhi, J. Brock, and C. Wright. Classifying vegetation using nasas experimental advanced airborne research lidar (eaarl) at assateague island national seashore. In Proceedings ASPRS Annual Conference, 2005.

[102] A. Nayegandhi, J. Brock, and C. Wright. Small-footprint, waveform-resolving lidar estimation of submerged and sub-canopy topography in coastal environments. International Journal of Remote Sensing, 30(4):861–878, 2009.

[103] A. Nayegandhi and R. Faux. Performance considerations for small-footprint topobathymetric lidar. Presented at the International Lidar Mapping Forum, Denver, CO, 2013.

[104] A. Nayegandhi, C. Wright, and J. Brock. Chapter 1 - EAARL: an airborne lidar system for mapping coastal and riverine environments. UNKNOWNl, 2009.

[105] R. Neely, M. Hayman, J. P. Thayer, R. Hardesty, M. O'Neill, R. Stillwell, and C. Alvarez. The cloud, aerosol backscatter and polarization lidar at summit, greenland. In Proceedings of 26th International Laser Radar Conference, 2012.

[106] Tatiana Novikova, Angelo Pierangelo, Antonello De Martino, Abdelali Benali, and Pierre Validire. Polarimetric imaging for cancer diagnosis and staging. Optics and Photonics News, 23(10):26–33, 2012.

[107] BM Oliver. Thermal and quantum noise. Proceedings of the IEEE, 53(5):436–454, 1965.

[108] Gregory R Osche. Optical Detection Theory. Wiley New York, 2002.

[109] LM Ott. Underwater ranging measurements using blue-green laser. NAVAIRDEVCEN Report, 1965.

[110] S. Peeri, L. Morgan, W. Philpot, and A. Armstrong. Land-water interface resolved from airborne lidar bathymetry (alb) waveforms. Journal of Coastal Research, 62:75–85, 2011.

[111] S. Peeri and W. Philpot. Increasing the existence of very shallow-water lidar measurements using the red-channel waveforms. IEEE Transactions on Geoscience and Remote Sensing, 45:1217–1223, 2007.

[112] M. Penny, R. Abbot, D. Phillips, B. Billard, D. Rees, D. Faulkner, D. Cartwright, B. Woodcock, G. Perry, P. Wilsen, T. Adams, and J. Richards. Airborne laser hydrography in australia. Applied Optics, 25:2046–2058, 1986.

[113] G. Petty. A first course in atmospheric radiation. Sundog Publishing, 2006.

[114] Nathan D Quadros and Philip A Collier. Delineating the littoral zone using topographic and bathymetric lidar. In ABLOS Conference, pages 16–17, 2008.

[115] ND Quadros, PA Collier, and CS Fraser. Integration of bathymetric and topographic lidar: a preliminary investigation. Remote Sensing and Spatial Information Sciences, 37:1299–1304, 2008.

[116] Yakov I Rabinovich, Joshua J Adler, Madhavan S Esayanur, Ali Ata, Rajiv K Singh, and Brij M Moudgil. Capillary forces between surfaces with nanoscale roughness. Advances in colloid and interface science, 96(1):213–230, 2002.

[117] E. Rignot and P. Kanagaratnam. Changes in the velocity structure of the greenland ice sheet. Science, 311, 2006.

[118] S. Rodier, Y. Hu, and M. Vaughan. Calipso surface return for ice and water detection. In Proceedings of 26th International Laser Radar Conference, 2012.

[119] JM Sanz, JM Saiz, F González, and F Moreno. Polar decomposition of the mueller matrix: a polarimetric rule of thumb for square-profile surface structure recognition. Applied Optics, 50(21):3781–3788, 2011.

[120] Kenneth Sassen, Jiang Zhu, Peter Webley, Ken Dean, and Patrick Cobb. Volcanic ash plume identification using polarization lidar: Augustine eruption, alaska. Geophysical research letters, 34(8):L08803, 2007.

[121] C. Schoof. Ice-sheet acceleration driven by melt supply variability. Nature, 468:803–806, 2010.

[122] K. Shrestha, W. Carter, K. Slatton, and T. Cossio. Shallow bathymetric mapping via multistop single photoelectron sensitivity laser ranging. IEEE Geoscience and Remote Sensing Letters, 50, 2012.

[123] R. Simon. Nondepolarizing systems and degree of polarization. Optics Communications, 77, 1990.

[124] K. Slatton, W. Carter, R. Shrestha, and W. Dietrich. Airborne laser swath mapping: achieving the resolution and accuracy required for geosurficial research. Geophysical Research Letters, 34, 2007.

[125] C. Smith and K. Baker. Optical properties of the clearest natural waters (200-800 nm). Applied Optics, 20:177–184, 1981.

[126] L.D. Smullin and G. Fiocco. Optical echoes from the moon. 1962.

[127] W. Sneed and G. Hamilton. Evolution of melt pond volume on the surface of the greenland ice sheet. Geophysical Research Letters, 34, 2007.

[128] W. Sneed and G. Hamilton. Validation of a method for determining the depth of glacial melt ponds using satellite imagery. Annals of Glaciology, 52:15–22, 2011.

[129] GP Sorenson, RC Honey, and JR Payne. Analysis of the use of airborne laser radar for submarine detection and ranging. SRI, Report, 5583, 1966.

[130] A. Sundal, A. Shepherd, P. Nienow, E. Hanna, S. Palmer, and P. Huybrechts. Evolution of supra-glacial lakes across the greenland ice sheet. Remote Sensing of Environment, 113:2164–2171, 2009.

[131] M. Tedesco and N. Steiner. In-situ multispectral and bathymetric measurements over a supraglacial lake in western greenland using a remotely controlled watercraft. The Cryosphere, 5:445–452, 2011.

[132] R. Thomas, E. Frederick, W. Krabill, S. Manizade, and C. Martin. Progressive increase in ice loss from greenland. Geophysical Research Letters, 33, 2006.

[133] V. Tsai and J. Rice. A model for turbulent hydraulic fracture and application to crack propagation at glacier beds. Journal of Geophysical Research, 115, 2010.

[134] Gaspar R Valenzuela. Theories for the interaction of electromagnetic and oceanic wavesa review. Boundary-Layer Meteorology, 13(1):61–85, 1978.

[135] A. Vasilkov, Y. Goldin, B. Gureev, F. Hoge, R. Swift, and C. Wright. Airborne polarized lidar detection of scattering layers in the ocean. Applied Optics, 40:4353–4364, 2001.

[136] L.M. Wedding, A.M. Friedlander, M. McGranaghan, R.S. Yost, and M.E. Monaco. Using bathymetric lidar to define nearshore benthic habitat complexity: Implications for management of reef fish assemblages in hawaii. Remote Sensing of Environment, 112(11):4159–4165, 2008.

[137] C. Weitkamp. Lidar: range-resolved optical remote sensing of the atmosphere, volume 102. Springer, 2005.

[138] S. White. Utilization of lidar and noaa's vertical datum transformation tool (vdatum) for shoreline delineation. In OCEANS 2007, pages 1–6. IEEE, 2007.

[139] Wikipedia. Stokes parameters, 2004. [Online; accessed 9-February-2013].

[140] Wikipedia. Electromagnetic absorption by water, 2013. [Online; accessed 8-March-2013].

[141] A. Witze. Melting at the microscale. ScienceNews, 177, 2010.

[142] J. Wozencraft and J. Lillycrop. Shoals airborne coastal mapping: past, present, and future. Journal of Coastal Research, 38:207–215, 2003.

[143] J.M. Wozencraft and W.J. Lillycrop. Total shallow-water survey through airborne hydrography. Technical report, DTIC Document, 2002.

[144] Y. Yamaguchi, A.B. Kahle, H. Tsu, T. Kawakami, and M. Pniel. Overview of advanced spaceborne thermal emission and reflection radiometer (aster). Geoscience and Remote Sensing, IEEE Transactions on, 36(4):1062 –1071, jul 1998.

[145] H. Zwally, W. Abdalati, T. Herring, K. Larson, J. Saba, and K. Steffen. Surface melt-induced acceleration of greenland ice-sheet flow. Science, 297:218–222, 2002.